Optical Measurement Methods and an Optically Induced Phenomenon in Piezoelectric Transducers

Michio Ohki

Contents

Chapter 1
Introduction

Interaction processes between electrical, mechanical and thermal systems can be described crystallographically.[1] Piezoelectricity is a linear interaction between electrical and mechanical systems. Stress T applied to a piezoelectric crystal causes not only strain S but also polarization P. The former is based on Hooke's law, and the latter is the direct piezoelectric effect. This is a transformation of mechanical to electrical energy. Conversely, electric field E applied to the crystal causes not only polarization P but also strain S. These two transformations between different states of energy are equivalent in a thermodynamic aspect using Gibbs free energy, and represented by applying the same piezoelectric constant d as follows,

$$P\,(= D - \varepsilon_0 E) = dT + \chi^T E, \tag{1.1}$$

$$S = s^E T + dE, \tag{1.2}$$

where D is electric flux density, ε_0 is permittivity in vacuum, χ^T is electric susceptibility when $T = 0$, and s^E is elastic compliance when $E = 0$. The variables of state in eqs. (1.1) and (1.2), P, S, T and E, are assumed to be d.c.; therefore, the material constants d, χ^T and s^E are defined at the low frequency limit. If metal electrodes are deposited on both surfaces where polarized charges appear and the circuit is shorted between the electrodes ($E = 0$), stress T applied to the crystal causes electric flux density D which corresponds to true electric charge density. If either the electric circuit is opened or metal electrodes are not deposited ($D = 0$), stress T applied to the crystal causes depolarizing field $E = -P/\varepsilon_0$ in the crystal. The difference of the electric condition when either $E = 0$ or $D = 0$ is important. If electric field E applied to the crystal is alternating, that is, periodic in time domain, generated strain S is also alternating; therefore, piezoelectric vibration occurs. The resonance can occur at various frequencies determined by the shape and the material constants of the piezoelectric transducer. From a crystallographic point of view, the piezoelectricity exists in the materials whose crystal structures do not have centrosymmetry. Representative piezoelectric materials are as follows: quartz (SiO_2), barium titanate ($BaTiO_3$) ceramics, PZT ($PbZr_xTi_{1-x}O_3$) ceramics, lithium niobate ($LiNbO_3$), lithium tantalate ($LiTaO_3$), *etc*. These piezoelectric materials have been widely applied to electronics since W.G.Cady succeeded in steadying oscillation frequency of electronic circuit using piezoelectric vibration of quartz.

Piezoelectric vibration and material can be evaluated using the electromechanical method[2] which measures the admittance of the piezoelectric transducer near its resonance frequencies.

Usually, after metal electrodes are deposited on the piezoelectric sample, the relation between electric current and voltage is measured. With this method, we can evaluate, for example, the electromechanical coupling coefficient and Q-value of the sample. However, this method provides the data only on the characteristics of the sample as a whole, and no method has been available, which can measure the piezoelectric properties at some specific points in the sample. One purpose of this thesis, therefore, exists to develop the new method by which local piezoelectric vibrations can be measured, taking advantage of coherence of optical waves. Optical probing techniques using laser and optical fiber are chosen for this purpose. Here acoustic vibration can be detected by interference of two coherent optical waves which are phase-modulated by interaction with the acoustic vibration. The physical quantities evaluated directly by these optical methods are the amplitude and the phase of the acoustic vibration in the piezoelectric transducer. Several types of interferometers have been proposed for optical measurements. Here we adopt the fiber optic ring interferometer.[3),4)] This interferometer has the merit of compensating temperature variation. But, optical methods can not measure all physical values necessary for the evaluation of materials. Previous optical measurement of acoustic vibration did not pay attention to the evaluation of materials. For this purpose, we do not deny the virtue of the electromechanical method in this thesis. New measurement methods can be created by considering the electric condition of the piezoelectric vibration when either $E = 0$ or $D = 0$, as mentioned above, and the theory of vibration, which the electromechanical method is based on. The value corresponding to the piezoelectric constant and Poisson's ratio which are regarded as the material constants can be obtained simply. Concerning the piezoelectric transducer, not only the material constants but also the shape of the transducer is an important factor determining the characteristics. For example, in the case of the transducers whose forms are columnar, different vibrational characteristics can be obtained for different ratios of the radius to the height of the column. The influence of the difference of the form on the results of the present measurement is also investigated experimentally and theoretically. In this study, PZT piezoelectric ceramics are used as samples for the measurement, because samples in various shapes can be easily prepared.

From a crystallographic point of view, the crystal with the piezoelectric effect is possible to exhibit the Pockels effect—— an electrooptic effect of the first order, in which the refractive index of the crystal is changed by electric field. Transparent or semitransparent piezoelectric crystals in which optical waves can propagate, for example, $LiNbO_3$, $LiTaO_3$, PLZT ceramics, potassium dihydrogenphosphate (KH_2PO_4), *etc.*, are used for such electrooptic applications. Another objective of this thesis is to discover and examine a new phenomenon induced by coherent optical waves in a semitransparent piezoelectric transducer. We pay attention to the photorefractive (PR) effect for this purpose. The PR effect is the phenomenon in which the refractive index of an electrooptic crystal, that is, a piezoelectric crystal, varies according to the incidence

of visible rays.[5] Interference of two coherent optical waves yields fringes which cause excitation and diffusion of carriers, forming a space-charge distribution in the crystal.[6] The variation of the refractive index is caused by the internal electric field from the charge distribution through the Pockels effect. Representative photorefractive materials are $LiNbO_3$, $BaTiO_3$ single crystal, $Bi_{12}SiO_{20}$, *etc*. Application of this effect to holography and optical processing has been developed in recent years.[7] Application to acoustics has also been developed; an acoustic wave is filtered by the periodic variation of the acoustic velocity that is caused by the internal electric field.[8] In this thesis, the influence of the PR effect on piezoelectric vibration is investigated from a new point of view. We view electromechanical characteristics of Fe-doped $LiNbO_3$ ($LiNbO_3$:Fe) piezoelectric transducers with the PR grating near the resonance frequencies of the modes of vibration. We adopt $LiNbO_3$:Fe because of its excellent piezoelectricity and its longevity of stored PR grating. Strong nonlinear acoustic vibration was observed in the piezoelectric resonator with the PR grating. The reason for the generation of the present nonlinear phenomenon is also considered.

This study recommends the development of an interdisciplinary field among piezoelectric material science, acoustics and optics, on the basis of the electromechanical measurement method of piezoelectric transducer and the nature of interference of coherent optical waves.

The composition of this thesis is as follows. In Chapter 2, the measurement methods of piezoelectric vibration using optical fiber are described from an optical point of view.[9]-[11] In Chapter 3, the evaluation of the piezoelectric vibration and material is described. A disk piezoelectric transducer is used as the sample. First, the value corresponding to the piezoelectric constant is measured locally by a new method.[10]-[12] In this method, the optical measurement of the *amplitude* of the piezoelectric vibration and the electromechanical measurement of the admittance are mixed, considering the electric condition of the piezoelectric vibration and the theory of vibration. Second, the acoustic velocity of the radial-extensional mode and Poisson's ratio of the material are measured by a new method.[13] With this method, the optical measurement of the *phase* of the piezoelectric vibration is used. In Chapter 4, the measurement methods described in Chapter 3 are applied to circular piezoelectric transducers whose forms are not disk, that is, in the case of other ratios of the radius to the height. The experimental results are considered by using the theory of resonance coupling.[14],[15] In Chapter 5, the influence of the PR effect on piezoelectric vibration is investigated experimentally.[16],[17] In addition, the experimental results are explained by a new concept, space-periodic modulation of the piezoelectric polarization due to the PR internal electric field.[18],[19] In Chapter 6, the results obtained from this study are summarized.

References

1) W.P.Mason: *Crystal Physics of Interaction Processes* (Academic Press, New York, 1966)

2) T.Ikeda: *Fundamentals of Piezoelectricity* (Oxford University Press, 1990)

3) R.Ulrich: Optics Lett., **5** (1980), 173.

4) J.E.Bowers, R.L.Jungerman, B.T.Khuri-Yakub, and G.S.Kino: Jour. Lightwave Tech., **LT-1** (1983), 488.

5) A.Ashkin *et al.*: Appl. Phys. Lett., **9** (1966) 72.

6) P.Gunter *et al.* (editor): *Photorefractive Materials and Their Applications I* (Springer-Verlag, Berlin, 1988)

7) A.Yariv: *Optical Electronics 4th ed.* (Holy, Rinchart and Winston Inc., Orland, 1991)

8) D.E.Oates and J.Y.Pan: Ferroelectronics, **92** (1989) 253.

9) M.Ohki, N.Shima and T.Shiosaki: *Proc. 12th Symp. Ultrasonic Electronics, Tokyo, 1991*, Jpn.J.Appl.Phys., **31**(1992) Suppl.31-1, p.105

10) M.Ohki, N.Shima and T.Shiosaki: IEICE Tech.Rep., US90-71,EA90-84 (1991.1.25) [in Japanese]

11) M.Ohki, T.Kita and T.Shiosaki: IEICE Tech.Rep., US91-23 (1991.7.16) [in Japanese]

12) M.Ohki and T.Shiosaki: *Proc. IEEE Ultrasonics Symp.,Florida, 1991* (IEEE, Piscataway, 1991) p.615

13) M.Ohki, N.Shima and T.Shiosaki: Jpn.J.Appl.Phys., **32**(1993) 2463.

14) M.Ohki, N.Shima and T.Shiosaki: Jpn.J.Appl.Phys., **31**(1992) 3272.

15) M.Ohki, N.Shima and T.Shiosaki: IEICE Tech.Rep., US91-79,EA91-92 (1992.1.28) [in Japanese]

16) M.Ohki, N.Taniguchi and T.Shiosaki: Jpn.J.Appl.Phys., **31**(1992) 3249.

17) M.Ohki, N.Taniguchi and T.Shiosaki: *Proc. IEEE ISAF, Greenville, 1992*, p.156

18) M.Ohki and T.Shiosaki: Jpn.J.Appl.Phys., **32**(1993) 2243.

19) M.Ohki and T.Shiosaki: *Proc. IEEE Ultrasonics Symp., Tucson, 1992*

Chapter 2
Measurement of Piezoelectric Vibration Using Optical Fiber

§2.1. Introduction

Optical measurement methods are useful because of their higher sensitivity and capability of measuring physical parameters that cannot be measured by electric methods. In particular, methods using optical fibers have the following advantages: 1) optical alignment is not necessary in constructing an interferometer; 2) a very long optical path can be prepared in the laboratory easily; and 3) optical fibers have not only the function of wave guides, but also sensors, by themselves. In this chapter, two new methods for measurement of piezoelectric vibration using the interaction between the piezoelectric vibration and light waves traveling in optical fibers are described. In one method, the sample is in contact with the fiber, in which the light is phase-modulated by piezoelectric vibration.[1] In this case, the fiber is wrapped many turns around a cylindrical piezoelectric transducer. In the other method, the light is incident on the sample surface and phase-modulated by reflection when the sample vibrates.[2)-5)] This method enables us to evaluate the vibration locally by changing the measurement point where the light is incident. In either method, the modulated optical phase has a relation to the acoustic amplitude and phase of the transducer; therefore, by detecting the phase-modulated signal, we can measure the acoustic vibration and evaluate the vibration and material of the transducer. The ring interferometer was developed for this experiment. Here the measurement of piezoelectric vibration using the ring interferometer is discussed from an optical point of view.

§2.2. Ring Interferometer

Electric field vector E [V/m] of an optical wave can be expressed as

$$E = A\cos(\omega_C t + \phi_C), \tag{2.2.1}$$

where A is the amplitude and involves the direction of polarized light, ω_C [rad/s] is the angular frequency, and ϕ_C [rad] is the phase. Optical measurement is usually performed by observing the modification of some of the factors, A, ω_C and ϕ_C, caused by the object of measurement. We take the measurement of acoustic vibration which causes phase modulation of coherent optical waves. The phase-modulated signal of light cannot be observed directly by photo-detector; therefore, in order to transform the phase-modulated signal into an intensity-modulated signal,

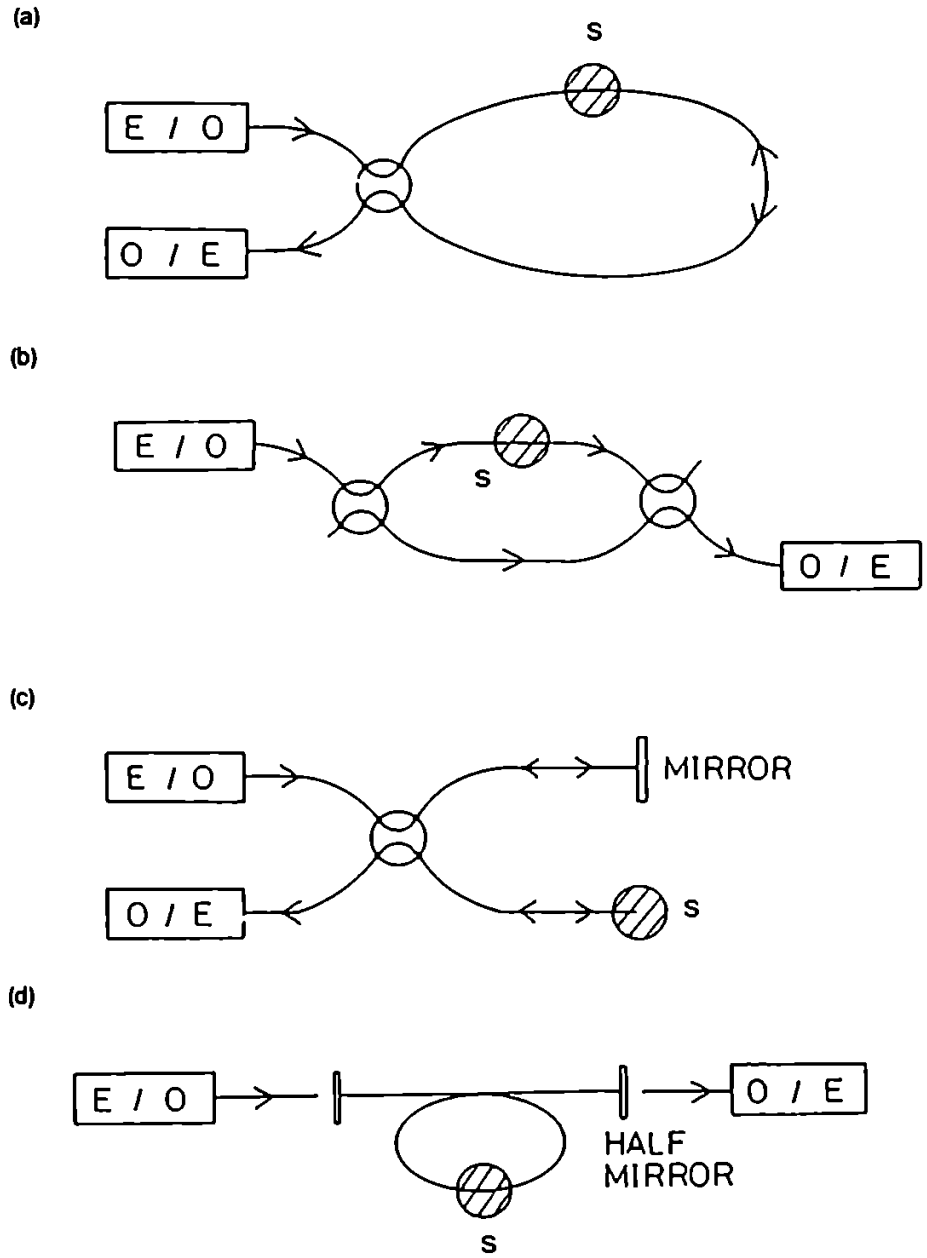

Fig. 2.1. Four kinds of interferometers using optical fibers: (a) Ring, (b) Mach-Zender, (c) Michelson and (d) Fabry-Perot interferometers. The "S" represents the sample for measurement.

an interferometer in which the signal wave and the reference wave interfere with each other is constructed.

The electric fields of the signal wave and the reference one, E_S and E_R, can be represented as

$$E_S = A'_S \cos(\omega_C t + \phi_{CS}), \tag{2.2.2}$$

$$E_R = A'_R \cos(\omega_C t + \phi_{CR}), \tag{2.2.3}$$

where the states of the polarization are assumed to be the same in the two waves. The output of the interferometer, V_{PD} [V], is in proportion to the time average of the square of the sum of the two electric fields; therefore,

$$V_{PD} \propto |A'_S|^2 + |A'_R|^2 + 2\gamma A'_S A'_R \cos(\phi_{CS} - \phi_{CR}), \tag{2.2.4}$$

where γ ($0 \le \gamma \le 1$) is the visibility. When the two waves are incoherent; that is, $\gamma = 0$, the two waves do not interfere, and V_{PD} is in proportion only to the sum of the square of the respective amplitudes. When the two waves are completely coherent; that is, when the difference of the optical paths of the two coherent waves is almost zero, the value of γ becomes unity, and the maximum output on the phase difference $\phi_{CS} - \phi_{CR}$ can be detected. When the difference of the optical paths becomes long, the value of γ decreases, and the output due to the interference decreases. The coherence of the light source has relation to its spectrum width $\Delta\nu$ [Hz]. The coherence time and length, τ_C [s] and l_C [m], are defined expediently by

$$\gamma = \gamma(\tau = 0) \exp(-\tau / \tau_C), \tag{2.2.5}$$

$$\tau_C \cdot \Delta\nu \approx 1, \tag{2.2.6}$$

$$l_C = c \cdot \tau_C, \tag{2.2.7}$$

where the two lights emitted simultaneously from the light source interfere with time difference τ, and c is the velocity of light. The two lights with a smaller difference of the optical path than l_C can be considered to interfere with each other. The light source with narrow spectrum width has high coherence time and length.

Four kinds of interferometers using optical fibers, (a) ring, (b) Mach-Zender, (c) Michelson and (d) Fabry-Perot interferometers are illustrated in Figs. 2.1 (a), 2.1(b), 2.1(c) and 2.1(d), respectively. Single-mode fibers relative to the transverse mode are used for this purpose. Multi-mode fibers cannot be used, because they cannot transfer the information about the optical phase. In this study, the ring interferometer illustrated in Fig. 2.1(a) is selected for the present experiment from among these interferometers. Two waves that travel around the loop clockwise and counterclockwise interfere with each other. Both of the waves can be modified by the object of measurement. This configuration itself is widely used for optical rotation gyro-sensing, [6] measurement of acoustic vibration, [7] and so forth. Since the length of the optical fibers can be

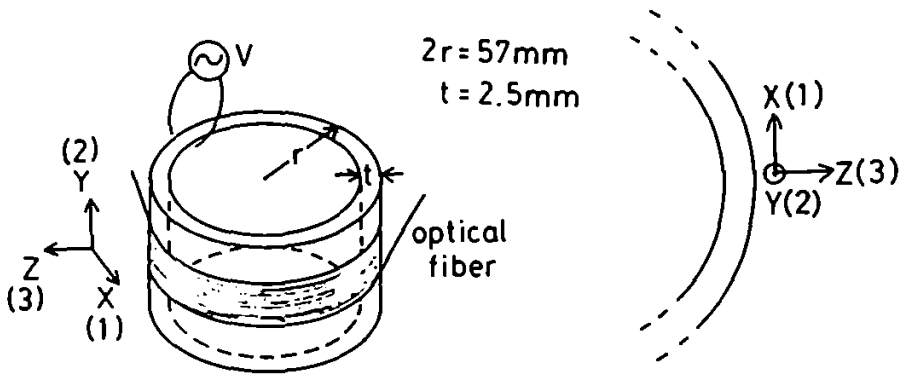

Fig. 2.2. Fiber-optic wrap-around cylindrical phase modulator.

Table 2.I. Main material constants of "P-5D."

Piezoelectric	$d_{31}(10^{-12}m/V)$	-103
Permittivity	$\varepsilon^T_{33}/\varepsilon_0$	1370
Compliance	$s^E_{11}(10^{-12}m^2/N)$	13.2

Table 2.II. Form of the piezoelectric tensor in the crystallographic point group of *6mm*. The "•" and "·" mean non zero and null components, respectively. The line connecting the non zero components means that they are equal.

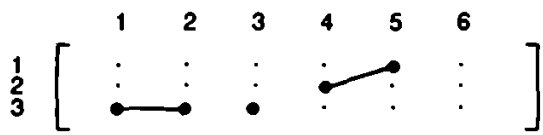

affected easily by the variation of temperature, the output of the interferometers other than the ring interferometer changes severely in a short time by the interference of the coherent optical waves. On the other hand, in the ring interferometer, the variation of the length of the fiber due to the variation of temperature can be compensated for, because the two waves travel in the same fiber; therefore, severe variation of the output does not occur in a short time.

§2.3. Measurement Using Wrap-Around Cylindrical Phase Modulator[1)]

2.3.1 Method of Measurement

For the purpose of modulating the phase of optical waves, we use a cylindrical piezoelectric transducer around which a fiber is wrapped many times in the form illustrated in Fig. 2.2. Though this type of device is often applied to a phase modulator, [8)] we are concerned with this method rather as one of the ways of measuring cylindrical piezoelectric vibration optically.

The sample shown in Fig. 2.2 is made of PZT material "P-5D," and is polarized in the direction of the radius, that is, the z-direction in Fig. 2.2. The material constants of P-5D are shown in Table 2.I. We connect the phase modulator in Fig. 2.2 with the ring interferometer in Fig. 2.1(a). The coverture around the fiber is taken off for closer fixing with the transducer, and epoxy resin is used for the fixing. In the case of the transducer illustrated in Fig. 2.2, the crystallographic point group of the material is considered to be *6mm* whose form of the piezoelectric tensor is shown in Table 2.II; therefore, when electric field E is applied between the electrodes in the z-direction, strain S can be caused in the x, y and z directions as follows,

$$S_i = d_{ji} E_j \quad (i=1,2,3;\ j=3;\ d_{31}=d_{32}), \tag{2.3.1}$$

where the subscripts 1, 2, and 3 mean the x- , the y- and the z-directions, respectively, and eq.(2.3.1) is defined exactly at the low frequency limit of S and E. Mechanical resonances can occur at the frequencies determined by the size of the transducer. The ji-mode means the vibrational mode which is derived by the piezoelectric constant d_{ji}. The resonance of 31-mode is observed at about 19 kHz in the x-direction, that is, the circumferential direction, and the resonance of 32-mode at about 58 kHz in the y-direction. The resonance of 33-mode in the z-direction can occur at higher frequencies. The piezoelectric vibration in the x-direction causes elongational vibration of the fiber.

A laser diode whose wave length λ is 1.30 μm is used as a light source for the measurement. In order to avoid unnecessary interference, a laser with low coherence, that is, with multi-mode with regard to the longitudinal mode, is selected. An avalanche photodiode is used as a photodetector. The characteristics of the single-mode glass fiber used in the experiment are shown in Table 2.III.

Table 2.III. Characteristics of the single-mode SiO_2 glass fiber used in the experiment.

Loss	0.36 dB/km
Cut-off wavelength	1.26 μm
Diameter of core	9.1 μm
Zero dispersion wavelength	1.32 μm
Diameter of fiber	124.5 μm
Eccentricity of core	0.6 μm

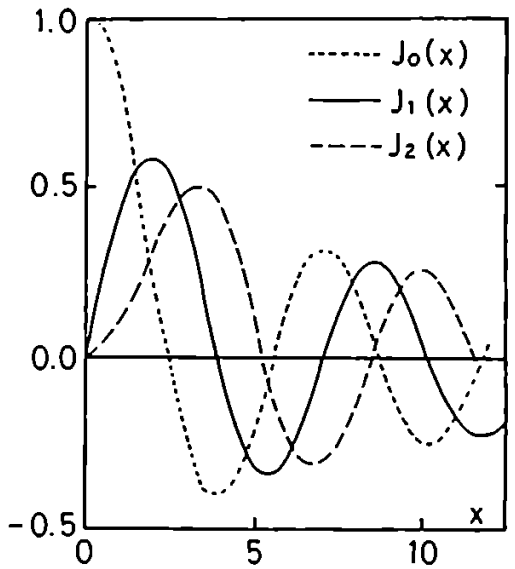

Fig. 2.3. Dependence of the Bessel functions $J_0(x)$, $J_1(x)$ and $J_2(x)$ on the independent variable x.

In the presence of piezoelectric vibration, the total elongational amplitude of the fiber, $u(t)$ [m], is expressed as

$$u(t) = m\, U_A \cos(\omega_A t + \phi_A), \tag{2.3.2}$$

where m is the number of turns (30); U_A, ω_A and ϕ_A are the one-turn elongational amplitude, a driving angular frequency, and the vibrational phase of the transducer, respectively.

If two waves counterpropagating in the ring interferometer start from the light source simultaneously, they reach the detector almost at the same time. But, assume that the clockwise wave (*CW*) reaches the phase modulator later than the counterclockwise one (*CCW*) by time T that is determined by the length of the loop and the light velocity in the fiber. Then, the two waves are modulated respectively,

$$(CW) = B' \cos\{\omega_C t + k n_C u(t+T) + \Delta\phi\}, \tag{2.3.3}$$

$$(CCW) = B' \cos\{\omega_C t + k n_C u(t)\}, \tag{2.3.4}$$

where B' is the amplitude of electric field, k [rad/m] is the wave number of light in a vacuum ($2\pi/k = 1.3\times 10^{-6}$ m), n_C is the refractive index of the fiber ($n_C = 1.47$), and $\Delta\phi$ [rad] is the phase difference between the two waves in the *absence* of the acoustic wave at the phase modulator. [7), 9)] The value of T is selected to be 1.0×10^{-6} s or 0.725×10^{-6} s.

The two waves interfere and yield voltage proportional to the intensity, that is, the time average of the square of the sum of the two electric fields expressed in eqs. (2.3.3) and (2.3.4). The detected voltage V_{PD} at the photodiode can be expressed as

$$V_{PD} = \sum_n V_{PD}(n\omega_A) \cos\{n\omega_A t + P_{PD}(n\omega_A)\}, \tag{2.3.5}$$

where

$$V_{PD}(0) = C'\{1 + \gamma \cos\Delta\phi\, J_0(\Delta\theta_A)\}, \tag{2.3.6}$$

$$V_{PD}(\omega_A) = \left| C'\gamma\, 2 \sin\Delta\phi\, J_1(\Delta\theta_A) \right|, \tag{2.3.7}$$

$$P_{PD}(\omega_A) = \phi_A + (\omega_A T/2) - (\pi/2) + P_1, \tag{2.3.8}$$

$$V_{PD}(2\omega_A) = \left| C'\gamma\, 2 \cos\Delta\phi\, J_2(\Delta\theta_A) \right|, \tag{2.3.9}$$

$$P_{PD}(2\omega_A) = 2\phi_A + \omega_A T + P_2, \tag{2.3.10}$$

where C' is the modulus proportional to the light intensity, $\gamma \approx 1$, J_i is the Bessel function of the first kind of order i, which is illustrated in Fig. 2.3, and $\Delta\theta_A$ corresponds to the phase modulation index expressed as

$$\Delta\theta_A = 2k n_C m U_A \sin(\omega_A T/2) \cdot \kappa, \tag{2.3.11}$$

where κ(= 0.778) is the correction coefficient taking the variation of the refractive index by

Table 2.IV. Form of the photoelastic tensor in the isotropic material. The notation "x" means ($p_{11} - p_{12}$) / 2.

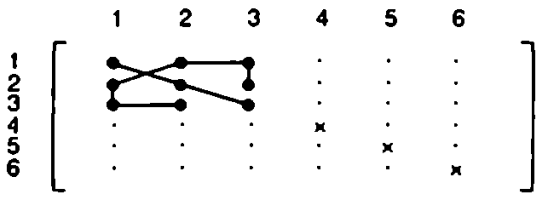

Table 2.V. Main material constants of the SiO_2 glass fiber.

Refractive index	n_{C2}	1.47
Photoelastic	p_{11}	0.121
	p_{12}	0.270
Poisson's ratio	σ	0.164

photoelasticity[10),11)] into consideration, and P_1 and P_2 are defined as

$$\begin{aligned} &P_1 = 0 \quad \text{when} \quad \sin \Delta\phi\, J_1(\Delta\theta_A) > 0, \\ &P_1 = \pi \quad \text{when} \quad \sin \Delta\phi\, J_1(\Delta\theta_A) < 0, \\ &P_2 = 0 \quad \text{when} \quad \cos \Delta\phi\, J_2(\Delta\theta_A) > 0, \\ &P_2 = \pi \quad \text{when} \quad \cos \Delta\phi\, J_2(\Delta\theta_A) < 0, \end{aligned} \tag{2.3.12}$$

The value of κ is calculated as follows. The same coordinates are chosen for the fiber as for the cylindrical transducer illustrated in Fig. 2.2; therefore, the light propagates in the x-direction in the fiber. The relative variation of the optical phase, $\Delta\theta/\theta$, can be expressed as

$$\Delta\theta/\theta = S_1 + \Delta n_C/n_C, \tag{2.3.13}$$

where S_1 is the strain of the fiber in the x-direction, and Δn_C is the variation of the refractive index of the fiber. The S_1 is now calculated by

$$S_1 = U_A / (2\pi r), \tag{2.3.14}$$

where $2\pi r$ is the outer circumference of the cylindrical transducer. The exact definition of strain will be described in §3.3. The variation of n_C can be caused mainly by photoelasticity. Photoelasticity is the phenomenon in which the refractive index n_C of material varies according to applying strain S on the material, and expressed as

$$\Delta(1/n_C^2) = (1/n_C^2) - (1/n_C^2)_{S=0} = p_{ij} S_j, \tag{2.3.15}$$

where p is the photoelastic constant, and the Einstein's summation convention is used; therefore, a summation from 1 to 3 is taken for the repeated indices in the same term. The form of the photoelastic tensor is shown in Table 2.IV, where the glass is assumed to be isotropic. From eq.(2.3.15) and Table 2.IV, the variation of the refractive index of the propagating light, whose polarization is in the y- or z-direction, is expressed as

$$\Delta(1/n_C^2) = \Delta(1/n_{C2}^2) = -2\Delta n_{C2}/n_{C2}^3 = p_{21} S_1 + p_{22} S_2 + p_{21} S_3 . \tag{2.3.16}$$

Therefore, $\Delta n_{C2}/n_{C2}$ is expressed as

$$\Delta n_{C2}/n_{C2} = -(n_{C2}^2/2)\{p_{21}(1-\sigma) - \sigma p_{22}\} S_1, \tag{2.3.17}$$

where Poisson's ratio σ of the fiber is defined as $S_2 = S_3 = -\sigma S_1$. From eqs. (2.3.13) and (2.3.17),

$$\Delta\theta/\theta \equiv \kappa S_1 = [\, 1 - (n_{C2}^2/2)\{p_{21}(1-\sigma) - \sigma p_{22}\}\,] S_1. \tag{2.3.18}$$

The material constants of the fiber necessary for the calculation are shown in Table 2.V. Substitution of the value in Table 2.V into eq.(2.3.18) gives $\kappa = 0.778$. This means that 77.8% of the

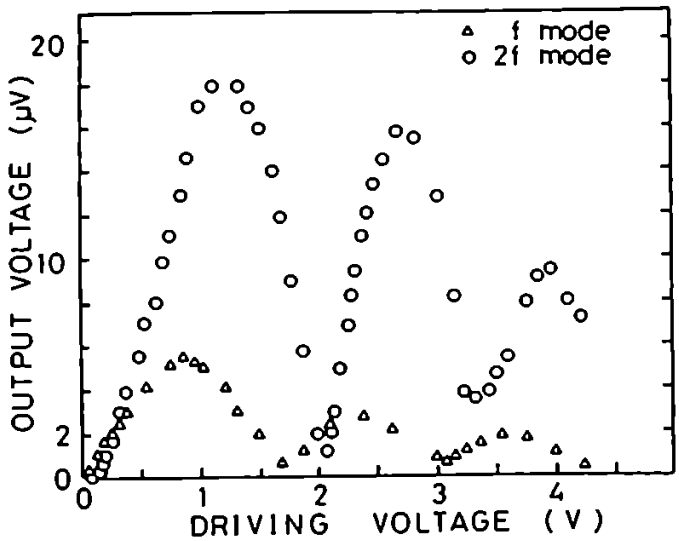

Fig. 2.4. Dependence of the output voltage V_{PD} (ω_A and $2\omega_A$ components) at the lock-in amplifier on the driving voltage V_{DR} of the transducer at a frequency $f = \omega_A/(2\pi)$ = 20 (kHz).

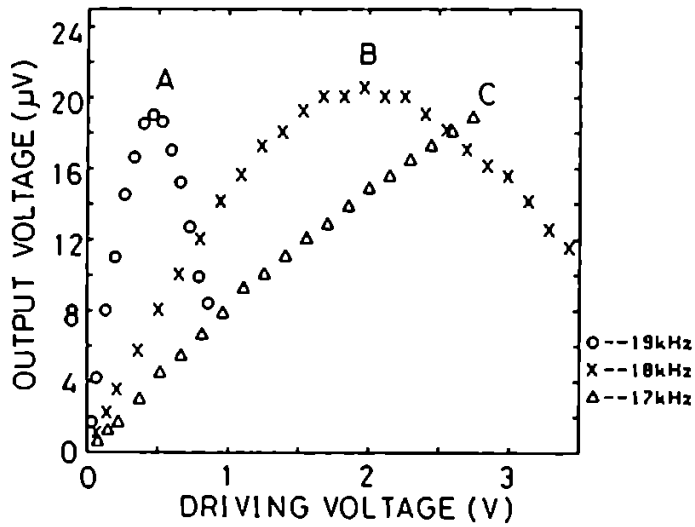

Fig. 2.5. Difference of the relation between the driving voltage V_{DR} of the transducer and the output voltage V_{PD} of ω_A components at the lock-in amplifier by changing the driving frequency (A : 19 kHz, B : 18 kHz, C : 17 kHz).

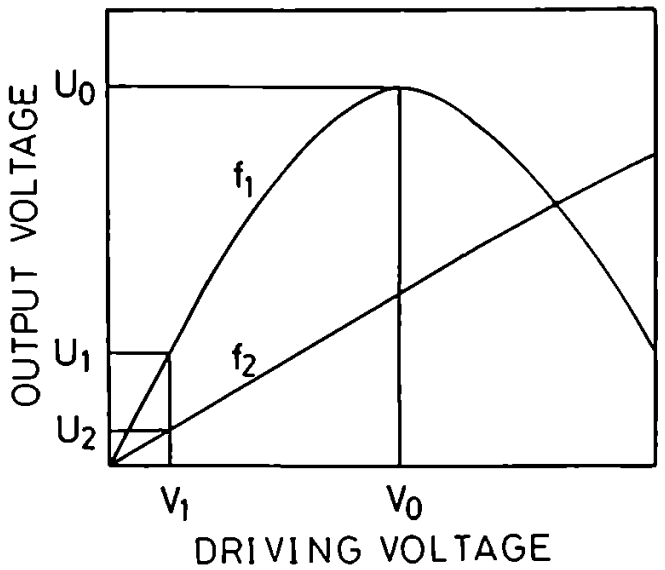

Fig. 2.6. Graphical method of determining the relation between $\Delta 0_A$ and V_{DR} when the experimental curve of relation between V_{PD} and V_{DR} does not have the maximum. The feature that $J_1(x)$ is almost linear at $x < 0.4$ is used.

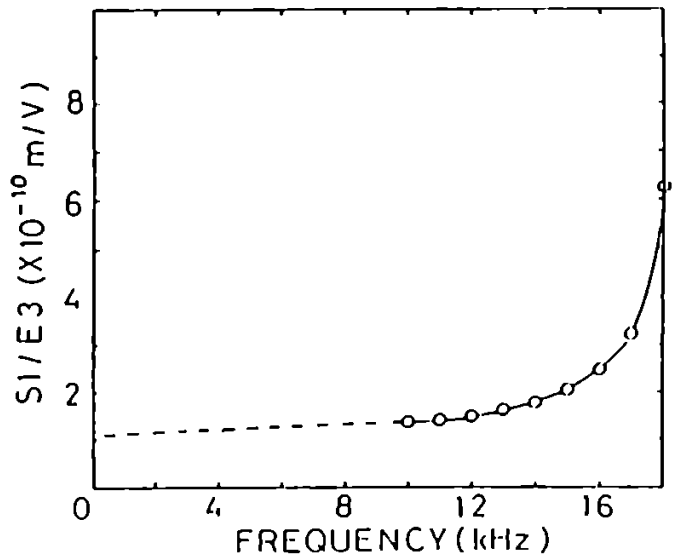

Fig. 2.7. Frequency characteristic of the S_1 / E_3 lower than the resonance frequency. The value of S_1 / E_3 at a zero frequency can be conjectured.

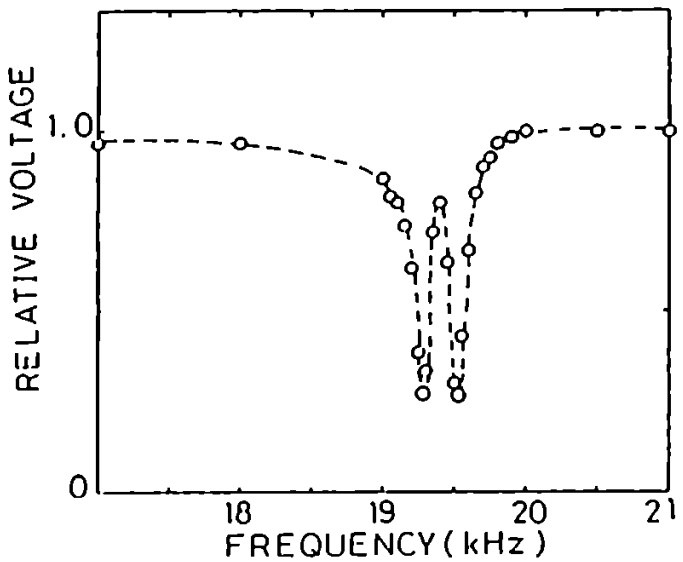

Fig. 2.8. Decrease of the driving voltage V_{DR} between the electrodes near the resonance frequency.

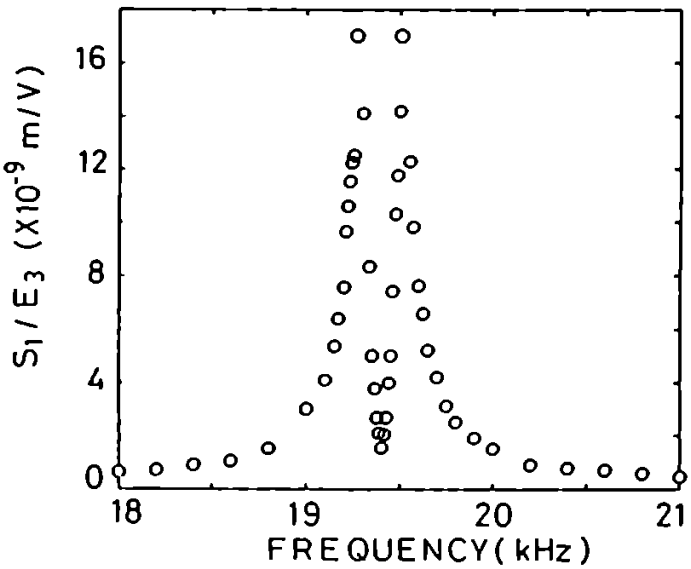

Fig. 2.9. Frequency characteristic of S_1/E_3 near the resonance frequency.

strain contributes to the relative variation of the optical phase.

The output voltage at the photodiode, V_{PD}, is detected in a narrow band of the frequency by using a lock-in amplifier.

2.3.2 Measurement of $\Delta\theta_A$ and Strain of Sample

Figure 2.4 shows the relation between the driving voltage of the transducer and the output voltage of ω_A and $2\omega_A$ components at the lock-in amplifier. With regard to the abscissa, experimental curves conform to $J_1(\Delta\theta_A)$ and $J_2(\Delta\theta_A)$, respectively, as is expected from eqs. (2.3.7) and (2.3.9). Since the abscissa of Fig. 2.4 is the driving voltage V_{DR}, we find that $\Delta\theta_A$ is in proportion to V_{DR}. And then, from eq.(2.3.11), we can conclude logically that U_A is in proportion to V_{DR}. This is an experimental confirmation of the piezoelectric effect using the optical method. With regard to the ordinate of Fig. 2.4, the experimental curves do not coincide with $J_1(\Delta\theta_A)$ and $J_2(\Delta\theta_A)$, because of the variation of light intensity or the value of $\Delta\phi$ during the experiment.

Figure 2.5 shows the experimental results (ω_A components) after changing the driving frequency. The curves A and B have their maxima. In such a case, we can determine the relation between $\Delta\theta_A$ and V_{DR}, or the ratio of U_A to V_{DR}, utilizing the feature that $J_1(x)$ has the first maximum at $x = 1.84$. When there is no maximum as in curve C in Fig. 2.5, we can utilize the feature that $J_1(x)$ is almost linear in $x<0.4$. By setting the driving voltage in this range, and comparing these results with those for curves A and B, the ratio of U_A to V_{DR} for the curve C can be obtained. This method is explained graphically in Fig. 2.6.

The frequency characteristic of the amplitude in the range lower than the resonance frequency is shown in Fig. 2.7 whose ordinate is now translated into the ratio of S_1 to E_3, the strain in the direction of circumference to the electric field in the direction of the radius. Examining the results of Fig. 2.7, we can extrapolate the value of S_1/E_3 to the zero frequency and obtain S_1/E_3 at the low frequency limit as 1.1×10^{-10} m/V, which should correspond to the piezoelectric constant d_{31} by definition. To avoid confusion with the material constant d_{31}, we name the value obtained by our measurement "d'_{31}." The value of d'_{31} is nearly in agreement with that of d_{31}(-1.03×10^{-10} m/V) shown in Table 2.I.

Near the resonance, the driving voltage V_{DR} between the electrodes decreases, as in Fig.2.8. The frequency characteristic of S_1/E_3, obtained by the method mentioned above near the resonance frequency, is shown in Fig. 2.9, from which we can read the maximum of S_1/E_3 as 1.70×10^{-8} m/V and the Q-value as 161. The value of d'_{31} can also be obtained by the following equation:

$$d'_{31} = \frac{S_1/E_3\ (\text{maximum})}{Q}\ , \qquad (2.3.19)$$

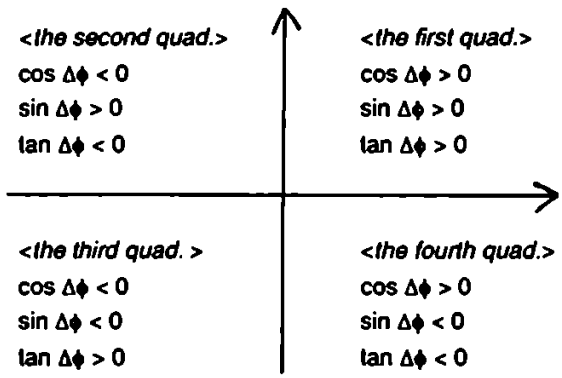

Fig. 2.10. Algebraic sign of cosΔϕ, sinΔϕ and tanΔϕ in the respective quadrants.

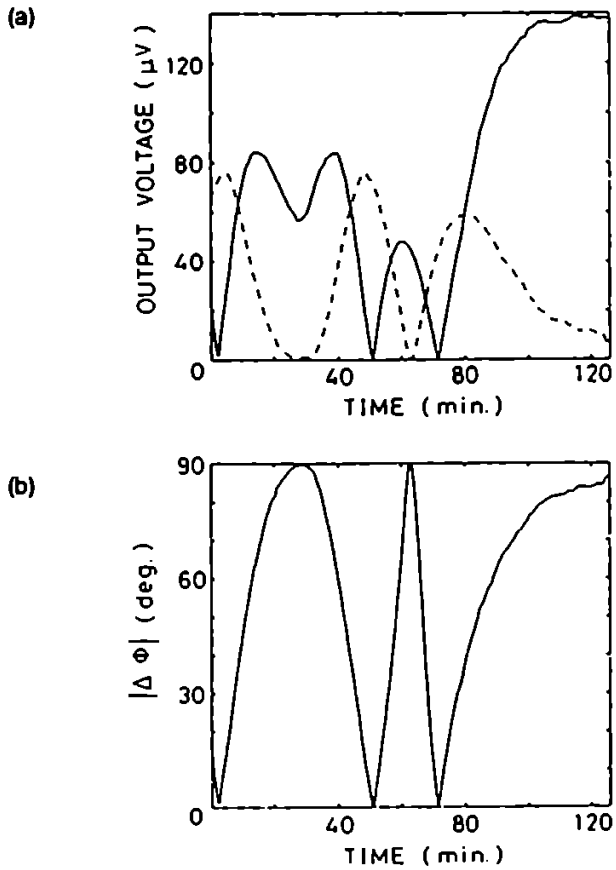

Fig. 2.11. (a) Time variation of the value of $V_{PD}(\omega_A)$ (solid line) and $V_{PD}(2\omega_A)$ (dashed line). (b) Time variation of the value of Δϕ calculated by eq.(2.3.21).

where we must use the value at the first resonance. Using eq.(2.3.19), we can obtain the value of d'_{31} as 1.06×10^{-10}m/V, which is nearly in agreement with that of d_{31} shown in Table 2.I. The grounds for eq.(2.3.19) will be described in §3.7.

2.3.3 Calculation of $\Delta\phi$

The value of $\Delta\phi$ can be calculated by the analysis of the interferometer output expressed in eqs. (2.3.6), (2.3.7) and (2.3.9). The ratio of $V_{PD}(\omega_A)$ to $V_{PD}(2\omega_A)$ gives

$$| \tan\Delta\phi | = \frac{J_2(\Delta\theta_A)\, V_{PD}(\omega_A)}{J_1(\Delta\theta_A)\, V_{PD}(2\omega_A)}. \tag{2.3.20}$$

The Bessel function $J_1(x)$ has the first maximum value as 0.582 at $x = 1.84$, then, $J_2(x)$ does not become the maximum, and has the value as 0.316. Therefore, we set such value of the driving voltage of the phase modulator as the output voltage at the angular frequency ω_A becomes the first maximum; that is, $\Delta\theta_A = 1.84$, then, by the measurement of $V_{PD}(\omega_A)$ and $V_{PD}(2\omega_A)$, we can obtain

$$| \tan\Delta\phi | = \frac{0.316\, V_{PD}(\omega_A)}{0.582\, V_{PD}(2\omega_A)}. \tag{2.3.21}$$

In the measurement of $V_{PD}(\omega_A)$ and $V_{PD}(2\omega_A)$, we must pay attention to the different frequency characteristics of the photodiode at the two frequencies, and correct the value before substituting eq.(2.3.21).[12]

At this stage, $\Delta\phi$ may have four values in the respective quadrants, as illustrated in Fig. 2.10. From eq.(2.3.6) we can determine the algebraic sign of $\cos\Delta\phi$. The Bessel function $J_0(x)$ has the maximum value at $x = 0$, and the value of $J_0(x)$ decreases at $x > 0$ in an appropriate range, compared with the value at $x = 0$. If the value of V_{PD}, when the phase modulator is at the state of $\Delta\theta_A > 0$ in an appropriate range, decreases compared with the value when the phase modulator is not driven; that is, $\Delta\theta_A = 0$, we can determine that $\cos\Delta\phi > 0$. If the contrary result is obtained, $\cos\Delta\phi < 0$ is found. Accordingly, we can obtain the value of $\cos\Delta\phi$ and $| \sin\Delta\phi |$ by this method. In the actual measurement to determine the algebraic sign of $\cos\Delta\phi$, the light source is intensity-modulated at an angular frequency ω_L, and the output of $V_{PD}(\omega_L)$ is detected, instead of that of $V_{PD}(0)$, in order to use the lock-in amplifier which can detect ac signal, but cannot detect the dc signal. Figure 2.11(a) shows time variation of the value of $V_{PD}(\omega_A)$ and $V_{PD}(2\omega_A)$, and Fig. 2.11(b) shows time variation of the value of $\Delta\phi$ calculated by eq.(2.3.21).

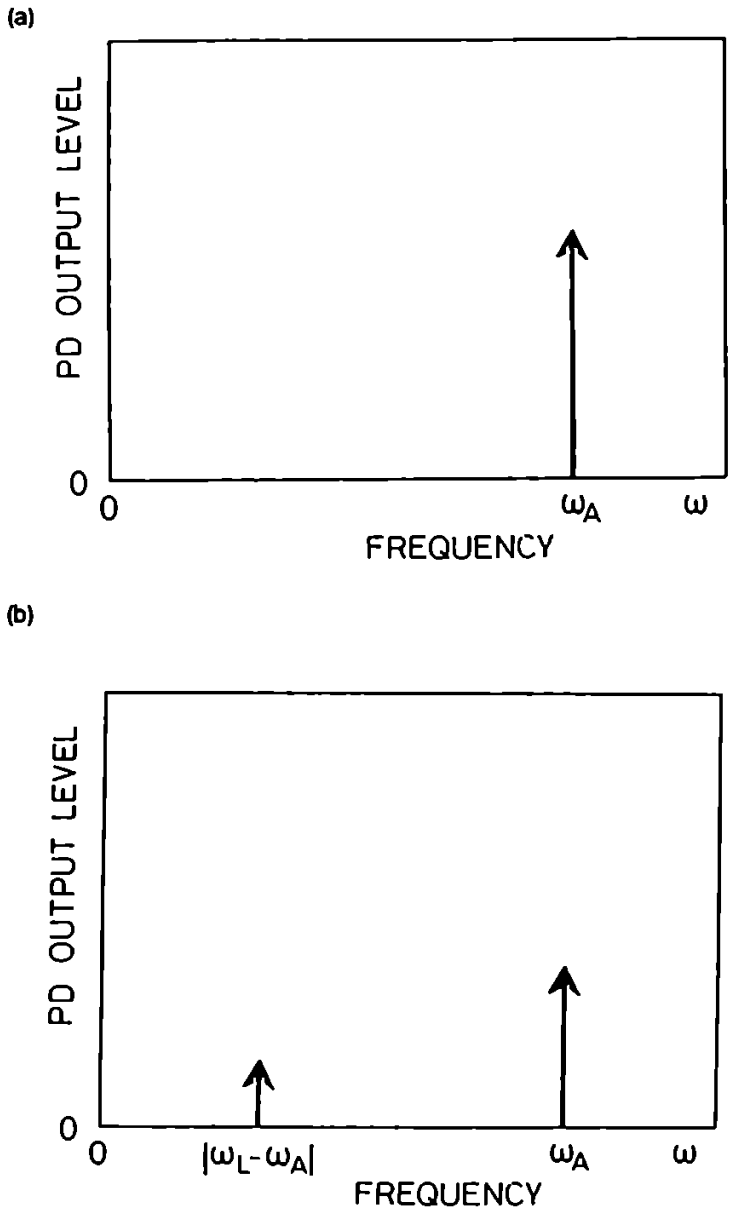

Fig. 2.12. (a) Spectrum analysis of the idealized signal of ω_A component detected at the photodiode. (b) Signal of $|\omega_A - \omega_L|$ component is generated due to the intensity modulation of the light source at an angular frequency ω_L.

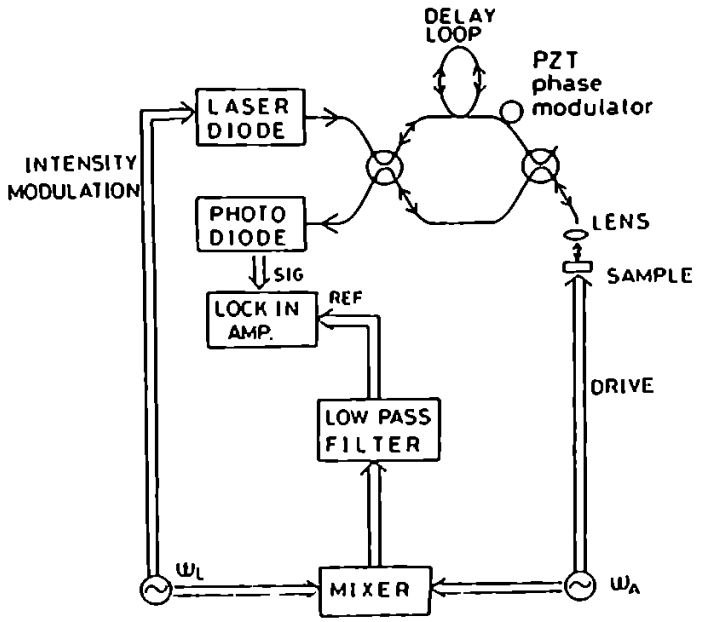

Fig. 2.13. Electrical and optical experimental configuration for the measurement of acoustic wave by reflection of light on the sample surface.

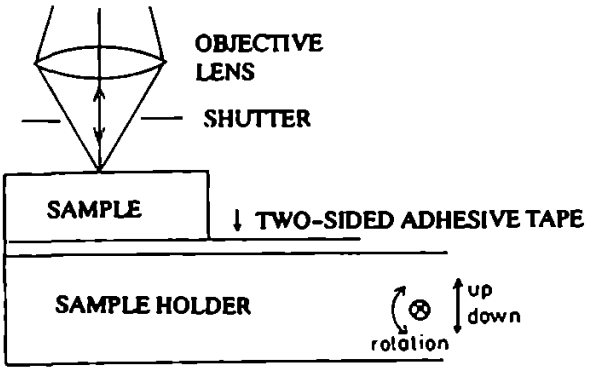

Fig. 2.14. The light emitted from the fiber is focused on the sample surface by the objective lens, reflected, and returns in the fiber. The sample is fixed lightly on the sample holder by means of two-sided adhesive tape. The shutter is used for distinction between the light reflected by the sample and other lights.

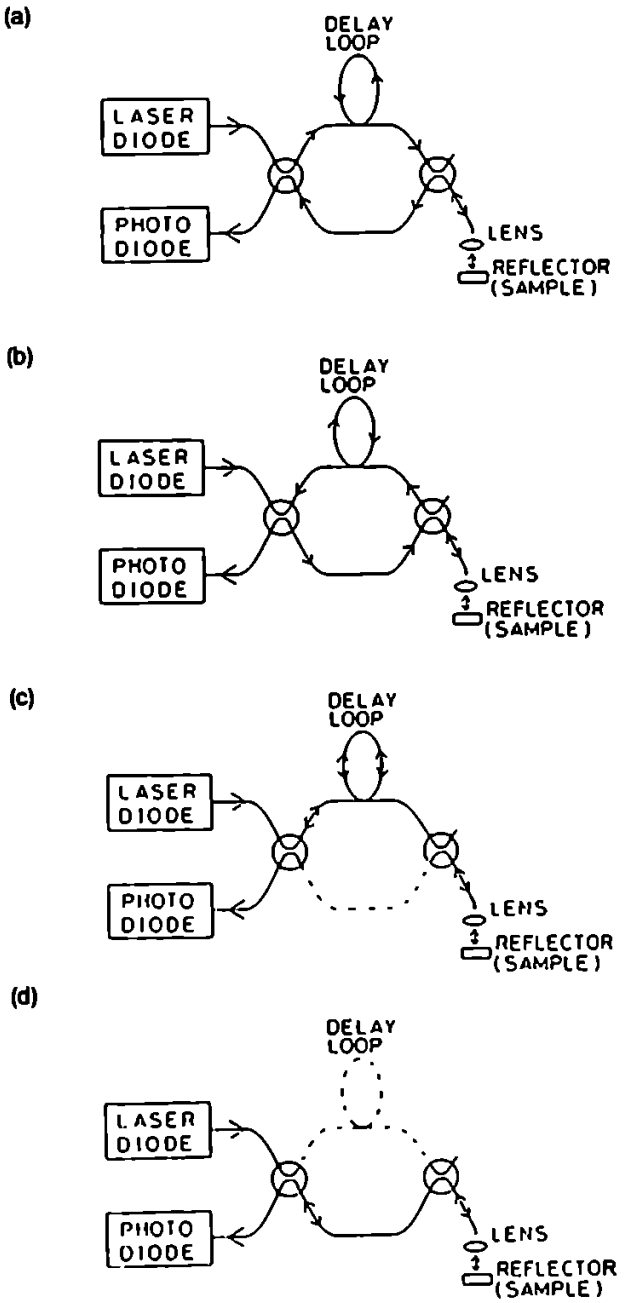

Fig. 2.15. Four possible paths of the light in the fiber. (a) clockwise, (b) counterclockwise, (c) and (d) the other paths.

§2.4. Measurement by Reflecting Light on Sample Surface[3)]

2.4.1 Outline of Measurement Method

Another measurement of piezoelectric vibration can be performed by reflecting light on a sample surface. The light is phase-modulated by reflection when the sample vibrates. The ring interferometer is used for transformation of the phase-modulated signal to the intensity-modulated one. The lock-in amplifier is used for detection of the output voltage V_{PD} at the photodiode. However, the lock-in amplifier can only measure high frequency up to approximately 100 kHz. In order to measure the acoustic vibration whose angular frequency ω_A is higher than the limit of the lock-in amplifier, the light source, a laser diode, is intensity-modulated at the angular frequency ω_L. Interference of the two optical waves phase-modulated by acoustic vibration causes an intensity-modulated optical wave, the components of which have an angular frequency $n\omega_A$ (n=0,1,2,$\cdots$). The light itself is now intensity-modulated at the angular frequency ω_L. Therefore, signals whose frequencies are the sum and the difference between the two frequencies ω_L, $|\omega_A \pm \omega_L|$, $|2\omega_A \pm \omega_L|$, etc. can occur. The signals whose angular frequencies are lower than the limit frequency of the lock-in amplifier can be detected and used for the measurement of the acoustic vibration. Figures 2.12(a) and 2.12(b) illustrate the generation of $|\omega_A - \omega_L|$ component due to the intensity modulation of the light source at the angular frequency ω_L.

2.4.2 Experimental system

The experimental configuration is shown in Fig. 2.13. The wrap-around phase modulator described in §2.3 is still connected to the ring interferometer. In order to supply the electric reference signal whose angular frequencies are ω_L, $|\omega_A - \omega_L|$ and $|2\omega_A - \omega_L|$ for the lock-in amplifier, a double-balanced mixer is used for the frequency mixing. The light emitted from the fiber is focused on the sample surface by objective lens, reflected, and returned to the fiber, as illustrated in Fig. 2.14. The sample is fixed lightly on the sample holder by means of two-sided adhesive tape. The shutter is used for distinguishing between the light reflected by the sample and other light.

In the experimental configuration shown in Fig. 2.13, optical paths other than the clockwise and counterclockwise paths exist. Figures 2.15 (a), (b), (c) and (d) show the four possible paths of the light in the fiber: clockwise, counterclockwise, and two other paths, respectively. The lights in the clockwise and the counterclockwise paths can interfere with each other, while the other two lights cannot interfere with the lights in the clockwise and the counterclockwise paths, because the other two lights reach the photodiode at a different time which is now determined to

be longer than the coherent time of the light.

2.4.3 Formulation of Measurement Method

The *intensity* of the lights at the photodiode whose paths are shown in Figs. 2.15 (a), (b), (c) and (d) can be expressed as

$$I_a = A'_a \{ 1 + D' \cos(\omega_L t + \omega_L T) \}, \tag{2.4.1}$$

$$I_b = A'_b \{ 1 + D' \cos(\omega_L t + \omega_L T) \}, \tag{2.4.2}$$

$$I_c = A'_c \{ 1 + D' \cos(\omega_L t + 2\omega_L T) \}, \tag{2.4.3}$$

$$I_d = A'_d (1 + D' \cos\omega_L t), \tag{2.4.4}$$

respectively, where the lights are intensity-modulated with the modulation index D' ($0 \le D' \le 1$) at the angular frequency ω_L.

The two coherent lights whose paths are shown in Figs. 2.15(a) and 2.15(b) are phase-modulated by the acoustic vibration to be measured at the angular frequency ω_A as

$$E_a = B'_a \cos \{ \omega_C + 2kU_A \cos(\omega_A t + \omega_A T + \phi_A) + \Delta\phi \}, \tag{2.4.5}$$

$$E_b = B'_b \cos \{ \omega_C + 2kU_A \cos(\omega_A t + \phi_A) \}, \tag{2.4.6}$$

respectively, where E_a and E_b are the electric fields of the lights, B'_a and B'_b are their *amplitudes*. Though eqs. (2.4.5) and (2.4.6) are similar to eqs. (2.3.3) and (2.3.4) in the case of the wrap-around phase modulator, the optical paths in eqs. (2.4.5) and (2.4.6) are $2/n_C$ times as long as those in eqs. (2.3.3) and (2.3.4), because the reflection makes the optical path twice, and the present phase-modulation is performed in air.

Since the two coherent lights whose paths are shown in Figs. 2.15(a) and 2.15(b) can interfere with each other, the square of the sum of the electric fields is detected at the photodiode. Since the other two incoherent lights whose paths are shown in Figs. 2.15 (c) and 2.15(d) cannot interfere with each other and with the lights whose paths are shown in Figs. 2.15 (a) and 2.15(b), each of the intensities is detected at the photodiode. Therefore, the output voltage V_{PD} at the photodiode can be expressed as

$$V_{PD} \propto I_a + I_b + 2\gamma(I_a I_b)^{1/2} \cos\Delta\theta + I_c + I_d, \tag{2.4.7}$$

where $\gamma \approx 1$, and $\Delta\theta$ is the phase difference between the two coherent lights and is expressed as

$$\Delta\theta = \Delta\phi + \Delta\theta_A \cos \{\omega_A t + (\text{terms on phase})\}, \tag{2.4.8}$$

where $\Delta\theta_A$ is expressed as

$$\Delta\theta_A = 4kU_A \sin(\omega_A T/2), \tag{2.4.9}$$

similar to eq.(2.3.11). The output voltage V_{PD} in eq.(2.4.7) can be expressed as

$$V_{PD} = \sum_n V_{PD}(\mid n\omega_A \pm \omega_L \mid) \cos \{(n\omega_A \pm \omega_L)t + P_{PD}(n\omega_A \pm \omega_L)\}. \qquad (2.4.10)$$

In eqs. (2.4.1) to (2.4.4), if the intensity of the four lights are the same; that is, $A'_a : A'_b : A'_c : A'_d = 1 : 1 : 1 : 1$, and if the phase difference of the *intensity-modulation* does not exist among the four lights; that is, $\omega_L T = 0$, the amplitude of V_{PD} in eq.(2.4.10) can be expressed as

$$V_{PD}(\omega_L) \equiv K_0 = C'D' \{2+ \gamma \cos\Delta\phi J_0(\Delta\theta_A)\}, \qquad (2.4.11)$$

$$V_{PD}(\mid \omega_A - \omega_L \mid) \equiv K_1 = \mid C'D' \gamma \sin\Delta\phi J_1(\Delta\theta_A) \mid , \qquad (2.4.12)$$

$$V_{PD}(\mid 2\omega_A - \omega_L \mid) \equiv K_2 = \mid C'D' \gamma \cos\Delta\phi J_2(\Delta\theta_A) \mid , \qquad (2.4.13)$$

where C' is in proportion to the intensity of the light, D' is the intensity-modulation index of the light source, as expressed in eqs. (2.4.1) to (2.4.4), and $\gamma = 1$.

The angular frequencies ω_L, $\mid \omega_A - \omega_L \mid$ and $\mid 2\omega_A - \omega_L \mid$ are selected in the range of the limit frequency of the lock-in amplifier, for example, below 100 kHz, and selected to be the same value in order to cancel out the different frequency characteristics of the photodiode at lower frequency than 100 kHz. For this reason, the angular frequencies ω_L in eqs. (2.4.11), (2.4.12) and (2.4.13) are different from one another, and the intensity-modulation index D' of the light source must be the same in the selected frequency range of ω_L. Figures 2.16(a) and 2.16(b) show the frequency characteristics of the intensity-modulation in the experiment. This measurement was performed using a tracking generator, which is constructed using the generator and detector of the electrical signal whose frequency can be swept, as illustrated in Fig. 2.16(c).

Equation (2.4.11) is similar to eq.(2.3.6); however, in the term "2," the incoherent lights contribute to the factor "1," while the coherent lights contribute to the remaining factor "1." In the actual experiment, the phase difference of the intensity-modulation in eqs. (2.4.1) to (2.4.4), $\omega_L T$, is not zero, as is illustrated in Fig. 2.17. The sum of the intensity-modulated signals with the phase difference decreases the ω_L component. The ω_L component reaches its maximum when $\omega_L T = 2n\pi$, and its minimum when $\omega_L T = (2n+1)\pi$ $(n = 0, 1, 2, \cdots)$. Figure 2.18(a) shows the experimental result of the value of $V_{PD}(\omega_L)$ after changing the value of ω_L. This measurement was performed using a tracking generator, as illustrated in Fig. 2.18(b). This effect changes the term "2" in eq.(2.4.11).

The difference of the intensity of the four lights also changes the term "2" in eq.(2.4.11). The ω_L component involved in eq.(2.4.7) can be expressed as

(a)

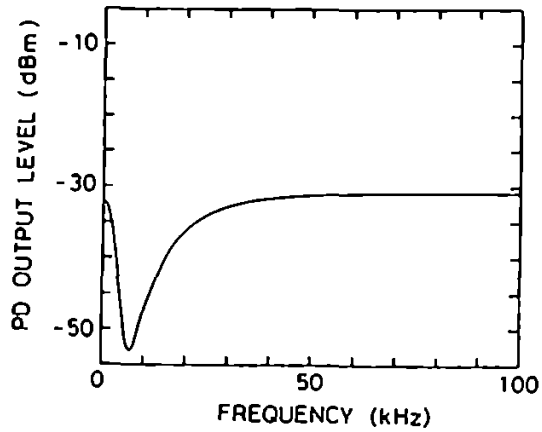

(b)

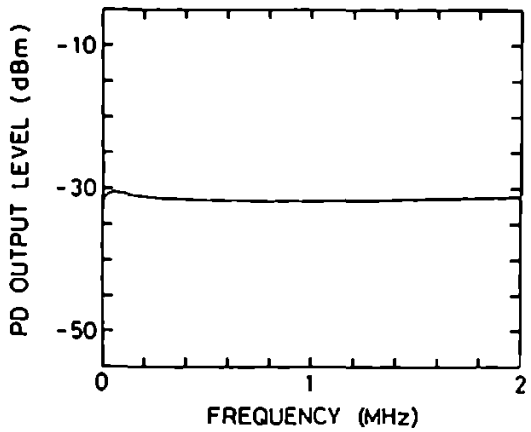

(c)

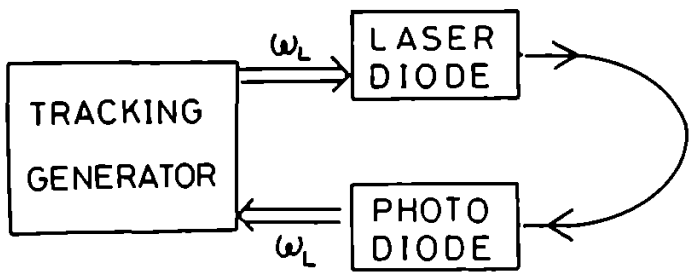

Fig. 2.16. Frequency characteristics of the intensity-modulation in the experiment. (a) Frequency characteristic below 100 kHz. (b) Frequency characteristic below 2 MHz. (c) Experimental configuration of this measurement.

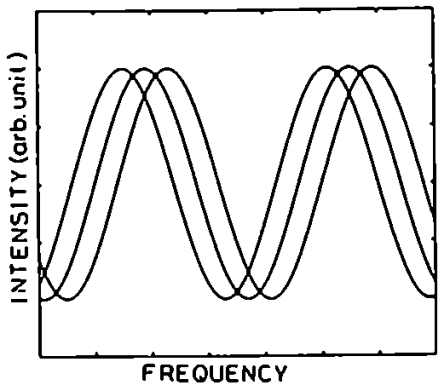

Fig. 2.17. Phase difference of four kinds of the intensity-modulated lights. This phase difference will occur, unless $\omega_L T = 2n\pi$ (n= 0, 1, 2,···).

(a)

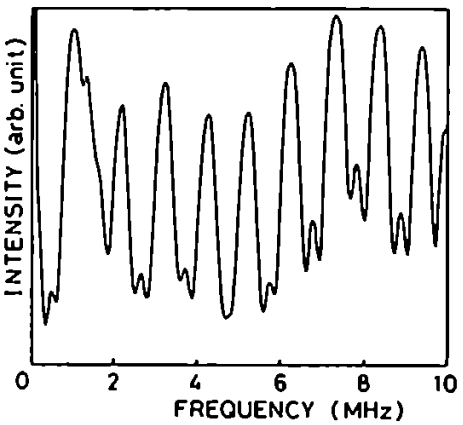

(b)

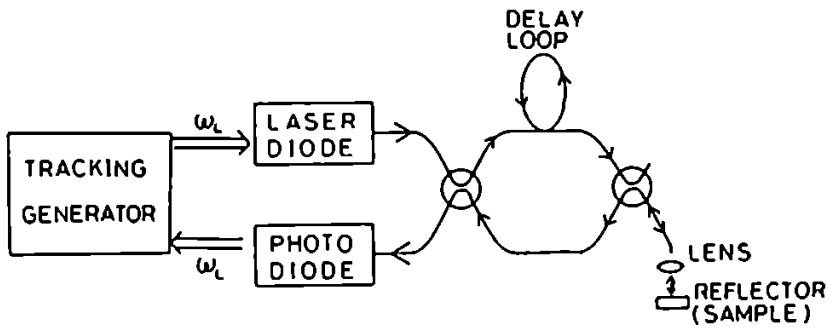

Fig. 2.18 (a) Experimental result of the value of $V_{PD}(\omega_L)$ after changing the value of ω_L. (b) Experimental configuration of this measurement.

$$V_{PD}(\omega_L) = \frac{C'D'}{2(A'_a A'_b)^{1/2}} \{(A'_{ab}\cos\omega_L T + A'_c\cos 2\omega_L T + A'_d)^2$$

$$+ (A'_{ab}\sin\omega_L T + A'_c\sin 2\omega_L T)^2\}^{1/2}, \quad (2.4.14)$$

where

$$A'_{ab} = A'_a + A'_b + 2(A'_a A'_b)^{1/2}\,\gamma\cos\Delta\phi\, J_0(\Delta\theta_A). \quad (2.4.15)$$

In our experiment,

$$A'_a : A'_b : A'_c : A'_d = 19.3 : 88.0 : 82.6 : 20.6, \quad (2.4.16)$$

and when $V_{PD}(\omega_L)$ is measured, ω_L is selected to be $\omega_L T << 1$. Then, eq.(2.4.14) approximates

$$V_{PD}(\omega_L) \equiv K_0 = C'D'\{E' + \gamma\cos\Delta\phi\, J_0(\Delta\theta_A)\}, \quad (2.4.17)$$

where $\gamma \approx 1$, and

$$E' = 1.46 + 1.10\cos\omega_L T. \quad (2.4.18)$$

For example, $E' = 2.53$ in our experiment when $\cos\omega_L T = 0.975$. Therefore, the value of E' is larger than 2 in the ideal case expressed in eq.(2.4.11).

In the measurement of the piezoelectric vibration by the *reflection* of the light, the value of $\Delta\theta_A$ in eq.(2.4.9) is considered to be $\Delta\theta_A << 1$; therefore, the approximation that

$$J_0(\Delta\theta_A) \approx 1, \quad (2.4.19)$$

$$J_1(\Delta\theta_A) \approx \Delta\theta_A/2, \quad (2.4.20)$$

$$J_2(\Delta\theta_A) \approx (\Delta\theta_A)^2/8, \quad (2.4.21)$$

can be used. In this case, from eqs. (2.4.12), (2.4.13) and (2.4.17), two unknown quantities C' and D' can be eliminated, and two unknown quantities $\cos\Delta\phi$ and $\Delta\theta_A$ can be calculated by

$$\text{when } \cos\Delta\phi > 0, \quad \cos\Delta\phi = \{ -E'K_1^2 + (E'^2K_1^4 + F')^{1/2} \}/G', \quad (2.4.22)$$

$$\text{when } \cos\Delta\phi < 0, \quad \cos\Delta\phi = \{ -E'K_1^2 + (E'^2K_1^4 + H')^{1/2} \}/I', \quad (2.4.23)$$

where

$$F' \equiv 8K_0K_2(K_1^2 + 2K_0K_2), \quad (2.4.24)$$

$$G' \equiv 2(K_1^2 + 2K_0K_2), \quad (2.4.25)$$

$$H' \equiv -8K_0K_2(K_1^2 - 2K_0K_2), \quad (2.4.26)$$

$$I' \equiv 2(K_1^2 - 2K_0K_2), \quad (2.4.27)$$

and

$$\Delta\theta_A = \frac{2(E' + \cos\Delta\phi)K_1}{|\ \sin\Delta\phi\ |\ K_0} P_A , \tag{2.4.28}$$

where

$$P_A = 1 \quad \text{when } \sin(\omega_A T/2) > 0,$$
$$P_A = -1 \quad \text{when } \sin(\omega_A T/2) < 0. \tag{2.4.29}$$

The different formulae (2.4.22) and (2.4.23) are used for the different algebraic sign of cos $\Delta\phi$.

In fact, the algebraic sign of cos$\Delta\phi$ cannot be measured by the methods mentioned above in this section, and when $\Delta\theta_A$ is too small, the value of K_2 in eq.(2.4.13) cannot be measured, because K_2 includes the factor of $(\Delta\theta_A)^2$. Therefore, the wrap-around phase modulator connected to the present ring interferometer is used for the calculation of cos$\Delta\phi$ and $|\ \sin\Delta\phi\ |$, as described in §2.3.3. Then, we can calculate the value of $\Delta\theta_A$ by using eq.(2.4.28), which does not include K_2, and the value of U_A, which we hope to arrive at by operation of eq.(2.4.9).

In our measurement, the sensitivity of the amplitude measurement is about 0.1 nm so long as the power of the light source is about 1 mW and about 5 % of the light returns to the fiber.

With regard to the phase of V_{PD} in eq.(2.4.10), we can obtain experimentally that

$$\text{when } \omega_A > \omega_L,\ P_{PD}(|\ \omega_A - \omega_L\ |) = \phi_A + \omega_A T/2 - \pi/2 + P_1 + \phi' + \phi^{\circ}, \tag{2.4.30a}$$

$$\text{when } \omega_A < \omega_L,\ P_{PD}(|\ \omega_A - \omega_L\ |) = -\phi_A - \omega_A T/2 + \pi/2 + P_1 + \phi' - \phi^{\circ}, \tag{2.4.30b}$$

$$\text{when } 2\omega_A > \omega_L,\ P_{PD}(|\ 2\omega_A - \omega_L\ |) = 2\phi_A + \omega_A T + P_2 + \phi^{\circ\circ} + \phi^{\circ\circ\circ}, \tag{2.4.31a}$$

$$\text{when } 2\omega_A < \omega_L,\ P_{PD}(|\ 2\omega_A - \omega_L\ |) = -2\phi_A - \omega_A T + P_2 + \phi^{\circ\circ} - \phi^{\circ\circ\circ}, \tag{2.4.31b}$$

where ϕ' and ϕ° are additional terms dependent on the experimental system, and symmetric and asymmetric terms on the algebraic sign of $\omega_A - \omega_L$, respectively. The terms $\phi^{\circ\circ}$ and $\phi^{\circ\circ\circ}$ are similar and correspond to ϕ' and ϕ°, respectively.

The application of this measurement to the evaluation of piezoelectric transducers will be described in the next chapter. Main experimental conditions are summarized in Table 2.VI.

§2.5. Summary

In this chapter, two new methods for measurement of piezoelectric vibration using the fiber-optic ring interferometer were described. In one method, the sample is in contact with a fiber, on which the light is phase-modulated by piezoelectric vibration. In this case, the fiber is wrapped many turns around a cylindrical piezoelectric transducer. The low frequency limit of S_1 / E_3 measured by this method was nearly in agreement with the material constant d_{31}. In the other method, the light is incident on the sample surface and phase-modulated by reflection

when the sample vibrates. The formulation of this method was described herein.

Reference

1) M.Ohki, N.Shima and T.Shiosaki: *Proc. 12th Symp. Ultrasonic Electronics, Tokyo, 1991*, Jpn.J.Appl.Phys., **31**(1992) Suppl.31-1, p.105

2) M.Ohki, N.Shima and T.Shiosaki: IEICE Tech.Rep., US90-71,EA90-84 (1991.1.25) [in Japanese]

3) M.Ohki, T.Kita and T.Shiosaki: IEICE Tech.Rep., US91-23 (1991.7.16) [in Japanese]

4) M.Ohki and T.Shiosaki: *Proc. IEEE Ultrasonics Symp.,Florida, 1991* (IEEE, Piscataway, 1991) p.615

5) M.Ohki, N.Shima and T.Shiosaki: Jpn.J.Appl.Phys., **32**(1993) 2463.

6) R.Ulrich: Optics Lett., **5** (1980), 173.

7) K.E.Bowers, R.L.Jungerman, B.T.Khuri-Yakub and G.S.Kino: Jour.Lightwave Tech. **LT-1** (1983) 429.

8) S.A.Kingsley: Electron. Lett. **14** (1978) 419.

9) T.Ohkoshi *et al.*: *Hikari Faiba Sensa* (Optical Fiber Sensors) (Ohmusha,Tokyo,1986) Chapters 6 and 7 [in Japanese] .

10) T.Ohkoshi *et al.*: *Hikari Faiba Sensa* (Optical Fiber Sensors) (Ohmusha,Tokyo,1986) Chapter 2 [in Japanese] .

11) E.N.Kingsley and S.A.Kingsley: Electron. Lett. **10** (1975) 21.

12) N. Shima: Thesis for Master of Engineering, Kyoto Univ. (1992) [in Japanese]

Table 2.VI. Main experimental conditions of the measurement.

Laser diode	NEC OD-8326 or Fujitsu FLD130D413J:
	λ = 1.30μm, 1 mW, low coherence
Avalanche photodiode	Anritsu MZ118A+MH923A
Optical Fiber	Furukawa Electric Co.,Ltd. Single mode (SiO_2)
	loss = 0.36 dB/km, delay loop = 200 or 145 m
Double balanced mixer	R&K Co.,Ltd. M5: isolation > 35dB
Lock-in Amplifier	NF 5610B: measured at 100kHz,
	time const. = 1 or 3 s.
XYZ pulse stage	Chuo-Seiki Co.,Ltd. PS-10Z20XY, CPC-3C
Sample holder	General Scanning Co.,Ltd. M6300PD

Chapter 3
Optical and Electromechanical Evaluation of Piezoelectric Vibration

§3.1. Introduction

The optical measurement methods using the ring interferometer described in Chapter 2 enable us to evaluate the acoustic amplitude and phase of the piezoelectric transducer. In particular, the method in which light is reflected on the sample surface described in §2.4 enables us to evaluate the acoustic vibration locally by adjusting the measurement point where the light is incident. In this chapter, measurement of the amplitude and phase of piezoelectric vibration is performed by this method.

An electromechanical method is usually used for the evaluation of piezoelectric vibration. The relationship between voltage and current in the piezoelectric transducer can be measured; that is, admittance is measured when voltage is constant with this method. The electromechanical coupling coefficient can be calculated by means of this method; however, this measurement is not local. The characteristics of the sample are measured as a whole. Acoustic amplitude and phase cannot be measured directly by this method.

By exploiting the advantages of both optical and electromechanical methods, we can work out new methods for the evaluation of the piezoelectric transducer. Vibration theory is also considered in this evaluation. A disk piezoelectric transducer is used as a sample. The physical quantities, for example, values corresponding to the piezoelectric constant,[1)-3)] the acoustic velocity of the radial-extensional mode,[4)] and Poisson's ratio of the material [4)] can be evaluated using the new methods.

§3.2. Theory of Simple Harmonic Oscillation

3.2.1 Equation of Mechanical Vibration

In this section, the theory of simple harmonic oscillation of one dimension is described for our later use. We assume that the oscillator is composed of a material particle and a spring connecting the material particle. Infinitesimal vibration of the material particle near the stable equilibrium is treated as simple harmonic oscillation. The periodic external force whose angular frequency is ω_A [rad/s] acts on the material particle. The vibrational equation can be expressed as

$$m\frac{d^2u}{dt^2} + \eta'\frac{du}{dt} + ku = F\sin\omega_A t\,, \tag{3.2.1}$$

where u [m], m [kg], $-\eta' du/dt$ [N], $-ku$ [N], and F [N] are the displacement of the vibration, the mass of the material particle, the friction, the elastic force, and the amplitude of the external force, respectively. Equation (3.2.1) can be expressed as

$$\frac{d^2u}{dt^2} + 2\beta'\frac{du}{dt} + \omega_0^2 u = \rho'\sin\omega_A t\,, \tag{3.2.2}$$

where $\beta' = \eta'/(2m)$, $\omega_0^2 = k/m$, and $\rho' = F/m$, where ω_0 is the proper angular frequency of the vibrational system. The displacement u is calculated from eq.(3.2.2) as

$$u = A\sin(\omega_A t + \delta) + a' e^{\kappa t} + a'' e^{\lambda t}\,, \tag{3.2.3}$$

where

$$A = \rho'\{(\omega_0^2 - \omega_A^2)^2 + 4\beta^2\omega_A^2\}^{-1/2}\,, \tag{3.2.4}$$

$$\delta = -\tan^{-1}\{2\beta'\omega_A/(\omega_0^2 - \omega_A^2)\}\,, \tag{3.2.5}$$

$$\kappa = -\beta' - (\beta'^2 - \omega_0^2)^{1/2}\,, \tag{3.2.6}$$

$$\lambda = -\beta' + (\beta'^2 - \omega_0^2)^{1/2}\,, \tag{3.2.7}$$

a', a'' : constants.

The object of the measurement is the first term on the right hand in eq.(3.2.3); stationary state term. The Q-value is defined as

$$Q = \omega_0/(2\beta') \quad \text{[dimensionless]}, \tag{3.2.8}$$

If $Q > 2^{-1/2}$, the amplitude of the displacement A has the maximum as

$$A = 2\rho'(Q/\omega_0)^2/(4Q^2 - 1)^{-1/2}, \tag{3.2.9}$$

at an angular frequency $\omega_A = \omega_0\{1 - 1/(2Q^2)\}^{1/2}$.

The approximate relationship between the angular frequency of the external force ω_A and the vibrational response A and δ in eq.(3.2.3) is as follows:

a) When $\omega_A \to 0$,

$$A \equiv A_0 \approx \rho'/\omega_0^2 = F/k, \text{ and } \delta \approx 0, \tag{3.2.10}$$

where the stiffness controls the vibration. The displacement can follow the external force with $\delta \approx 0$; that is, the vibration is at a free state without clamping.

b) When $\omega_A \approx \omega_0$,

$$A \equiv A_{res} \simeq \rho' Q/\omega_0^2 = F/(\eta'\omega_0), \text{ and } \delta \simeq -\pi/2, \tag{3.2.11}$$

where the vibrational state becomes the resonance, and the resistance controls the vibration. The displacement at the resonance is Q times as large as that at $\omega_A \to 0$.

c) When $\omega_A >> \omega_0$,

$$A \simeq \rho'/\omega_A^2 = F/(m\omega_A)^2, \text{ and } \delta \simeq -\pi, \tag{3.2.12}$$

where the inertia controls the vibration, and $A \propto \omega_A^{-2}$. The displacement hardly follows the external force; that is, the vibration is clamped at the frequency much higher than the resonance.

The Q-value is calculated by the following method: Angular frequencies ω_{A1} and ω_{A2} are defined as

$$\text{when } \omega_A = \omega_{A1}, \quad \delta = \pi/4, \tag{3.2.13a}$$

$$\text{when } \omega_A = \omega_{A2}, \quad \delta = -\pi/4. \tag{3.2.13b}$$

Then, from eqs. (3.2.4) and (3.2.5),

$$\omega_{A2} - \omega_{A1} = 2\beta' = \omega_0 / Q, \tag{3.2.14}$$

and when $\omega_A = \omega_{A1}$ or $\omega_A = \omega_{A2}$,

$$A \simeq A_{res} / 2^{1/2}. \tag{3.2.15}$$

The Q-value can be calculated by the measurement of ω_{A1}, ω_{A2}, and ω_0, using eqs. (3.2.14) and (3.2.15).

3.2.2 Analogy between Electrical and Mechanical Vibration

The vibrational equation for the electrical resonance circuit can be expressed as

$$L\frac{di}{dt} + Ri + \frac{q}{C} = V \sin \omega_A t, \tag{3.2.16a}$$

where L [H], R [Ω], C [F], i [A], and V [V] are the inductance, resistance, capacitance, electric current, and electromotive force, respectively, and

$$q = \int i\, dt, \tag{3.2.16b}$$

is the electric charge. On the other hand, eq.(3.2.1) can be rewritten as

$$m\frac{dv}{dt} + \eta v + ku = F\sin\omega_A t\,, \tag{3.2.17a}$$

where v [m/s] is the velocity of the mechanical vibration, and

$$u = \int v\,dt\,. \tag{3.2.17b}$$

Comparison between eqs. (3.2.16a) and (3.2.17a) leads to the analogy between the electrical and the mechanical vibration as

electric charge q ↔ displacement u,

electric current i ↔ velocity v,

electromotive force V ↔ mechanical force F,

inductance L ↔ inertia (m),

resistance R ↔ friction (η),

capacitance C ↔ elasticity (k^{-1}), k : stiffness, k^{-1} : compliance.

The correspondence mentioned above is important for the discussion which will follow in this thesis.

§3.3. Treatment for Piezoelectric Vibration

3.3.1 Fundamental Piezoelectric Relations

Intensive variable, stress T [N/m^2], and extensive variable, strain S [dimensionless], are usually adopted as the variables of mechanical state, and they are second rank tensors. Stress T_{ij} in i-direction on j-plane is related to force F_i [N] in i-direction as

$$F_i = \partial T_{ij} / \partial x_j \cdot \Delta x_1 \Delta x_2 \Delta x_3, \tag{3.3.1}$$

where $\Delta x_1 \Delta x_2 \Delta x_3$ is the cubic content on which the force acts, and Einstein's summation convention is used; therefore, a summation from 1 to 3 is taken for the repeated indices in the same term. The engineering notations

$$T_1 \equiv T_{11}\,,\quad T_2 \equiv T_{22},\quad T_3 \equiv T_{33},$$
$$T_4 \equiv T_{23} = T_{32}\,,\quad T_5 \equiv T_{13} = T_{31}\,,\quad T_6 \equiv T_{12} = T_{21}\,,$$

are widely used. The strain S_{ij} is related to the displacement u as

$$S_{ij} = (\partial u_i/\partial x_j + \partial u_j/\partial x_i) / 2. \tag{3.3.2}$$

The engineering notations

$$S_1 \equiv S_{11}, \quad S_2 \equiv S_{22}, \quad S_3 \equiv S_{33},$$

$$S_4/2 \equiv S_{23} = S_{32}, \quad S_5/2 \equiv S_{13} = S_{31}, \quad S_6/2 \equiv S_{12} = S_{21},$$

are also widely used. The relation between S and T is expressed as

$$T_{ij} = c_{ijkl} S_{kl}, \text{ or } S_{ij} = s_{ijkl} T_{kl}, \tag{3.3.3}$$

where c [N/m^2] and s [m^2/N] are elastic stiffness and elastic compliance, respectively. They are fourth rank tensors.

Intensive variable, electric field E [V/m], and extensive variable, electric flux density D [C/m^2] are now adopted as the variables of electrical state, and they are first rank tensors. The relation between E and D is expressed as

$$D_i = \varepsilon_{ij} E_j, \text{ or } E_i = \beta_{ij} D_j, \tag{3.3.4}$$

where ε [F/m] and β [m/F] are the dielectric constant (permittivity) and the dielectric impermeability, respectively. They are second rank tensors.

Relations among the mechanical and the electrical variables are called the fundamental piezoelectric relations or the piezoelectric equations. There are four types of relations as

$$\begin{cases} S = s^E T + dE, \\ D = dT + \varepsilon^T E, \end{cases} \quad (d\text{-form}) \tag{3.3.5}$$

$$\begin{cases} T = c^E S - eE, \\ D = eS + \varepsilon^S E, \end{cases} \quad (e\text{-form}) \tag{3.3.6}$$

$$\begin{cases} S = s^D T + gD, \\ E = -gT + \beta^T D, \end{cases} \quad (g\text{-form}) \tag{3.3.7}$$

$$\begin{cases} T = c^D S - hD, \\ E = -hS + \beta^S D, \end{cases} \quad (h\text{-form}) \tag{3.3.8}$$

where d [m/V=C/N], e [N/(V·m)=C/m^2], g [m^2/C=V·m/N], and h [N/C=V/m] are the piezoelectric constants. They are third rank tensors; for example, $S_{ij} = d_{kij} E_k$ and $D_k = d_{kij} T_{ij}$. Superscripts "E" and "D" in the elastic constants indicate the electrical conditions $E = 0$, and $D = 0$, respectively, and superscripts "T" and "S" in the dielectric constants indicate the mechanical conditions $T = 0$, and $S = 0$, respectively. The electromechanical coupling coefficients k^2 [dimensionless] are generally defined by

$$c^E = (1 - k^2) c^D, \tag{3.3.9a}$$

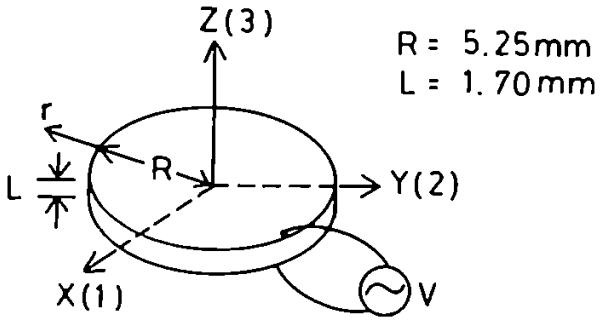

Fig. 3.1. Configuration of the disk piezoelectric transducer for the measurement.

Table 3.I. Elastic and dielectric tensors in crystallographic point group of *6mm*. The piezoelectric tensor was shown in Table 2.II.

Elastic

	1	2	3	4	5	6
1	•	•	•	·	·	·
2	•	•	•	·	·	·
3	•	•	•	·	·	·
4	·	·	·	•	·	·
5	·	·	·	·	•	·
6	·	·	·	·	·	×

The notation "×" means $(c_{11} - c_{12}) / 2$ or $2(s_{11} - s_{12})$, and $c_{ij} = c_{ji}$, $s_{ij} = s_{ji}$.

Dielectric

	1	2	3
1	•	·	·
2	·	•	·
3	·	·	•

Table 3.II. Main material constants of "P-7."

Piezoelectric	$d_{33}(10^{-12}m/V)$	410
	$d_{31}(10^{-12}m/V)$	-207
	$g_{33}(10^{-3}Vm/N)$	22
Permittivity	$\epsilon^{T}_{33}/\epsilon_0$	2100
Compliance	$s^{E}_{11}(10^{-12}m^2/N)$	15.8
Poisson's ratio	υ	0.31
Mass density	$\rho(10^{3}kg/m^{3})$	7.8

$$s^D = (1 - k^2) s^E, \tag{3.3.9b}$$

$$\epsilon^S = (1 - k^2) \epsilon^T, \tag{3.3.9c}$$

$$\beta^T = (1 - k^2) \beta^S. \tag{3.3.9d}$$

However, these definitions are conceptual. Exact definition of k^2 depends on the vibrational mode. The piezoelectric relations mentioned above are exactly defined for the situation of the low frequency limit $\omega_A \rightarrow 0$, because mechanical and electrical vibration cannot follow an external force at higher frequency. Therefore, the electromechanical coefficient is also defined for $\omega_A \rightarrow 0$.

3.3.2 Form of Sample

A sample for the measurement of piezoelectric vibration is in the form of a disk illustrated in Fig. 3.1. This is made of PZT material "P-7" (Murata Manufacturing Co., Ltd.), which is polarized in the direction of the thickness, that is, z-direction in Fig. 3.1. In this case, the crystallographic point group of the material is given as *6mm*. Its elastic, piezoelectric, and dielectric tensor forms are shown in Table 3.I. The main material constants are shown in Table 3.II. Silver electrodes are sintered on both faces of the sample.

3.3.3 Vibrational Modes and Their Mechanical Conditions

Such a disk piezoelectric transducer has radial-extensional and thickness-extensional resonances. The lowest resonance frequency of the thickness mode is much higher than the radial-extensional mode, because thickness L of the sample is sufficiently thin compared to radius R, and roughly speaking, the lowest resonance frequencies of the respective modes are inversely proportional to the sizes of the respective directions where the respective resonances can occur.

At the lowest resonance frequency of the radial-extensional mode, the displacement in the r-direction becomes the maximum, and the vibration in the z-direction is sufficiently free; that is, the stress T on the z-planes can be regarded as zero. The displacement in the z-direction also becomes the maximum as in the r-direction, because the displacement in the z-direction can follow that in the r-direction at this frequency.

On the other hand, at the lowest resonance frequency of the thickness-extensional mode, the vibration in the r-direction cannot follow the external force, and is clamped in the r-direction; that is, the strain S in the r-direction can be regarded as zero.

3.3.4 Piezoelectric Transverse and Longitudinal Effects

With regard to piezoelectric vibration, it is important to consider the direction of the wavenumber vector k of the vibration and that of the polarization P accompanied with the vibration. In general, when $k \perp P$, the vibration is in the piezoelectric *transverse* effect, and when $k \parallel P$, the vibration is in the piezoelectric *longitudinal* effect. The difference between the two effects leads to the difference of the electric conditions of the piezoelectric vibration. The electric condition has a great deal to do with the direction of the depolarizing field $E = -P / \varepsilon_0$.

In the radial-extensional mode, the wavenumber vector k is in the r-direction, the polarization P and the depolarizing field $E = -P / \varepsilon_0$ are in the z-direction. Therefore, this mode is caused by the transverse effect. In this case, the depolarizing field in the z-direction is completely short-circuited because of the existence of charges on the electrodes in the z-planes. This leads to the electric condition of E_3 being constant (or $E_3 = 0$) in the direction of the wavenumber vector k, the r-direction in this case. The electric flux density D_3 is not homogeneous in the direction of k, because the stress T_3 and the strain S_3 are not homogeneous in this direction.

On the other hand, in the thickness-extensional mode, k, P, and $E = -P / \varepsilon_0$ are in the z-direction. Therefore, this mode is caused by the longitudinal effect. In this case, the depolarizing field $E_3 = -P_3 / \varepsilon_0$ is not homogeneous in the direction of k, the z-direction in this case, because T_3 and S_3 are not homogeneous in this direction. On the other hand, D_3 is homogeneous in this direction. This leads to the electric condition of D_3 being constant (or $D_3 = 0$) in the direction of the wavenumber vector k, the z-direction in this case.

§3.4. Theory of Radial-Extensional Mode in Piezoelectric Transverse Effect

The vibration in the disk transducer can be analyzed using cylindrical coordinates. The theoretical analysis of the vibration of the radial-extensional mode is essential for the consideration of the new methods for evaluating the piezoelectric transducer described in this chapter. The radial-extensional mode is caused by the piezoelectric transverse effect.

The piezoelectric equations are given by the d-form as

$$S_r = s^E_{11} T_r + s^E_{12} T_\theta + s^E_{13} T_z + d_{31} E_z , \tag{3.4.1a}$$

$$S_\theta = s^E_{12} T_r + s^E_{11} T_\theta + s^E_{13} T_z + d_{31} E_z , \tag{3.4.1b}$$

$$S_z = s^E_{13} T_r + s^E_{13} T_\theta + s^E_{33} T_z + d_{33} E_z , \tag{3.4.1c}$$

$$D_z = d_{31} T_r + d_{31} T_\theta + d_{33} T_z + \varepsilon^T_{33} E_z , \tag{3.4.2}$$

and the Newton's equation of motion is given by

$$\rho \frac{\partial^2 u_r}{\partial t^2} = \frac{\partial T_{rr}}{\partial r} + \frac{T_{rr} - T_{\theta\theta}}{r}, \tag{3.4.3}$$

where

$$S_{rr} = \frac{\partial u_r}{\partial r},\ S_{\theta\theta} = \frac{u_r}{r},\ \text{and}\ S_{zz}\ (=S_3) = \frac{\partial u_z}{\partial z}. \tag{3.4.4}$$

are the strain, u_r is the displacement in the r–direction, T_{mn} is the stress in the m–direction on the n–plane, E_z $(=E_3)$ is the electric field in the z–direction, D_z $(=D_3)$ is the electric flux density in the z–direction, s^E_{ij} is the elastic compliance when E = 0, d_{kl} is the piezoelectric d–constant, and ρ [kg/m^3] is the mass density of the material. Notations that

$$s_{11} \equiv s_{1111},\ s_{12} \equiv s_{1122},\ s_{13} \equiv s_{1133},$$
$$d_{31} \equiv d_{311},\ d_{33} \equiv d_{333},$$

are used here. The mechanical condition is given by

$$T_{zz}\ (=T_3) = 0, \tag{3.4.5}$$

and the electrical condition is given by

$$\frac{\partial E_z}{\partial r} = 0. \tag{3.4.6}$$

The grounds of eqs. (3.4.5) and (3.4.6) were described in §3.3.3 and §3.3.4, respectively. From eqs. (3.4.1a) and (3.4.1b) using the mechanical condition eq.(3.4.5), T_{rr} and $T_{\theta\theta}$ are expressed as

$$T_{rr} = c'S_{rr} + c'\sigma S_{\theta\theta} - e'E_z, \tag{3.4.7a}$$

$$T_{\theta\theta} = c'\sigma S_{rr} + c'S_{\theta\theta} - e'E_z, \tag{3.4.7b}$$

where

$$c' = \{\ s^E_{11}\ (1 - \sigma^2)\ \}^{-1}, \tag{3.4.8a}$$

$$\sigma = -\ s^E_{12} / s^E_{11}, \tag{3.4.8b}$$

$$e' = d_{31} / \{\ s^E_{11}\ (1 - \sigma)\ \}, \tag{3.4.8c}$$

where σ [dimensionless] is the Poisson's ratio of the material.

Substitution of eqs. (3.4.7a) and (3.4.7b) into eq.(3.4.3) using the electrical condition eq.(3.4.6) gives

Table 3.III. The value of α_n for the Poisson's ratio σ.

σ	α_1	α_2/α_1	σ	α_1	α_2/α_1
0.25	2.017	2.667	0.33	2.067	2.610
0.26	2.024	2.660	0.34	2.074	2.603
0.27	2.030	2.652	0.35	2.080	2.596
0.28	2.036	2.645	0.36	2.086	2.590
0.29	2.043	2.638	0.37	2.092	2.583
0.30	2.049	2.630	0.38	2.097	2.577
0.31	2.055	2.623	0.39	2.103	2.571
0.32	2.061	2.617	0.40	2.107	2.564

$$-\frac{\omega_A^2\rho}{c'}u(r)=\frac{\partial^2 u(r)}{\partial r^2}+\frac{1}{r}\frac{\partial u(r)}{\partial r}-\frac{u(r)}{r^2}, \tag{3.4.9}$$

where

$$u_r = u(r)\exp(-j\omega_A t), \tag{3.4.10}$$

is assumed. Equation (3.4.9) is the Bessel's equation; therefore, $u(r)$ can be expressed as

$$u(r) = B' J_1(\omega_A r / v), \tag{3.4.11}$$

where B' [m] is a coefficient, $J_i(x)$ is the Bessel function of the first kind of order i, and v [m/s] is the acoustic velocity of the radial-extensional mode,

$$v = (c'/\rho)^{1/2} = \{\rho s^E_{11}(1-\sigma^2)\}^{-1/2}. \tag{3.4.12}$$

The Bessel function of the second kind, the Neumann function $Y_i(x)$, is not appropriate for the expression of $u(r)$, because when $r \to 0$, $Y_i(\omega_A r / v) \to -\infty$.

The coefficient B' can be determined by the mechanical boundary condition,

$$T_r = 0 \quad \text{at } r = R, \tag{3.4.13}$$

where R [m] is the radius of the disk sample. By using eqs. (3.4.4), (3.4.7a), (3.4.11), (3.4.13), and the relationship on the Bessel function,

$$xdJ_i(x)/dx + iJ_i(x) = xJ_{i-1}(x), \tag{3.4.14}$$

the coefficient B' is calculated as

$$B' = \frac{d_{31}(1+\sigma)E_z R}{\alpha J_0(\alpha)-(1-\sigma)J_1(\alpha)}, \tag{3.4.15}$$

where α [dimensionless] is expressed as

$$\alpha = \omega_A R / v. \tag{3.4.16a}$$

The pole of the coefficient B' determines the frequencies of the mechanical resonance which is a characteristic of the entire sample. That is, the mechanical resonance angular frequencies,

$$\omega_{An} = \alpha_n v/R \ (n = 1,2,3,\cdots), \tag{3.4.16b}$$

can be obtained by

$$\alpha_n J_0(\alpha_n) - (1-\sigma)J_1(\alpha_n) = 0. \tag{3.4.17}$$

The value of α_n for the Poisson's ratio σ is shown in Table 3.III.[5]

The electric flux density D_z is expressed by using eqs.(3.4.2), (3.4.7a), and (3.4.7b) as

$$D_z = \varepsilon^{PS}_{33} E_z + e' (S_{rr} + S_{\theta\theta}), \tag{3.4.18}$$

where

$$\varepsilon^{PS}_{33} = \varepsilon^{T}_{33} (1 - k_p^2), \tag{3.4.19}$$

with

$$k_p^2 = \frac{2}{1-\sigma} \frac{d_{31}^2}{s^E_{11} \varepsilon^T_{33}}. \tag{3.4.20}$$

The superscript "PS" in eq.(3.4.19) indicates that $S_{rr} = S_{\theta\theta} = 0$, clamped in the plane. Equations (3.4.19) and (3.4.20) are the definition of the electromechanical coefficient k_p^2 in the radial-extensional mode. The electric current I [A] is calculated using

$$I = j\omega_A \int_0^R D_z \, 2\pi r \, dr , \tag{3.4.21a}$$

and the electric voltage V [V] is given by

$$V = E_z L, \tag{3.4.21b}$$

where L [m] is the thickness of the disk sample. The admittance Y [S] = I / V can be calculated by using eqs. (3.4.21a) and (3.4.21b) with eqs. (3.4.18), (3.4.4), (3.4.11), and (3.4.15) as

$$Y = Y_0 + Y_P, \tag{3.4.22a}$$

where

$$Y_0 = j\omega_A C_0 , \tag{3.4.22b}$$

$$Y_P = j\omega_A C_0 \frac{k_p^2}{1 - k_p^2} \frac{1 + \sigma}{\alpha J_0(\alpha) / J_1(\alpha) - (1-\sigma)}, \tag{3.4.22c}$$

where

$$C_0 = \varepsilon^{PS}_{33} \pi R^2 / L , \tag{3.4.22d}$$

which is the capacitance when $S_{rr} = S_{\theta\theta} = 0$, measured at the low frequency limit $\omega_A \to 0$. When eq.(3.4.17) is satisfied, the piezoelectric admittance Y_P in eq.(3.4.22c) becomes the maximum; that is, electrical resonance occurs.

The piezoelectric admittance Y_P can be expanded with respect to the $\pm\alpha_n$, the pole of eq.(3.4.22c), as [5]

$$Y_P = \sum_{n=1} \frac{1}{j\{\omega_A L_n - 1/(\omega_A C_n)\}}, \tag{3.4.23a}$$

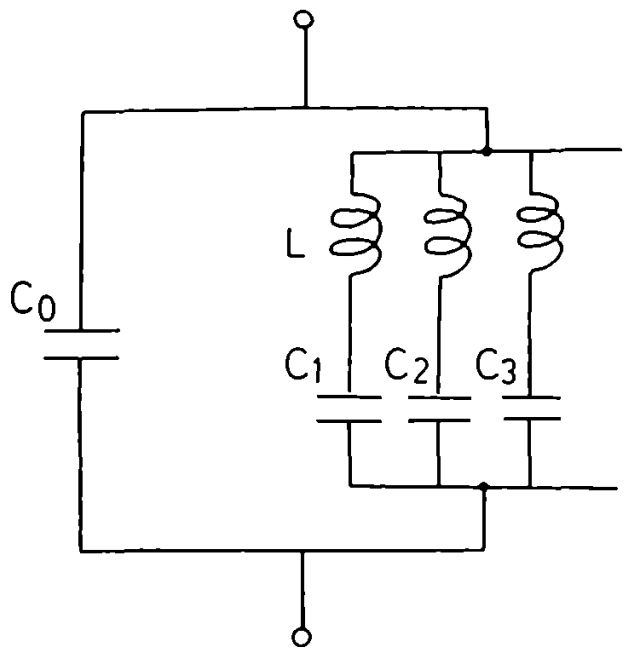

Fig. 3.2. Equivalent circuit for the radial-extensional mode in the piezoelectric *transverse* effect.

where

$$C_n = p_n \frac{k_p^2}{1 - k_p^2} C_0 , \tag{3.4.23b}$$

$$L_n = (\omega_{A1}^2 C_1)^{-1}, \tag{3.4.23c}$$

with

$$p_n = \frac{2(1+\sigma)}{\alpha_n^2 - (1-\sigma^2)} \quad (n = 1,2,3,\cdots), \tag{3.4.23d}$$

$$\sum_{n=1} p_n = 1. \tag{3.4.23e}$$

Therefore, the equivalent circuit for the radial-extensional mode in the piezoelectric transverse effect can be expressed as illustrated in Fig. 3.2. The capacitance C_n (n = 1,2,3,$\cdots$) corresponds to the elasticity of the n-th resonance of the mode, and inductance L_n corresponds to its inertia.

§3.5. Theory of Thickness-Extensional Mode in Piezoelectric Longitudinal Effect

The thickness-extensional mode is caused by the piezoelectric longitudinal effect. The piezoelectric equations are given by the e-form as

$$T_z = c^E_{13} S_r + c^E_{13} S_\theta + c^E_{33} S_z - e_{33} E_z , \tag{3.5.1}$$

$$D_z = e_{31} S_r + e_{31} S_\theta + e_{33} S_z + \varepsilon^S_{33} E_z , \tag{3.5.2}$$

and the Newton's equation of motion is given by

$$\rho \frac{\partial^2 u_z}{\partial t^2} = \frac{\partial T_z}{\partial z} , \tag{3.5.3}$$

where c^E_{ij} is the elastic stiffness when E = 0, and e_{kl} is the piezoelectric e-constant. The mechanical and the electrical conditions are given by

$$S_r = S_\theta = 0 . \tag{3.5.4}$$

$$\frac{\partial D_z}{\partial z} = 0 . \tag{3.5.5}$$

The grounds of eqs. (3.5.4) and (3.5.5) were described in §3.3.3 and §3.3.4, respectively. From eqs. (3.5.1) and (3.5.2) with the mechanical condition eq.(3.5.4), T_z can be expressed in a form without E_z as

$$T_{zz} = c^{D}_{33} S_{zz} - (e_{33}/\varepsilon^{S}_{33}) D_z , \tag{3.5.6}$$

where

$$c^{D}_{33} = c^{E}_{33} (1 - k_t^2)^{-1}, \tag{3.5.7}$$

with

$$k_t^2 = e_{33}^2/(c^{D}_{33}\varepsilon^{S}_{33}) , \tag{3.5.8}$$

where c^{D} is the elastic stiffness when $D = 0$. The translation from eq.(3.5.1) to eq.(3.5.6) is necessary for the analysis of the vibration, because E_z is not constant in the z-direction. Equations (3.5.7) and (3.5.8) define the electromechanical coefficient in the thickness-extensional mode.

Substitution of eq.(3.5.6) into eq.(3.5.3) using the electrical condition eq.(3.5.5) gives

$$\rho \frac{\partial^2 u_z}{\partial t^2} = c^{D}_{33} \frac{\partial^2 u_{zz}}{\partial z^2} . \tag{3.5.9}$$

The expression for u_z is assumed as

$$u_z = u(z) \exp(-j\omega_A t), \tag{3.5.10a}$$

with

$$u(z) = B' \sin(\omega_A z/v) + C' \cos(\omega_A z/v), \tag{3.5.10b}$$

where

$$v = (c^{D}_{33}/\rho)^{1/2} , \tag{3.5.11}$$

is the acoustic velocity of the thickness-extensional mode. Coefficients B' and C' can be determined by the mechanical boundary condition,

$$T_{zz} = 0 \quad \text{at} \quad z = \pm L/2. \tag{3.5.12}$$

Since the electric flux density D_z is constant in the z-direction, eqs. (3.5.6) and (3.5.12) with eqs. (3.4.4) and (3.5.10b) yield to

$$B' = \frac{e_{33} D_z}{c^{D}_{33}\varepsilon^{S}_{33}(\omega_A/v) \cos\{ \omega_A L/ (2v) \}} , \tag{3.5.13a}$$

$$C' = 0 . \tag{3.5.13b}$$

The electric current I is assumed to be calculated by

$$I = j\omega_A \int_0^R D_z \, 2\pi r \, dr = j\omega_A D_z \, \pi R^2, \tag{3.5.14a}$$

and the electric voltage V is given by

$$V = \int_{-L/2}^{L/2} E_z \, dz \, . \tag{3.5.14b}$$

For the calculation of the admittance $Y = I / V$, eq.(3.5.2) is integrated with respect to z from $-L/2$ to $L/2$, and we obtain

$$D_z L = \varepsilon^S{}_{33} V + \frac{e_{33}{}^2 D_z \cdot \sin\{ \omega_A L/(2v) \}}{c^D{}_{33} \varepsilon^S{}_{33} \{ \omega_A/(2v) \} \cos\{ \omega_A L/(2v) \}} . \tag{3.5.15a}$$

Integrating eq.(3.5.15a) with respect to r yields

$$j\omega_A D_z \pi R^2 \{ 1 - k_t{}^2 (\tan b)/b \} = j\omega_A \varepsilon^S{}_{33} \pi R^2 V / L, \tag{3.5.15b}$$

where

$$b = \omega_A L / (2v) . \tag{3.5.15c}$$

Therefore, the admittance Y can be expressed as

$$Y = j\omega_A \frac{\varepsilon^S{}_{33}}{1 - k_t{}^2 (\tan b)/b} \frac{\pi R^2}{L} . \tag{3.5.16}$$

When

$$b = b_m \equiv \omega_{Am} L / (2v) = m\pi / 2 \quad (m = 1,3,5,\cdots), \tag{3.5.17}$$

the mechanical resonance occurs in consideration of eqs. (3.5.10b), (3.5.13a) and (3.5.13b). Then, the admittance becomes zero; that is, electrical antiresonance occurs.

Equation (3.5.16) can be rewritten as

$$Y = Y_0 + Y_P, \tag{3.5.18a}$$

where

$$Y_0 = j\omega_A C_0 , \tag{3.5.18b}$$

$$Y_P{}^{-1} \equiv Z_P = \frac{1}{j\omega_A(-C_0)} + \frac{1}{j\omega_A C_0 k_t{}^2 (\tan b)/b} , \tag{3.5.18c}$$

where

$$C_0 = \varepsilon^S{}_{33} \pi R^2 / L, \tag{3.5.18d}$$

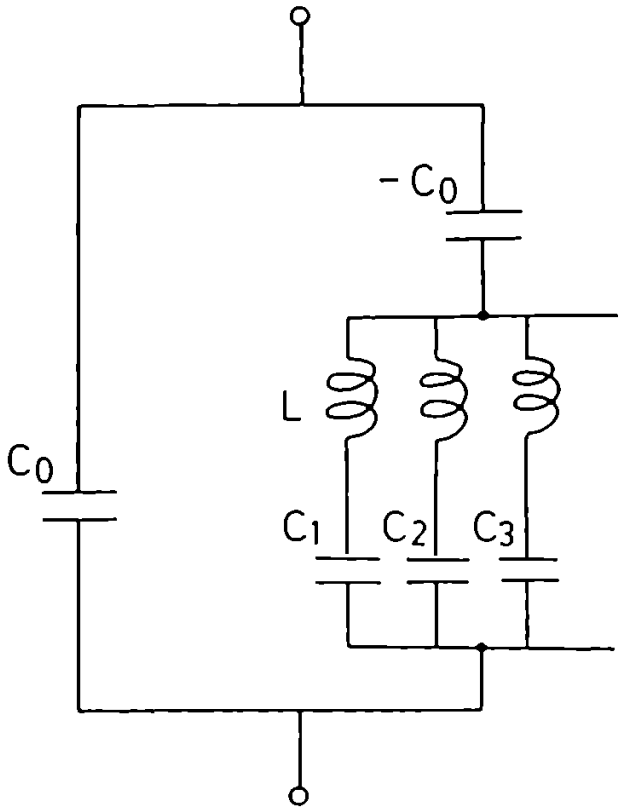

Fig. 3.3. Equivalent circuit for the thickness-extensional mode in the piezoelectric *longitudinal* effect.

which is the capacitance measured at the low frequency limit $\omega_A \to 0$ in the clamped state in not only the r–, and θ–directions but also z–direction. The second term in eq.(3.5.18c) can be expanded with respect to the pole of (tan b)/b; therefore, we can obtain the expression as [5]

$$Y_P^{-1} \equiv Z_P = \frac{1}{j\omega_A(-C_0)} + \sum_{m=1} j\{ \omega_A L_m - 1/(\omega_A C_m) \}, \tag{3.5.19a}$$

where

$$C_m = p_m k_t^2 C_0 \quad , \tag{3.5.19b}$$

$$L_m = (\omega_{A1}^2 C_1)^{-1} \quad , \tag{3.5.19c}$$

with

$$p_m = 8 / (\pi^2 m^2) \quad \text{for} \quad m = 1,3,5,\cdots, \text{ and } p_m = 0 \quad \text{for} \quad m = 2,4,6,\cdots, \tag{3.5.19d}$$

$$\sum_{m=1} p_m = 1. \tag{3.5.19e}$$

Therefore, the equivalent circuit for the thickness–extensional mode in the piezoelectric longitudinal effect can be expressed as illustrated in Fig. 3.3.

We summarize the difference between the piezoelectric transverse and the longitudinal effects. In the transverse effect, the mechanical resonance corresponds to the electrical resonance. On the other hand, in the longitudinal effect, the mechanical resonance corresponds to the electrical antiresonance. Therefore, in the electrical equivalent circuits, the negative capacitance $-C_0$ exists in series with the impedance which corresponds to the piezoelectric vibration in the longitudinal effect. This difference is caused by the difference of the electrical condition. In the transverse effect, the electrical condition is that E is constant. Even if $E = 0$, which is the ideal situation at the electrical resonance, the vibration can occur. Therefore, the electric voltage V corresponds to the external force, and the mechanical resonance can occur at the electrical resonance. In the longitudinal effect, the electrical condition is that D is constant. Even if $D = 0$, which is the ideal situation at the electrical antiresonance, the vibration can occur. Therefore, the electric current I corresponds to the external force, and the mechanical resonance can occur at the electrical antiresonance.

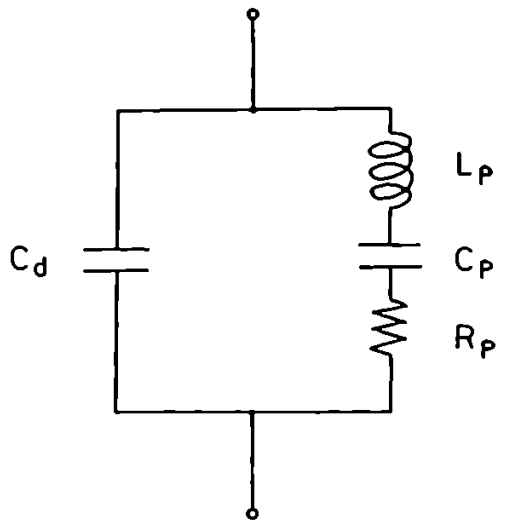

Fig. 3.4. Equivalent circuit of the piezoelectric transducer near the present resonance. This expression is appropriate for both the piezo-electric transverse and the longitudinal effects.

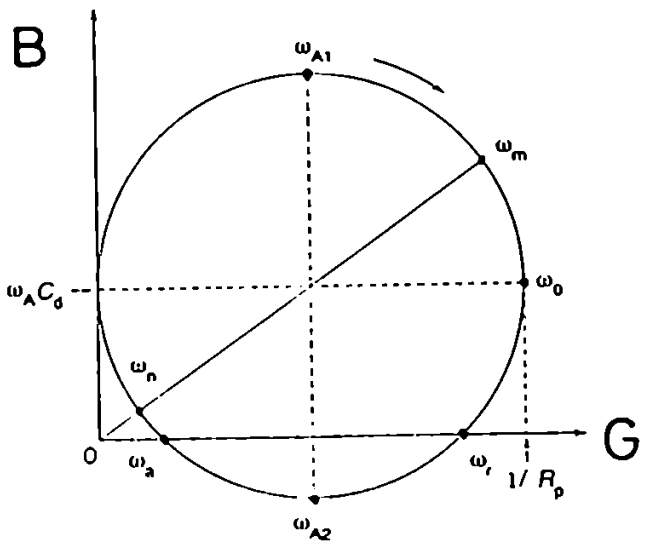

Fig. 3.5 Frequency characteristic of $Y = Y_d + Y_{mot}$, the locus of the admittance. The abscissa and the ordinate are the conductance G [S] and the susceptance B [S], respectively. The locus rotates clockwise when the frequency increases.

§3.6. Electromechanical Measurement of Piezoelectric Vibration

3.6.1 Admittance near Resonance Frequency

The admittance of the piezoelectric transducer near the resonance frequency can be expressed as

$$Y = Y_d + Y_{mot}, \tag{3.6.1a}$$

where

$$Y_d = j\omega_A C_d, \tag{3.6.1b}$$

$$Y_{mot} = [\, R_p + j\,\{\omega_A L_p - 1/(\omega_A C_p)\}\,]^{-1}. \tag{3.6.1c}$$

This expression is appropriate for both the piezoelectric transverse and longitudinal effects. The motional admittance Y_{mot} in eq.(3.6.1c) is not equal to the admittance Y_p in eqs. (3.4.22c) and (3.5.19a), and the dumped capacitance C_d in eq.(3.6.1b) is not equal to the capacitance C_0 in eqs. (3.4.22d) and (3.5.18d), because Y_{mot} deals with only one resonance under consideration. On the other hand, Y_p is the total piezoelectric admittance, involving harmonic resonances. Therefore, the dumped capacitance C_d includes not only C_0 but also the other elements in Y_p, which are not included in Y_{mot}.

The equivalent circuit of the piezoelectric transducer near the present resonance is shown in Fig. 3.4. The frequency characteristic of $Y = Y_d + Y_{mot}$ is illustrated in Fig. 3.5. Figure 3.5 shows the locus of the admittance, and the abscissa and the ordinate are the conductance G [S] and the susceptance B [S], respectively. The locus rotates clockwise when the frequency increases. The angular frequencies ω_m, ω_n, ω_r, ω_a, ω_0, ω_{A1}, and ω_{A2} are defined as

$\omega_A = \omega_m$, when $|\,Y\,|$ becomes the maximum,

$\omega_A = \omega_n$, when $|\,Y\,|$ becomes the minimum,

$\omega_A = \omega_r$ (resonance),
$\omega_A = \omega_a$ (antiresonance), } when the susceptance $B = 0$, where $\omega_r < \omega_a$

$\omega_A = \omega_0$, when the conductance G becomes the maximum,

$\omega_A = \omega_{A1}$, when the phase angle of Y_{mot} is $\pi/4$,

$\omega_A = \omega_{A2}$, when the phase angle of Y_{mot} is $-\pi/4$.

The mechanical Q-value can be calculated by

$$Q^{-1} = (\,\omega_{A2} - \omega_{A1}\,) / \omega_0 = \omega_0 C_p R_p, \tag{3.6.2}$$

using the electromechanical measurement of the piezoelectric transducer.

3.6.2 Measurement of Electromechanical Coupling Coefficient

The electromechanical coupling coefficient k^2 can be determined by the measurement of ω_r and ω_a. The methods of determining of k^2 are described below. The electromechanical coupling coefficient k^2 depends on the vibrational mode, and we can express k^2 exactly as

$$C_0 = \sum_{n=0} C_n (1 - k^2) , \tag{3.6.3}$$

where C_n (n = 0,1,2,3,···) is illustrated in Figs. 3.2 and 3.3 and depends on the vibrational mode. The capacitance C_0 is in proportion to the dielectric constant measured at the low frequency limit $\omega_A \rightarrow 0$ in the clamped state defined in the respective modes. The summation of C_n from n = 1 to ∞ corresponds to the elasticity of the transducer at the low frequency limit $\omega_A \rightarrow 0$, because all modes of vibration can follow the external force completely at $\omega_A \rightarrow 0$, and the mechanical vibration is controlled completely by stiffness. The expression of k^2 in eq.(3.6.3) involves the specific definition of k^2 of the respective modes mentioned previously.

The relationship among k^2, ω_r, and ω_a is as follows.

In the piezoelectric transverse effect, the electric equivalent circuit can be expressed in Fig. 3.2. With regard to the purpose of calculating k^2, the admittance $Y = Y_0 + Y_P$ is assumed to be expressed as

$$Y = Y_0 + Y_P = j\omega_A C_0 [1 + \{ k^2 / (1 - k^2) \} \cdot \tan b(\omega_A) / b(\omega_A)], \tag{3.6.4a}$$

where $b(\omega_A)$ is the function of ω_A and is in proportion to ω_A. At the resonance angular frequency $\omega_A = \omega_r$, mechanical resonance occurs and Y reaches its peak; therefore,

$$b(\omega_r) = \pi / 2 . \tag{3.6.4b}$$

At the antiresonance angular frequency $\omega_A = \omega_a$, Y approaches its minimum; therefore,

$$1 + \{ k^2 / (1 - k^2) \} \cdot \tan b(\omega_a) / b(\omega_a) = 0 . \tag{3.6.4c}$$

At the low frequency limit $\omega_A \rightarrow 0$, b approaches zero, and

$$Y / (j\omega_A) \rightarrow C_0 / (1 - k^2) . \tag{3.6.4d}$$

Equation (3.6.4a) is based on the electric equivalent circuit of the transverse effect, and eqs. (3.6.4b) and (3.6.4c) satisfy the definition of electrical resonance and antiresonance, respectively, and eq.(3.6.4d) is consistent with the expression of k^2 given by eq.(3.6.3). Therefore, eqs. (3.6.4a) to (3.6.4c) are reasonable for the purpose of calculating k^2 in the transverse effect. From eqs.(3.6.4b) and (3.6.4c),

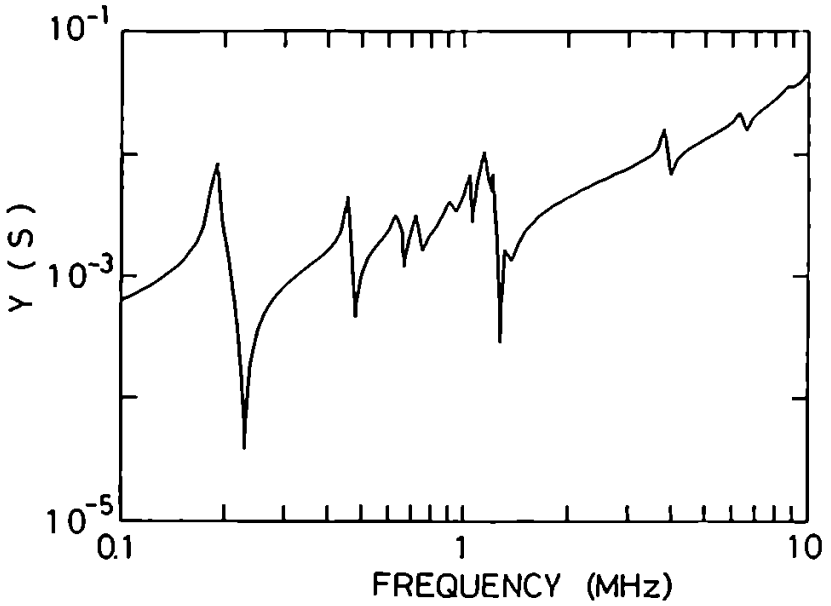

Fig. 3.6. Frequency characteristic of the admittance $|Y|$ of the disk sample illustrated in Fig. 3.1.

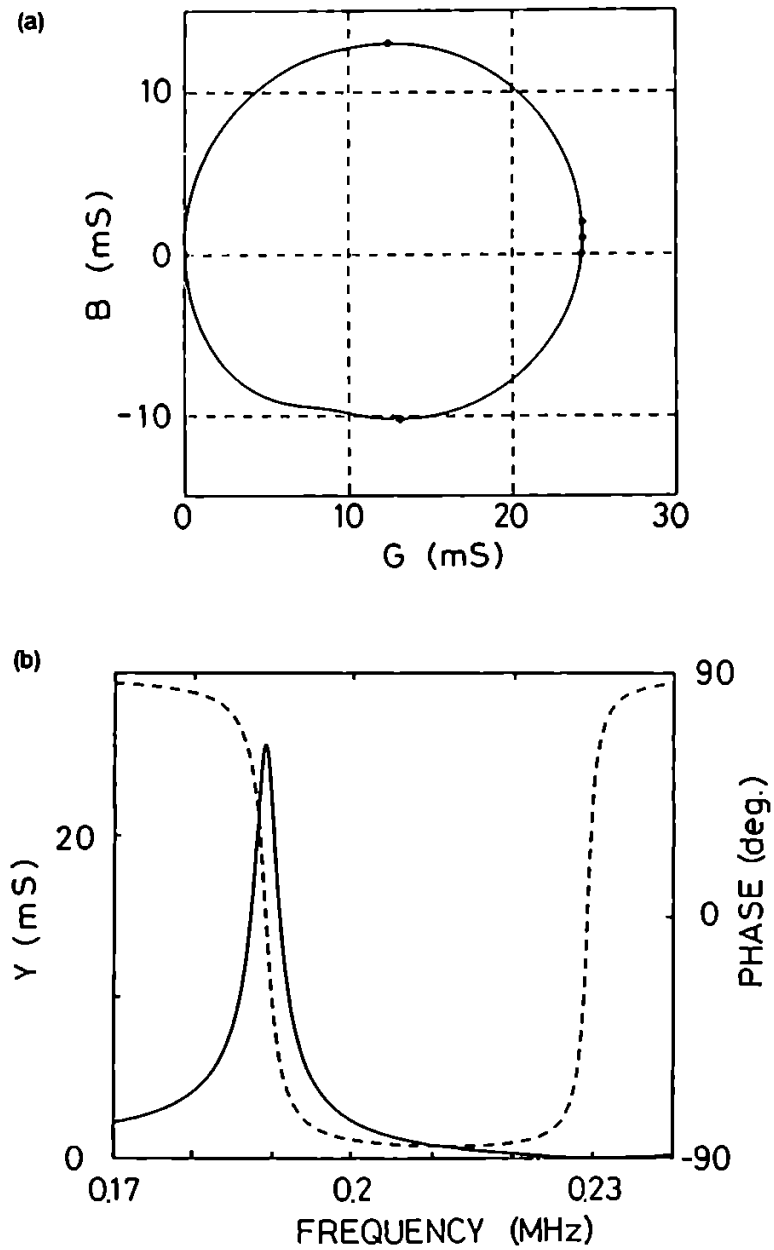

Fig. 3.7. Frequency characteristics of the admittance near the *first* resonance of the radial-extensional mode. (a) The *G-B* characteristic. (b) The solid line and the dashed line show the frequency characteristics of $|Y|$ and the phase angle of Y, that is, the phase difference between the electric current I and the voltage V, respectively.

$$\frac{k^2}{1-k^2} = -\frac{(\pi/2)(\omega_a/\omega_r)}{\tan\{(\pi/2)(\omega_a/\omega_r)\}}, \tag{3.6.5}$$

can be obtained, because $b(\omega_\Lambda)$ is in proportion to ω_Λ. Equation (3.6.5) is used for the calculation of k^2 in the electromechanical measurement of piezoelectric vibration in the transverse effect.

With regard to the piezoelectric longitudinal effect, a similar assumption is reasonable for the expression of $Y = Y_0 + Y_P$ as

$$Y = Y_0 + Y_P = j\omega_\Lambda C_0 \{1 - k^2 \tan b(\omega_\Lambda)/b(\omega_\Lambda)\}^{-1}, \tag{3.6.6a}$$

which is based on the electric equivalent circuit illustrated in Fig. 3.3. At the resonance angular frequency $\omega_\Lambda = \omega_r$, Y approaches its peak; therefore,

$$1 - k^2 \tan b(\omega_r)/b(\omega_r) = 0. \tag{3.6.6b}$$

At the antiresonance angular frequency $\omega_\Lambda = \omega_a$, Y approaches its minimum; therefore,

$$b(\omega_a) = \pi/2. \tag{3.6.6c}$$

At the low frequency limit $\omega_\Lambda \to 0$, b approaches zero, and

$$Y/(j\omega_\Lambda) \to C_0/(1-k^2), \tag{3.6.6d}$$

which is consistent with eq.(3.6.3). From eqs. (3.6.6b) and (3.6.6c),

$$k^2 = \frac{(\pi/2)(\omega_r/\omega_a)}{\tan\{(\pi/2)(\omega_r/\omega_a)\}}, \tag{3.6.7}$$

can be obtained. Equation (3.6.7) is used for the calculation of k^2 in the electromechanical measurement of piezoelectric vibration in the longitudinal effect.

3.6.3 Electromechanical Measurement of Disk Sample

A frequency characteristic of the admittance $|Y|$ of the disk sample described in §3.3.2 is shown in Fig. 3.6. Impedance analyzer (HP4192A) was used for the measurement. The peaks of Y below 1 MHz are caused by the radial-extensional resonances whose frequencies are determined by eq.(3.4.16b), and the antiresonances of Y over 1 MHz are mainly caused by the thickness-extensional resonances whose frequencies are determined by eq.(3.5.17).

Figures 3.7(a) and 3.7(b) shows the frequency characteristics of the admittance near the first resonance of the radial-extensional mode. Figure 3.7 (a) shows the admittance locus, that is, G-B characteristic, and the solid line and the dashed line in Fig. 3.7 (b) show the frequency characteristics of $|Y|$ and the phase angle of Y, that is, the phase difference between the electric

Table 3.IV. Typical results of the measurement of ω_{A1}, ω_m, ω_0, ω_r, ω_{A2}, ω_a, and ω_n near the *first* resonance of the radial-extensional mode.

$\omega_{A1}/(2\pi)$	0.1864 MHz	$\omega_{A2}/(2\pi)$	0.1888 MHz
$\omega_m/(2\pi)$	0.1875 MHz	$\omega_a/(2\pi)$	0.2285 MHz
$\omega_0/(2\pi)$	0.18755 MHz	$\omega_n/(2\pi)$	0.2285 MHz
$\omega_r/(2\pi)$	0.1876 MHz		

Table 3.V. The Q-value, k_p^2 and the parameters of the equivalent circuit represented in Fig. 3.4, C_d, C_p, R_p, and L_p, calculated by the data in Table 3.IV.

Q	78.1	C_d	537 pF
k_p^2	0.37	C_p	264 pF
		R_p	41.2 Ω
		L_p	2.73 mH

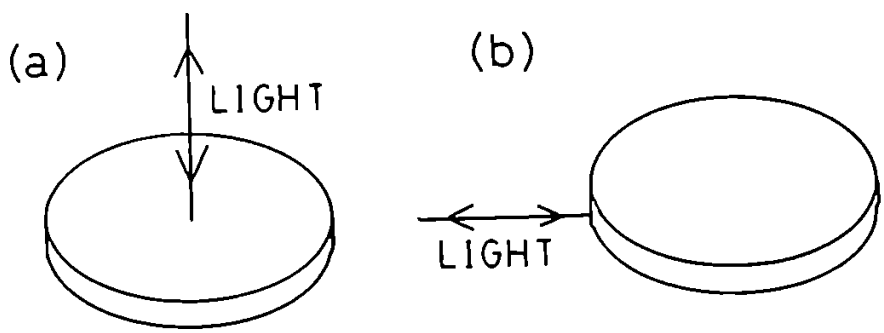

Fig. 3.8. Light for the measurement is incident on the sample surface. Diagram (a) shows the incidence of the light on the sample in the z-direction. Diagram (b) shows the incidence at the edge of the sample in the r-direction.

current and the voltage, respectively. The results of the measurement of ω_{A1}, ω_m, ω_0, ω_r, ω_{A2}, ω_a, and ω_n defined in §3.6.1 are shown in Table 3.IV. The Q-value is calculated as 78 by using eq.(3.6.2), and the electromechanical coupling coefficient k_p^2 is calculated as 0.37 by using eq.(3.6.5). Table 3.V shows the parameters of the equivalent circuit represented in Fig. 3.4, C_d, C_p, R_p, L_p, as well as Q and k_p^2. We must pay attention to the variation of Q-value due to certain experimental conditions, e.g. the method of fixing the sample. The values of k^2 and ω_r of different samples of the same shape and made of the same material are not always the same.

In Fig. 3.7 (b), the phase angle of Y decreases from $+\pi$ to $-\pi$ at the resonance , and increases from $-\pi$ to $+\pi$ again at the antiresonance. The former phase shift is caused by mechanical resonance, where the phase difference δ between the displacement u and the external force F changes, as expressed in eqs. (3.2.10) to (3.2.12). The correspondence between mechanical and electrical vibration exists, as described in §3.2.2. The latter phase shift is caused by the influence of the dumped capacitance which exists intrinsically in the piezoelectric transducer.

§3.7. Evaluation of Piezoelectric Vibration by Optical Measurement of Acoustic Amplitude

The optical method described in §2.4 enables us to measure the amplitude and the phase of the acoustic vibration. This section described the evaluation of the piezoelectric disk transducer by optically measuring acoustic *amplitude*. The optical measurement of the acoustic *phase* measured optically will be described in §3.8. The experimental configuration was described in §2.4.2, as illustrated in Figs. 2.13 and 2.14. The method of calculating the amplitude U_A was described in §2.4.3.

The light for the measurement is incident on the sample surface, as illustrated in Fig.3.8. Diagram (a) in Fig.3.8 shows the incidence of the light on the sample in the z-direction. Changing the measurement point on the z-plane enables us to evaluate the amplitude in the z-direction, $U_{Az}(r)$, at the position r locally. Diagram (b) in Fig.3.8 shows the incidence at the edge of the sample in the r-direction, and the amplitude in the r-direction, $U_{Ar}(r)$, at the position $r = R$ can be evaluated. The strains S_1 and S_3 can be calculated from the amplitude as

$$S_1 = U_{Ar}(R) / R , \tag{3.7.1}$$

$$S_3 = U_{Az}(r) / (L/2) . \tag{3.7.2}$$

3.7.1 Evaluation of Piezoelectric "d' " Value [1), 2)]

In this section, we describe the optical measurement of the vibration of the radial-extensional mode. This mode is caused by the piezoelectric transverse effect, as described in §3.3.4. The

electrical condition in which the electric field E is constant can be adopted. For example, the acoustic velocity is determined by the elastic compliance s^E, where $E = 0$ is conditioned, and the equation of the d-form expressed in eq.(3.3.5) is adopted for fundamental piezoelectric relations. Therefore, we deal with the value S / E as the fundamental value of optical measurement. We measure the frequency characteristics of S / E near the first resonance frequency of the radial-extensional mode.

The fundamental piezoelectric relations and the electromechanical coupling coefficient are defined at the low frequency limit $\omega_A \to 0$, as described in §3.3.1 and §3.6.2. Therefore, we consider the low frequency limit of S / E below. From eqs. (3.4.4), (3.4.10), (3.4.11) and (3.4.15), we can obtain [2)]

$$S_{00} / E_z \to d_{31} \quad (\omega_A \to 0), \tag{3.7.3}$$

$$S_{rr} / E_z \to d_{31} \quad (\omega_A \to 0), \tag{3.7.4}$$

$$\frac{S_{zz}}{E_z} = \frac{s^E_{13} / s^E_{11} \cdot (S_{rr} / E_z + S_{\theta\theta} / E_z - 2d_{31})}{1 - \sigma} + d_{33} \to d_{33} \quad (\omega_A \to 0), \tag{3.7.5}$$

where the characteristics of the Bessel functions, when $x \to 0$, $J_0(x) \to 1$, and $J_1(x) \to x/2$, are used. In that way, we can measure the piezoelectric d-constants by measurement of S / E at the low frequency limit. But, measurement near dc frequency is generally difficult because of the influence of noise in experimental circumstances. In addition, using optical measurement, the sensitivity of the measurement becomes lower at the low frequency near dc, as expressed in eq.(2.4.9), in which the phase modulation index $\Delta\theta_A$ is in proportion to ω_A near $\omega_A = 0$. With regard to the electromechanical measurement described in §3.6, the electromechanical coefficient k which is in proportion to the piezoelectric constant is measured near the resonance frequency of the mode by using eq.(3.6.5) or (3.6.7), without using eq.(3.6.3) defined at dc.

We also determine the optical measurement of the piezoelectric vibration near the resonance frequency in order to obtain higher sensitivity. For the optical measurement of the piezoelectric constant which is defined at dc, we use the theory of simple harmonic oscillation described in §3.2. From eqs. (3.2.10) and (3.2.11), the amplitude of the vibration at the resonance, A_{res}, is Q times as large as that at $\omega_A \to 0$, A_0. Therefore, we can obtain A_0 by measurement near the resonance frequency as

$$A_0 = \frac{A_{res}}{Q}, \tag{3.7.6}$$

where the Q-value can be calculated by eqs.(3.2.14) and (3.2.15) and we must use the value of A_{res} at the first resonance. Equation (3.7.6) is applied to the calculation of the low frequency

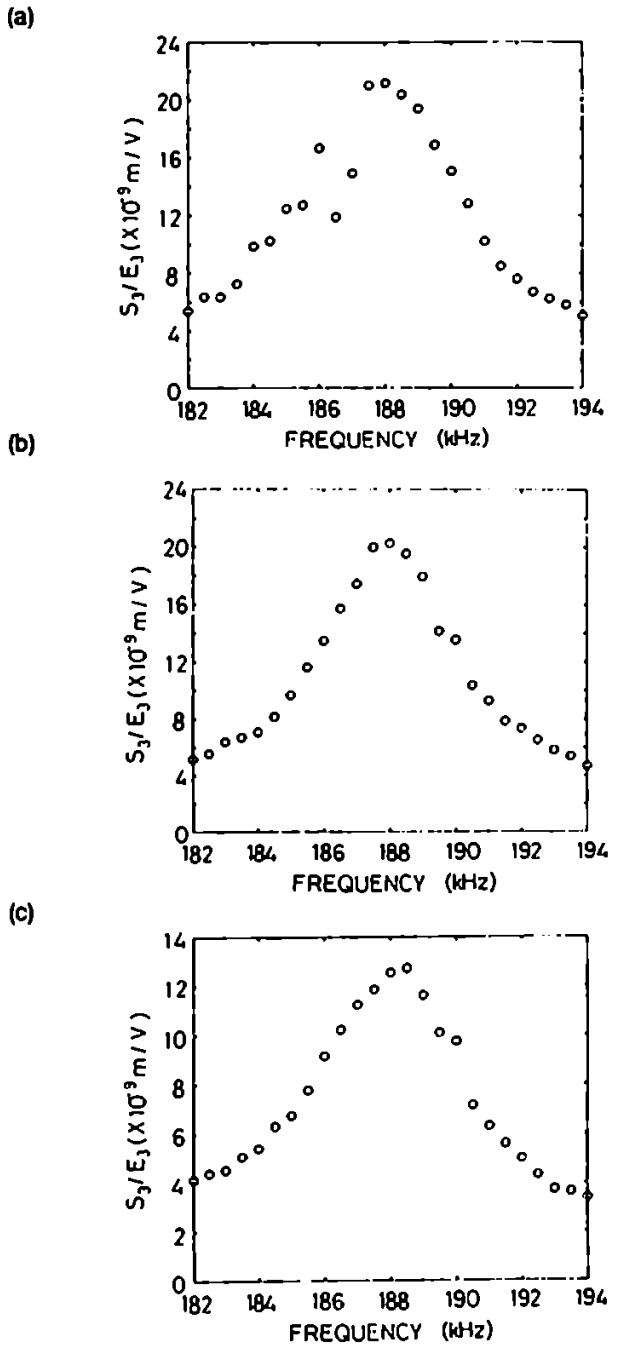

Fig. 3.9. Frequency characteristics of S_3 / E_3 near the first resonance (about 0.19 MHz) of the radial-extensional mode at the points (a) $r = 0$, (b) $r \approx 0.5R$, and (c) $r \approx 0.9R$ of the sample surface, respectively. The light for the measurement is incident in the z-direction.

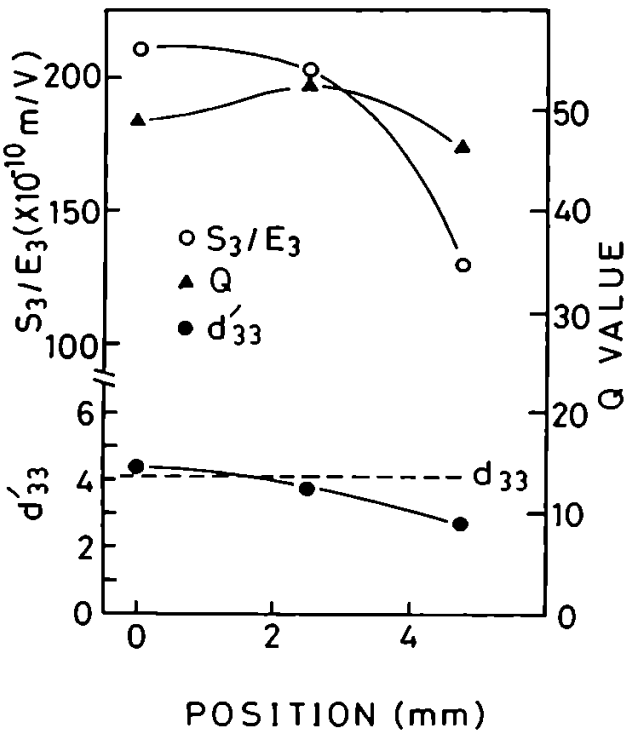

Fig. 3.10. Local characteristics of the maximum value of S_3 / E_3, the Q-value and the value of d'_{33} in the first resonance of the radial-extensional mode. The abscissa is distance from the center of the sample. A broken line shows the value of d_{33} given in Table 3.II.

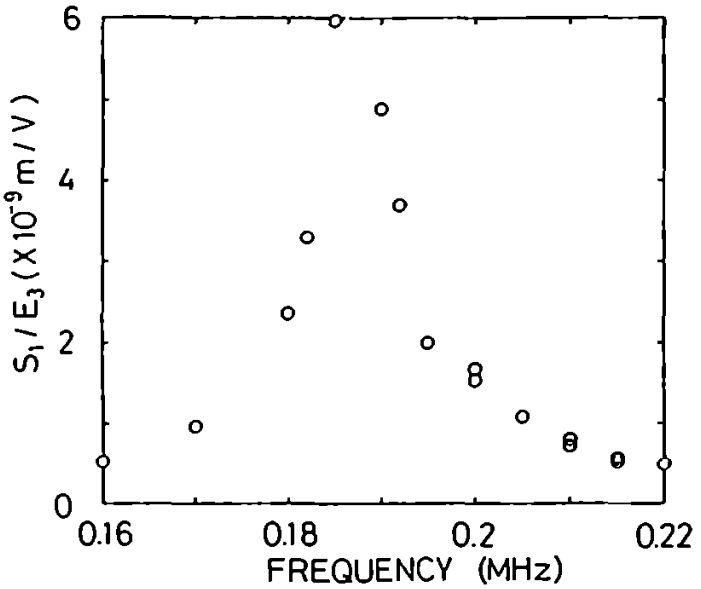

Fig. 3.11. Frequency characteristic of S_1 / E_3 near the first resonance of the radial-extensional mode. The light is incident in the r-direction.

limit of S / E.

In order to avoid confusing the d-constant as the material constant with the present d-like value, we call the latter "d'. " That is to say, we can obtain the value of "d' " according to

$$d'_{ij} = \frac{S_j / E_i \text{ (maximum)}}{Q}, \tag{3.7.7}$$

where we must use the value of S / E and Q at the first resonance. The Q-value is calculated by the frequency characteristic of S / E.

The experimental results are as follows. The light for the measurement is incident on some points (a) $r = 0$, (b) $r \simeq 0.5R$, and (c) $r \simeq 0.9R$ of the sample surface. Figures 3.9(a), 3.9(b), and 3.9(c) represent the frequency characteristics of S_3 / E_3 near the first resonance (about 0.19 MHz) of the radial-extensional mode at the points (a), (b), and (c) mentioned above, respectively.

We can read the maximum value of S_3 / E_3 and the Q-value at the resonance from Figs. 3.9 and obtain the value of d'_{33} by applying eq.(3.7.7). At point (a), S_3 / E_3 (max.) = 21.2×10^{-9} m/V and Q = 49.1 give $d'_{33} = 4.32\times10^{-10}$ m/V. At point (b), S_3 / E_3 (max.) = 20.3×10^{-9} m/V and Q = 53.2 give $d'_{33} = 3.82\times10^{-10}$ m/V. At point (c), S_3 / E_3 (max.) = 12.5×10^{-9} m/V and Q = 46.6 give $d'_{33} = 2.68\times10^{-10}$ m/V. These results are shown graphically in Fig. 3.10. We find that the maximum value of S_3 / E_3, the Q-value, and the value of d'_{33} are different locally and distributed variously. Ideally, from eq.(3.7.5), the value of d'_{33} should be the same regardless of the positions measured. The cause of such a distribution could be as follows: 1) the influence of the boundary of the sample; 2) the inequality of spontaneous polarization; and 3) the inequality of the electric field. Considering the shape and the high permittivity of the sample, cause 1) is the most probable. This means that the strain is not homogeneous even at zero frequency. Although the Q-value should ideally also be constant, the reason for the distribution may be the difference in the clamp state, which reflects the different frequency characteristics of the vibration.

A broken line in Fig. 3.10 shows the value of d_{33} (4.10×10^{-10} m/V) given in Table 3.II. Appraising the values of d_{33} and d'_{33}, we find that the value of d'_{33} is comparable to that of d_{33} at the center of the sample (5% larger), but rather smaller near the edge (35% smaller).

The value of d'_{31} can be also calculated by using eq.(3.7.7). The light for the measurement is incident on the point $r = R$ in the r-direction, as illustrated in Fig. 3.8(b). Figure. 3.11 shows the frequency characteristic of S_1 / E_3 near the first resonance. In this case, S_1 / E_3 (max.)= 6.0×10^{-9} m/V and Q = 29 give $d'_{31} = 2.1\times10^{-10}$ m/V, which is nearly in agreement with the value of d_{31} (-2.07×10^{-10} m/V) in Table 3.II.

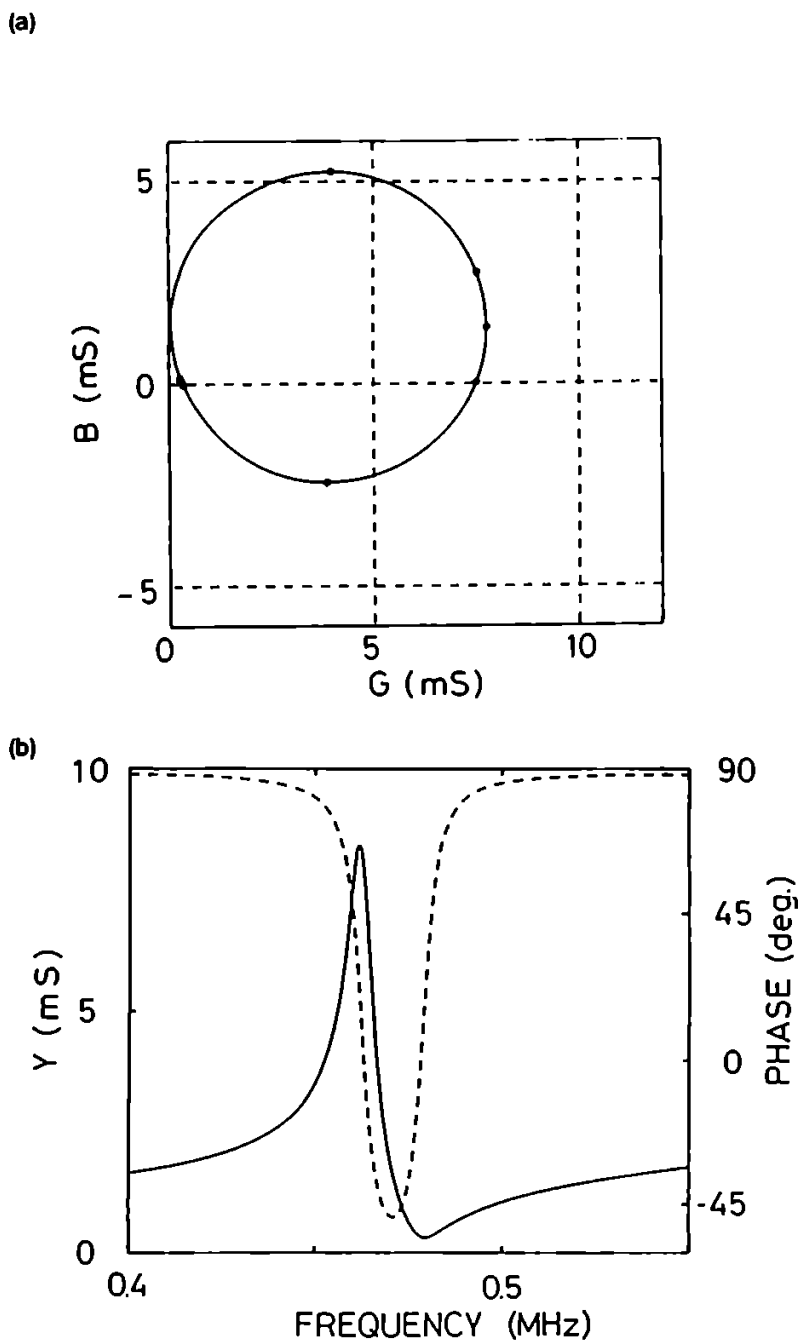

Fig. 3.12. Frequency characteristics of the admittance near the *second* resonance of the radial-extensional mode. (a) The G-B characteristic. (b) The solid line and the dashed line show the frequency characteristics of $|Y|$ and the phase angle of Y, respectively.

Table 3.VI. Typical results of the measurement of ω_{A1}, ω_m, ω_0, ω_r, ω_{A2}, ω_s, and ω_n near the *second* resonance of the radial-extensional mode.

$\omega_{A1}/(2\pi)$	0.4569 MHz	$\omega_{A2}/(2\pi)$	0.4635 MHz
$\omega_m/(2\pi)$	0.4596 MHz	$\omega_s/(2\pi)$	0.476 MHz
$\omega_0/(2\pi)$	0.4602 MHz	$\omega_n/(2\pi)$	0.478 MHz
$\omega_r/(2\pi)$	0.4608 MHz		

Table 3.VII. The Q-value, k_p^2 and the parameters of the equivalent circuit represented in Fig. 3.4, C_d, C_p, R_p, and L_p, calculated by the data in Table 3.VI.

Q	69.7	C_d	513 pF
k_p^2	0.078	C_p	38.2 pF
		R_p	130 Ω
		L_p	3.13 mH

3.7.2 Evaluation of Resonance of Higher Order

The first resonance of the radial extensional mode was used for the calculation of d' in §3.7.1. Here we describe the case of using the second resonance of the mode. Figures 3.12(a) and 3.12(b) show the results of electromechanical measurement at this resonance. Table 3.VI shows the values of ω_{A1}, ω_m, ω_0, ω_r, ω_{A2}, ω_a, and ω_n, and Table 3.VII shows the values of k^2, Q, and the other parameters of the equivalent circuit in Fig. 3.4. We find that the maximum value of $|Y|$ and the value of k^2 measured at the second resonance decrease compared with those at the first resonance. The reason is as explained below.

As described in §3.6.2, all modes of vibration can follow the external force without a phase lag at the low frequency limit; but, the vibration with lower resonance frequency cannot follow the external force and has a phase lag behind the force as the frequency of the force becomes higher. In the equivalent circuit illustrated in Fig. 3.2, all components of the elasticity C_1, C_2,C_3,$\cdots$, are effective in the frequency range under the first resonance; however, in the frequency range over the first resonance and under the second one, the first branch of the vibration is controlled by inductance L, that is, the inertia, and the components of the elasticity C_1 are neglected, and the others C_2, C_3, $\cdots$, are effective. The value of C_n (n = 0,1,2,3,$\cdots$) was represented in eqs. (3.4.22d) and (3.4.23b). From eqs. (3.4.19), (3.4.22d), (3.4.23b), and (3.4.23e), we can obtain

$$\sum_{n=1} C_n \propto k_p^2. \tag{3.7.8}$$

Therefore, the decrease of the effective components of C_n at higher frequency yields the apparent decrease of the electromechanical coupling coefficient, even though the coupling constant is defined at the low frequency limit. For example, the apparent value of k_p^2 measured at the second resonance becomes $1 - p_1$ times as large as the value of k_p^2 measured at the first resonance. In the present disk sample, $p_1 = 0.78$ is obtained by using eq.(3.4.23d) and the value in Tables 3.II and 3.III; therefore, $1 - p_1 = 0.22$. The electromechanical measurement gives

$k_p^2 = 0.37$ at the first resonance,

$k_p^2 = 0.078$ ($\equiv k'^2_p$) at the second resonance,

as in Tables 3.V and 3.VII, respectively. Therefore, the decrease of the coupling is

$$k'^2_p / k_p^2 = 0.078 / 0.37 = 0.21,$$

which is nearly in agreement with the theoretical value of $1 - p_1 = 0.22$.

On the other hand, using optical measurement, local measurement of the vibration is possible. Figures 3.13(a) and 3.13(b) show the frequency characteristics of S_3 / E_3 measured at the position

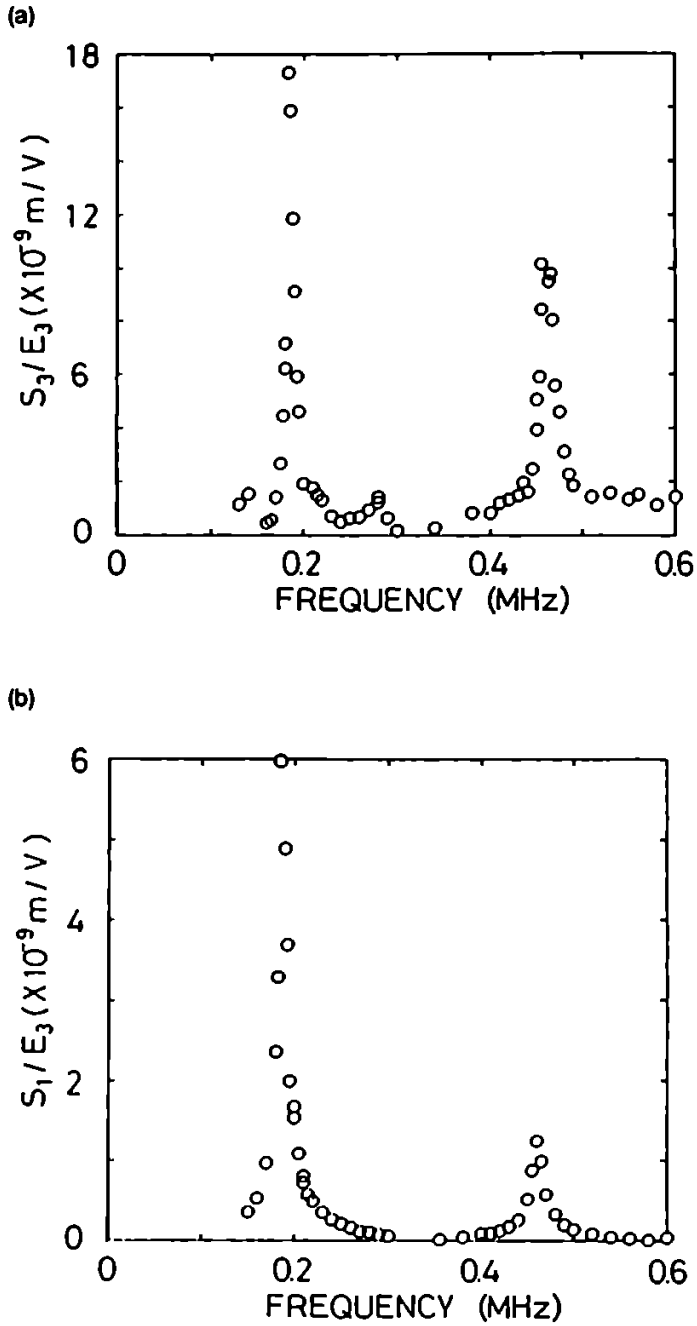

Fig. 3.13. (a), (b) Frequency characteristics of (a) S_3 / E_3 measured at the position $r = 0$ in the z-direction, and (b) S_1 / E_3 measured at the position $r = R$ in the r-direction.

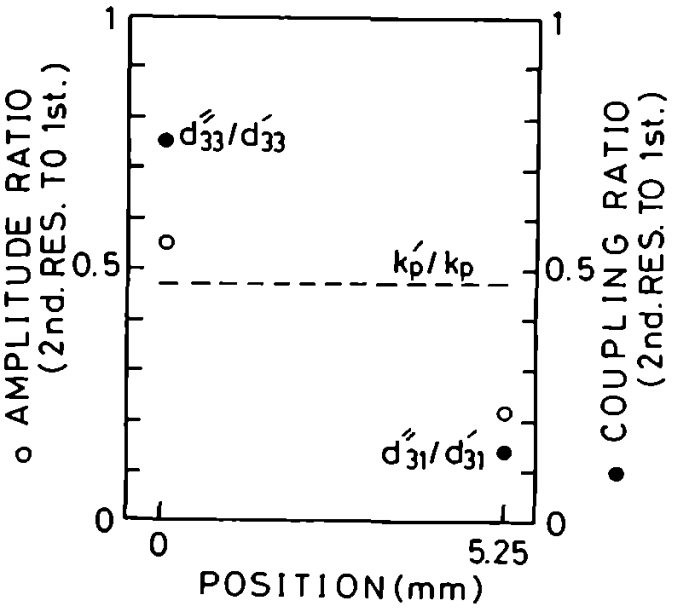

Fig. 3.14. Ratio of the maximum value of S/E at the second resonance to that at the first resonance and the ratio of d'' to d' at the positions $r = 0$ and $r = R$. The dashed line shows the ratio of k'_p to k_p.

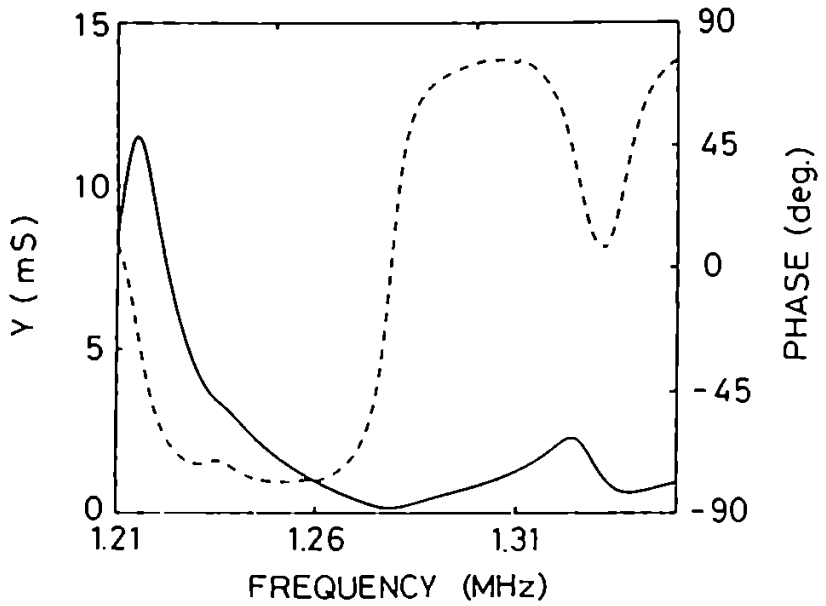

Fig. 3.15. Frequency characteristics of the admittance near the first resonance and antiresonance of the thickness-extensional mode. The solid line and the dashed line show $|Y|$ and the phase angle of Y, respectively.

Table 3.VIII. The Q-value, k_t^2 and the parameters of the equivalent circuit represented in Fig. 3.4, C_d, C_p, R_p, and L_p.

Q	110	C_d	159 pF
k_t^2	0.26	C_p	48.6 pF
		R_p	25.7 Ω
		L_p	0.386 mH

$r = 0$ in the z-direction and S_1 / E_3 measured at the position $r = R$ in the r-direction, respectively. The frequency range in Figs. 3.13(a) and 3.13(b) involves the first and the second resonances. The value of S_3 / E_3 at the position $r = 0$ at the second resonance is about 60% of that at the first resonance. The value of S_1 / E_3 at the position $r = R$ at the second resonance is only about 20% of that at the first resonance. This suggests that the vibration at the position $r = R$ has more difficulty following the external force than is the case at the position $r = 0$. As the frequency characteristics near the first resonance give the value of d' by using eq.(3.7.7), a similar calculation at the second resonance gives a value similar to d', which we call d''. Figure 3.14 shows the ratio of the maximum value of S / E at the second resonance to that at the first resonance and the ratio of d'' to d' at the positions $r = 0$ and $r = R$. The dashed line in Fig. 3.14 shows the ratio of k'_p to k_p. We find that the decrease of the electromechanical coupling varies locally, because it is more difficult for the vibration near the boundary to follow the external force at higher frequency, and the electromechanical coefficient measured by the electromechanical method is an average of the local value. The electric equivalent circuit in Fig. 3.2 expresses the average characteristics of the piezoelectric transducer as a whole. Therefore, the electric equivalent circuit is not effective for investigating the transducer from a local point of view.

3.7.3 Evaluation of Piezoelectric "g' " Value [1), 2)]

In this section, we describe the measurement of the thickness-extensional mode. Figure 3.15 and Table 3.VIII show the results of electromechanical measurement near the first resonance and antiresonance of this mode.

In the case of the measurement of the radial-extensional mode, we dealt with S / E as the fundamental value, considering the electrical condition of the mode with E as constant. As a result, the value d' corresponding to d can be measured as a parameter of the electromechanical coupling.

In contrast, the thickness-extensional mode is caused by the piezoelectric longitudinal effect as described in §3.3.4. The electrical condition in which the electric flux density D is constant can be adopted. For example, acoustic velocity is determined by the elastic stiffness c^D, where $D = 0$ is conditioned. In §3.5, the e-form was adopted for the fundamental piezoelectric relations, in which stress T and electric flux density D are the dependent variables and strain S and electric field E are the independent variables. From the viewpoint of optical measurement, it is desirable that the strain S be the dependent variable, and from the viewpoint of the electrical condition of the piezoelectric vibration in this mode, it is desirable that the electric flux density D be the independent variable. Therefore, we adopt the g-form expressed in eq.(3.3.7) as the piezoelectric fundamental relation. As in the case of the radial-extensional mode, we can calcu-

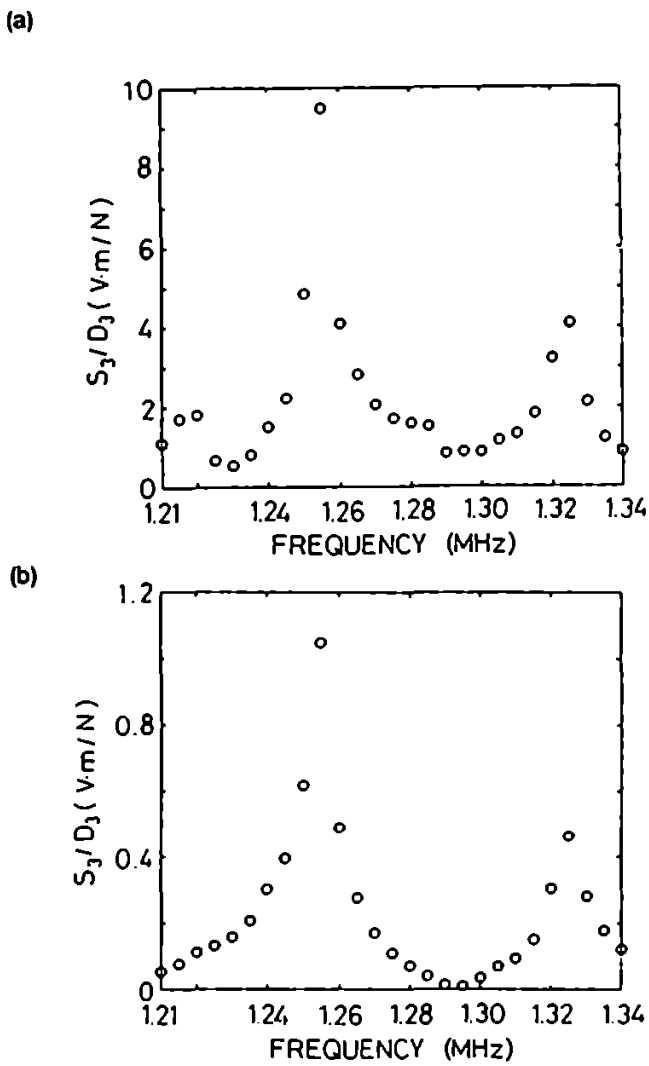

Fig. 3.16. (a), (b) Frequency characteristics of S_3 / D_3 near the first antiresonance (about 1.3 MHz) of the thickness-extensional mode measured at the positions (a) $r = 0$ and (b) $r \approx 0.9R$ of the sample surface in the z-direction, respectively.

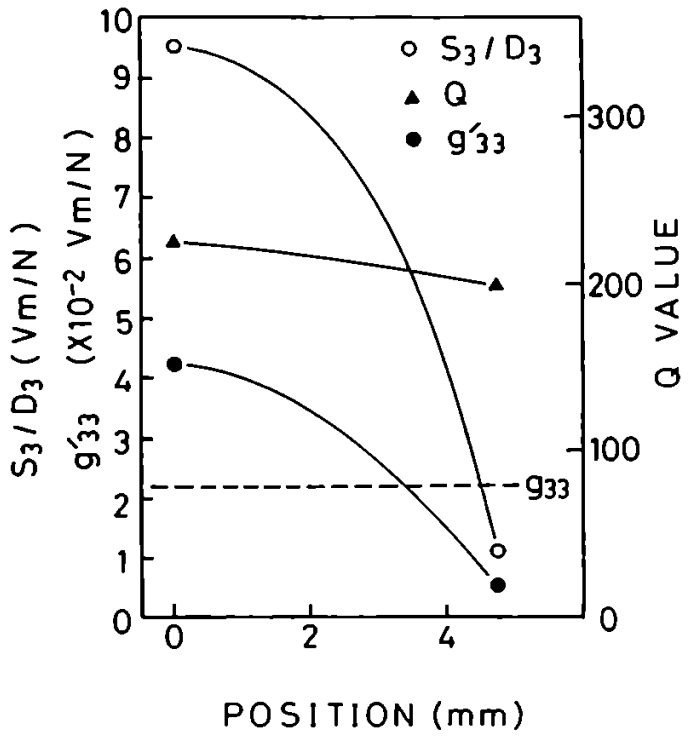

Fig. 3.17. The maximum value of S_3 / D_3, the Q-value, and the value of g'_{33} measured at the first antiresonance of the thickness-extensional mode. A broken line shows the value of g_{33} shown in Table 3.II.

(a)

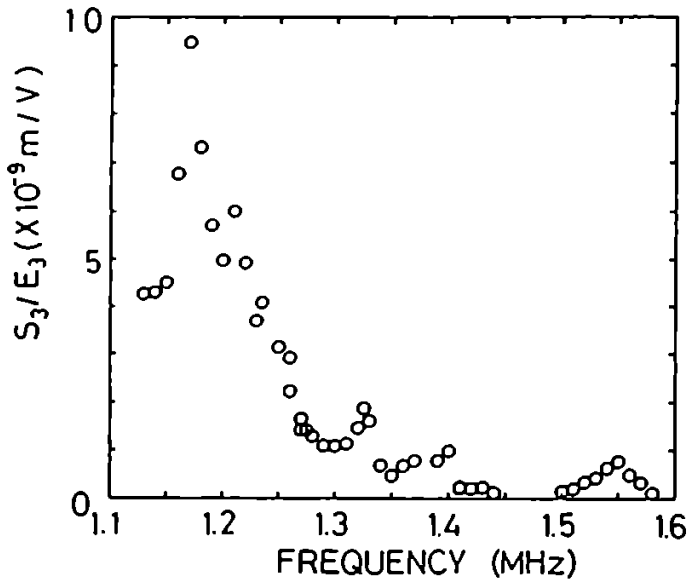

(b)

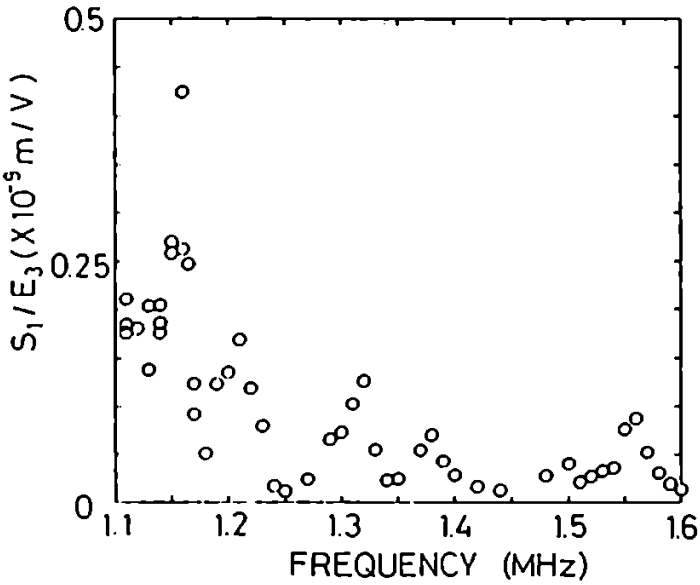

Fig. 3.18. (a), (b) Frequency characteristics of S / E of the *thickness-extensional* mode measured at the position (a) $r = 0$ in the z-direction and at the position (b) $r = R$ in the r-direction, respectively.

late the value corresponding to the piezoelectric g-constant using the frequency characteristics of S/D by

$$g'_{ij} = \frac{S_j / D_i \,(\text{maximum})}{Q}, \tag{3.7.9}$$

where we must use the value of S/D and Q at the first antiresonance.

In the thickness-extensional mode, the vibration is clamped in the r-direction, and the stress T is not zero at the circumference of the sample. As a result, the low frequency limit of S/D cannot be expected to agree with the g-constant, because $T = 0$ is not satisfied in eq.(3.3.7) even at the low frequency limit. However, the value of g' can be a criterion for the evaluation of the transducer.

The value of D_3 can be calculated as

$$|Y| = \frac{|I|}{|V|} = \frac{\omega_A D_3 \pi R^2}{V}, \tag{3.7.10}$$

where the voltage V between the two electrodes on the z-plane and the result of the electromechanical measurement shown in Fig. 3.15 are used. The experimental results are as follows. The light for the measurement is incident on two positions (a) $r = 0$, and (b) $r \approx 0.9R$ of the sample surface in the z-direction. Figures 3.16(a) and 3.16(b) represent the frequency characteristics of S_3/D_3 near the first antiresonance (about 1.3 MHz) of this mode at the positions (a) and (b) mentioned above, respectively. Figure 3.17 shows the maximum value of S_3/D_3, the Q-value, and the value of g'_{33} obtained by Figs. 3.16 and eq.(3.7.9). At point (a), S_3/D_3 (max.) = 9.50 V·m/N and $Q = 224$ give $g'_{33} = 42.4\times10^{-3}$ V·m/N. At point (b), S_3/D_3 (max.) = 1.05 V·m/N and $Q = 198$ give $g'_{33} = 5.30\times10^{-3}$ V·m/N.

A broken line in Fig. 3.17 shows the value of g_{33} (22×10^{-3} V·m/N) given in Table 3.II. We find that the value of g'_{33} is much (76%) smaller at the edge of the sample and much (93%) larger at the center than that of g_{33} due to the influence of the boundary. The ratio of the value of g' at the center to that at the edge is large, compared to d'. The influence of the boundary on the results of the measurement of g' is seen to be stronger than that of the measurement of d', because the resonance frequency of the thickness-extensional mode is much higher than that of the radial-extensional mode. Hence, a much stronger effect of the clamp may exist in the former case.

For reference, the frequency characteristics of S/E of this mode are shown below. Figure 3.18(a) and 3.18(b) show the frequency characteristics of S/E measured at the position $r = 0$ in the z-direction and at the position $r = R$ in the r-direction, respectively. As in the case of the radial-extensional mode, strain S approaches the maximum at the electrical resonance, because the electric current I which is caused by the piezoelectric vibration approaches the maximum at

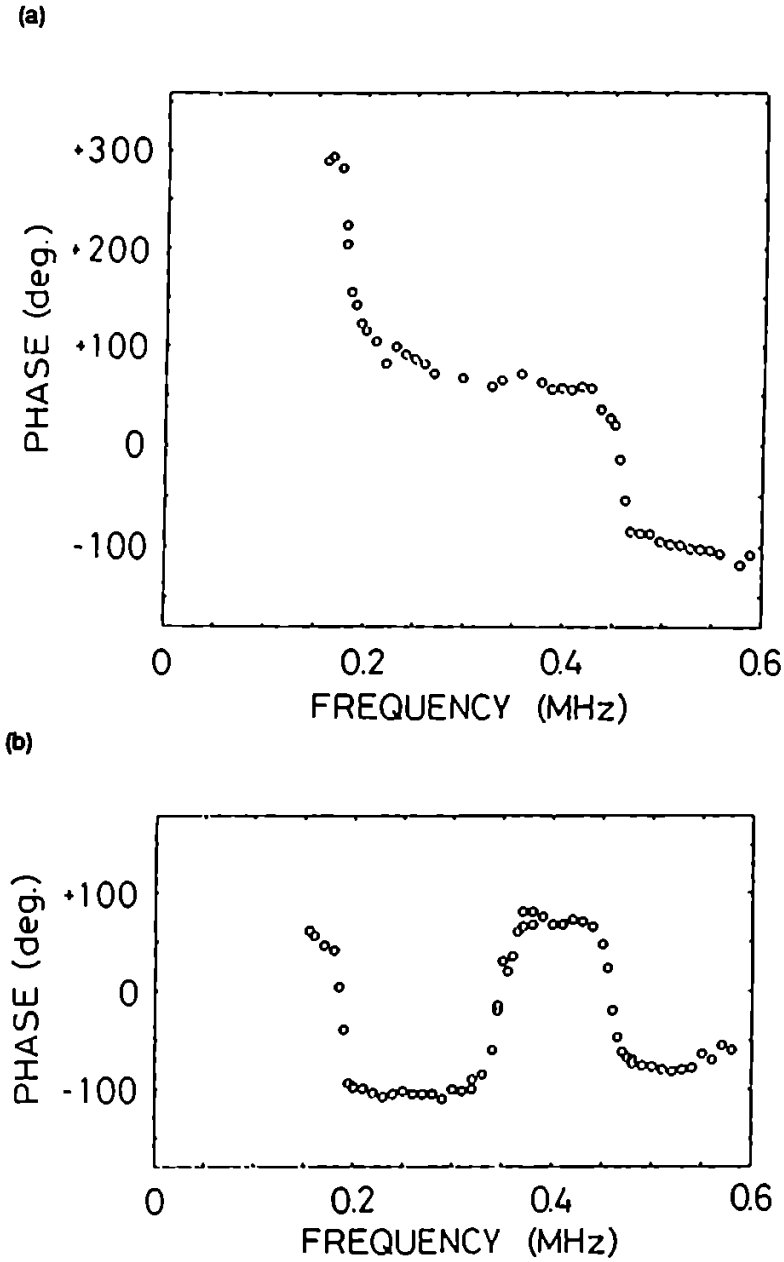

Fig. 3.19. (a),(b) Frequency characteristics of the phase of the acoustic vibration measured at the positions (a) $r = 0$ of the sample surface in the z-direction and (b) $r = R$, the edge of the sample, in the r-direction.

the electrical resonance when the voltage is constant. The strain S_1 in the r-direction is much smaller compared with that in the radial-extensional mode because of the mechanical clamp.

§3.8. Evaluation of Piezoelectric Vibration by Optical Measurement of Acoustic Phase[4)]

3.8.1 Evaluation of Acoustic Velocity and Poisson's Ratio

Using the optical method described in §2.4, phase of acoustic vibration (strictly speaking, the sum of the phase difference between the acoustic vibration to be measured and the driving voltage of the vibration and some phase value dependent on the experimental system) can be measured. At electrical resonance frequencies of the sample, the frequency characteristic of the phase mentioned above changes by about $-\pi$ radians. At electrical antiresonance frequencies, a phase shift of $+\pi$ cannot be observed with the present optical measurement method, unlike the electric measurement of admittance. The reason for this is discussed in §3.8.2. In the case of radial-extensional vibration, another phase shift of π can occur locally at other than the resonance and antiresonance frequencies. In this section, new methods of measurement of acoustic velocity and Poisson's ratio of the material are described, by optically measuring of the acoustic phase *locally*.

The light is incident on the sample surface at positions (a) $r = 0$ of the sample surface in the z-direction and (b) $r = R$, the edge of the sample, in the r-direction. Figures 3.19(a) and 3.19(b) show the frequency characteristics of the phase of acoustic vibration at positions (a) and (b) mentioned above, respectively. The range of the frequency in Figs. 3.19(a) and 3.19(b) involves the first and the second resonances of the radial-extensional mode the frequencies of which are about 0.187 and 0.460 MHz, respectively. Phase shifts of approximately $-\pi$ can be observed at the two resonances in both Fig. 3.19(a) and Fig. 3.19(b). These phase shifts are characteristic of the sample as a whole. On the other hand, another phase shift of approximately π can be observed at 0.348 MHz between the two resonances only in Fig. 3.19(b). This phase shift is a local characteristic of the sample.

In order to investigate the local characteristics of the sample, theoretical analysis of the vibration is necessary. We have expressed the displacement of the radial extensional vibration of a thin disk in the r-direction in eqs. (3.4.10), (3.4.11), (3.4.15), and (3.4.16a). The pole of coefficient B' in eq.(3.4.15) determines the frequencies of the resonance, which describes characteristics of the entire sample. That is, the resonance frequencies can be obtained by eq.(3.4.17). In addition, the zero of the Bessel function in eq.(3.4.11) determines the frequencies at which the phase of $u(r)$ can change by π. Since the Bessel function in eq.(3.4.11) is a function of position r, the present phase shift is a local characteristic of the sample. The Bessel function $J_1(x)$

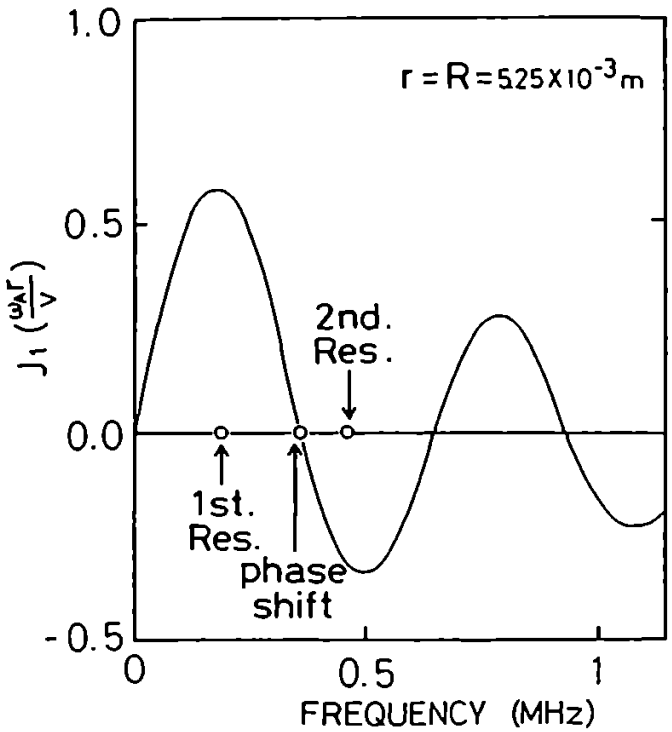

Fig. 3.20. Frequency characteristic of $J_1(\omega_A R/v)$. In the case of the present disk sample, the phase shift can occur at the frequency between the first and the second resonances determined by eq.(3.8.1).

approaches zero and changes the algebraic sign when $x = 3.83$; therefore, at the side of disk $r = R$, the present phase shift can occur at the frequency determined by

$$\frac{\omega_A R}{v} = 3.83. \tag{3.8.1}$$

The frequency of this phase shift can be measured by the incidence and reflection of light on the side of the disk sample in the r-direction, and the acoustic velocity v can be calculated by using eq.(3.8.1). The frequency cannot be measured by the usual electromechanical method described in §3.6, because local characteristics of the sample cannot be measured by this method.

The curve in Fig. 3.20 shows the frequency characteristic of $J_1(\omega_A R/v)$. In the case of the present disk sample, the phase shift can occur at the frequency between the first and the second resonances determined by eq.(3.8.1). Substitution of the experimental result into eq.(3.8.1) gives

$$v = 3.00\times10^3 \text{ m/s}.$$

The measurement of v of a disk transducer usually requires the measurement of both the resonance frequency and Poisson's ratio σ, because the resonance frequencies are determined by eq.(3.4.17) including σ. On the other hand, the optical method described here does not require the measurement of σ.

Poisson's ratio σ can be calculated using the value of v just measured. The value of σ can be calculated with the following two methods. First, eqs. (3.4.16b) and (3.4.17) can be used for the calculation. Substitution of the value of v measured by means of the method mentioned above and the first resonance angular frequency into eq.(3.4.16b) gives the value of $\alpha = \alpha_1$ which satisfies eq.(3.4.17). Then, Poisson's ratio σ can be calculated using eq.(3.4.17). Second, since v can be expressed in eq.(3.4.12), substitution of the value of v, ρ and s^E_{11} into eq.(3.4.12) gives the value of σ. The second method is now adopted. Substitution of the value of v and the material constants in Table 3.II into eq.(3.4.12) gives

$$\sigma = 0.31.$$

When $\sigma = 0.31$, the smallest value of α satisfying eq.(3.4.17), α_1, is 2.06 from Table 3.III. The value of $\alpha_1 = 2.06$ corresponds to a frequency 0.187 MHz due to eq.(3.4.16b), which is almost in agreement with the first resonance frequency actually measured. This verifies the accuracy in measuring the acoustic velocity and Poisson's ratio with the present optical method.

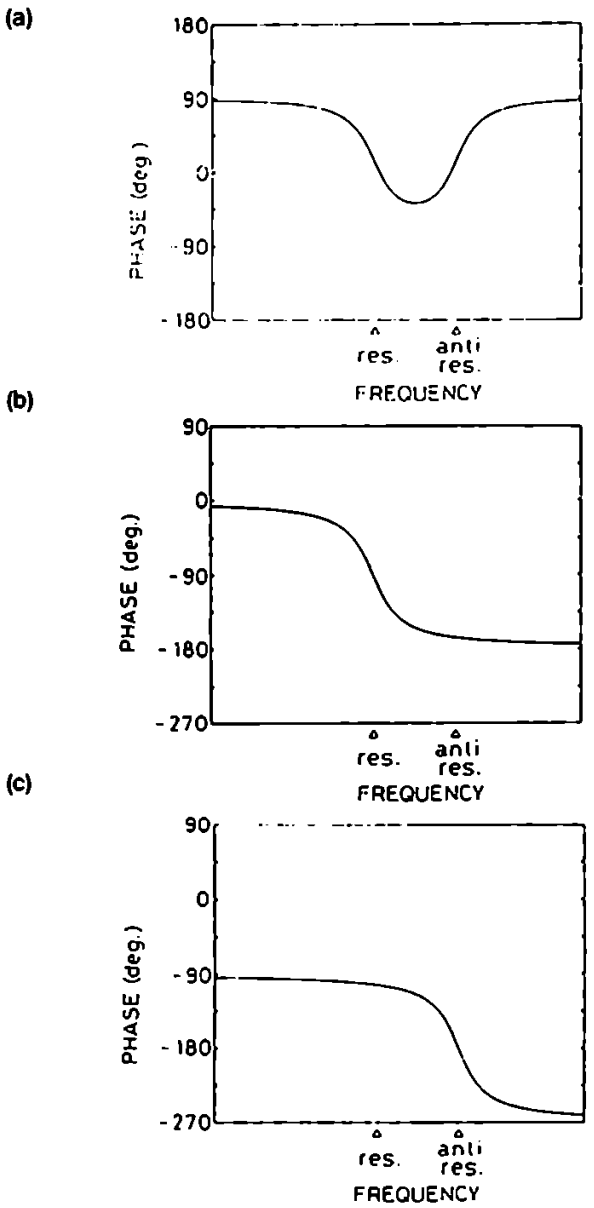

Fig. 3.21. (a) Phase difference between the current *I* and the voltage *V* changes by $-\pi$ at the electric resonance, and by $+\pi$ at the electric antiresonance because of the influence of the genuine electric capacity. (b) In the case of piezoelectric transverse effect, the phase difference between *u* and *V* changes by $-\pi$ at the electrical resonance.
(c) In the case of piezoelectric longitudinal effect, the phase difference between *u* and *I* changes by $-\pi$ at the electrical antiresonance.

3.8.2 Phase Shift in Electromechanical and Optical Measurement

Using the optical measurement described here, the phase shift of $-\pi$ can be observed at the electric resonance frequencies, and the phase shift of $+\pi$ cannot be observed at the antiresonance frequencies. The reason for this is explained below.

The phase difference between mechanical displacement u and driving force F changes by $-\pi$ at the mechanical resonance. This phase shift corresponds to the change of the vibrational state from stiffness control to inertia control via resistance control. In the electrical measurement of the admittance, the phase difference between current I and voltage V changes by $-\pi$ at the electrical resonance, and by $+\pi$ at the electrical antiresonance because of the influence of the genuine electric capacity, as illustrated in Fig. 3.21(a)

In the case of piezoelectric vibration resulting from the transverse effect, V corresponds to F, and the electrical resonance corresponds to the mechanical resonance, as discussed in §3.5. Using the optical method described here, the phase difference between u and V can be measured; therefore, the phase shift of $-\pi$ can be observed at the electrical resonance, as in Fig. 3.21(b). Since the measurement of u cannot be influenced by the genuine electric capacity, the phase shift of $+\pi$ cannot be observed at the electrical antiresonance, as in Fig. 3.21(b).

In the case of piezoelectric vibration resulting from the longitudinal effect, I corresponds to F, and the electrical antiresonance corresponds to the mechanical resonance, as discussed in §3.5; therefore, the phase difference between u and I can change by $-\pi$ at the electrical antiresonance, as in Fig. 3.21(c). On the other hand, the phase difference between I and V can change by $-\pi$ at the electrical resonance, and by $+\pi$ at the electrical antiresonance, as in Fig. 3.21(a); therefore, the phase difference between u and V observed by the optical method can change by $-\pi$ at the electrical resonance, and cannot change at the electrical antiresonance, as in Fig. 3.21(b), because of the neutralization of the two phase shifts $-\pi$ in Fig. 3.21(c) and $+\pi$ in Fig. 3.21(a).[6]

§3.9. Summary

Optical measurement of the acoustic amplitude and phase of the piezoelectric disk transducer was performed locally.

Optical measurement of the acoustic amplitude gave the values corresponding to the piezoelectric constants d and g locally, evaluating the theory of vibration, the electrical condition of the piezoelectric vibration, and the results of electromechanical measurement. It was found that the electrical equivalent circuit was not effective for analysis of the transducer from a local point of view, because the vibration near the boundary made it more difficult to follow the external force at higher frequency.

Optical measurement of the acoustic phase gave the acoustic velocity of the radial-extension-

al mode and the value of Poisson's ratio, utilizing local characteristics of the sample.

References

1) M.Ohki and T.Shiosaki: *Proc. IEEE Ultrasonics Symp.,Florida, 1991* (IEEE, Piscataway, 1991) p.615

2) M.Ohki, N.Shima and T.Shiosaki: IEICE Tech.Rep., US90-71,EA90-84 (1991.1.25) [in Japanese]

3) M.Ohki, T.Kita and T.Shiosaki: IEICE Tech.Rep., US91-23 (1991.7.16) [in Japanese]

4) M.Ohki, N.Shima and T.Shiosaki: Jpn.J.Appl.Phys., **32**(1993) 2463.

5) T.Ikeda: *Fundamentals of Piezoelectricity* (Oxford University Press, 1990)

6) M.Ohki, N.Shima and T.Shiosaki: IEICE Tech.Rep., US91-79,EA91-92 (1992.1.28) [in Japanese]

Chapter 4
Influence of Resonance Coupling on Measurement of Piezoelectric Vibration

§4.1. Introduction

In the previous chapter, piezoelectric vibration was evaluated by electromechanical and optical methods. These new methods for evaluating the piezoelectric transducer were described, and the quantities determined by the material constants were measured. The disk piezoelectric transducer was used as the sample.

In our study of piezoelectric transducers, it is important to analyze form as well as material constants to determine their characteristics. For example, in the case of the columnar piezoelectric transducers made of the same material, the characteristics such as acoustic velocities and the resonance frequencies can change if the ratio of the height to the radius of the column is changed. The variation of the characteristics is related to the variation of the state of the mechanical clamp.

If the ratio of the height to the radius of the column is quite large or small, the vibration of a mode which has a lower resonance frequency cannot be affected at its resonance frequency by the vibration of another mode which has a higher resonance frequency. The vibration is free in both directions; however, at the resonance frequency of the latter mode, which is higher than that of the former, the amplitude of the former vibration is very small, though the amplitude of the latter vibration approaches the maximum. In this case, the vibration is clamped in one direction and free in the other direction. Because of the mechanical clamp, the acoustic velocity of this mode will be higher than that of the mode with free vibration in both directions.

If the ratio of the height to the radius approaches unity, the states of the mechanical clamp of the respective modes are affected by each other, and reach an equilibrium between free and clamped.

In this chapter, the optical measurement methods described in the previous chapter are applied to columnar piezoelectric transducers with different ratios of height and radius, and the experimental results are considered from the viewpoint of resonance coupling of the two vibrational modes.[1),2)] The theory of the resonance coupling has long been used for the analysis of the variation of resonance frequency when the form of the transducer is changed.[3)] We apply this theory in a unique way using optical measurement.

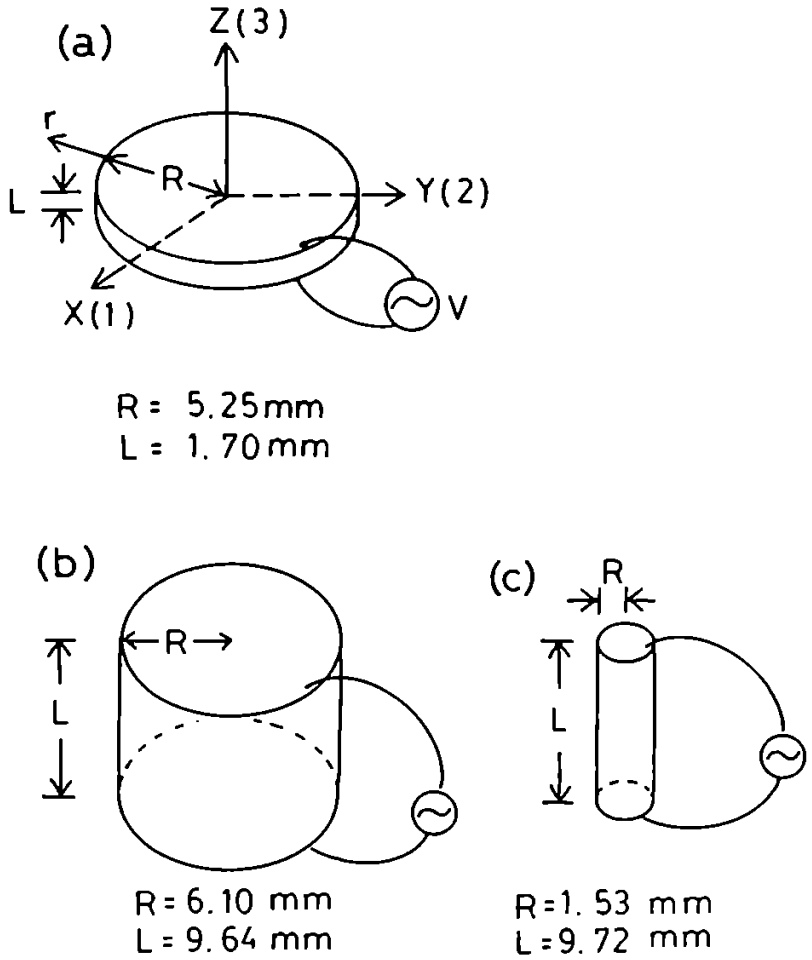

Fig. 4.1. Configuration of the samples for the measurement. They include circular piezoelectric ceramics of three forms. The value of p will be defined later in eq.(4.4.6). (a) $p = 0.223$. (b) $p = 1.09$. (c) $p = 4.37$.

§4.2. Samples for Measurement

4.2.1 Forms of Samples

The samples for our measurement are piezoelectric ceramics of the three types shown in Fig. 4.1, made of the same material as described in the previous chapter (PZT material "P-7" polarized in the direction of length; z-direction). The main material constants are shown in Table 3.II. The characteristics of the vibration in the disk sample illustrated in Fig. 4.1(a) were discussed in the previous chapter. The light is incident on the sample surface locally and reflected in the z-direction in Fig. 4.1. Silver electrodes are sintered on both faces of the sample. Changing point of measurement enables us to evaluate the sample locally.

4.2.2 Vibrational Theory of Circular Long Rod

The vibration of the circular long rod sample, as illustrated in Fig. 4.1(c), can be easily analyzed as in the case of disk sample, because its mechanical conditions are evident. In the latter case, as discussed in §3.4 and §3.5, for the radial-extensional mode in the piezoelectric transverse effect ($P \perp k$, $k \parallel r$-direction), the mechanical and electrical conditions were given by

$$T_{zz} = 0, \quad \text{that is, free on the } z\text{-planes,} \tag{4.2.1}$$

$$\partial E_z / \partial r = 0, \tag{4.2.2}$$

as described in eqs. (3.4.5) and (3.4.6). For the thickness-extensional mode in the piezoelectric longitudinal effect ($P \parallel k$, $k \parallel z$-direction), the mechanical and electrical conditions were given by

$$S_{rr} = S_{\theta\theta} = 0\,, \quad \text{that is, clamped in the } r\text{- and } \theta\text{-directions,} \tag{4.2.3}$$

$$\partial D_z / \partial z = 0\,, \tag{4.2.4}$$

as described in eqs. (3.5.4) and (3.5.5).

In the case of circular *long rod* sample, two modes, the length-extensional and the radial-extensional exist in the z- and r-directions, respectively. However, their mechanical conditions are different from those of the thin disk sample.

In the *length-extensional* mode of the circular long rod, the vibration is caused by the piezoelectric longitudinal effect ($P \parallel k$, $k \parallel z$-direction), and the mechanical conditions are given by

$$T_{rr} = T_{\theta\theta} = 0, \quad \text{that is, free in the } r\text{- and } \theta\text{-directions,} \tag{4.2.5}$$

and the electrical condition is the same as eq.(4.2.4). The fundamental piezoelectric relations are given by the g-form as

$$S_r = s^D_{13} T_z + g_{31} D_z , \tag{4.2.6a}$$

$$S_\theta = s^D_{13} T_z + g_{31} D_z , \tag{4.2.6b}$$

$$S_z = s^D_{33} T_z + g_{33} D_z , \tag{4.2.6c}$$

where the mechanical condition eq.(4.2.5) has been already included. The Newton's equation of motion is given by

$$\rho \frac{\partial^2 u_z}{\partial t^2} = \frac{\partial T_z}{\partial z} . \tag{4.2.7}$$

Simultaneous equations (4.2.6c) and (4.2.7) involving both the electrical condition eq.(4.2.4) and the mechanical boundary condition,

$$T_z = 0 \quad \text{at} \quad z = \pm L/2, \tag{4.2.8}$$

are solved as

$$u_z = u(z) \exp(-j\omega_A t), \tag{4.2.9a}$$

where

$$u(z) = B' \sin(\omega_A z/v) , \tag{4.2.9b}$$

$$B' = \frac{g_{33} D_z}{(\omega_A/v) \cos(b)} , \tag{4.2.9c}$$

where

$$v = (\rho s^D_{33})^{-1/2} , \tag{4.2.10}$$

is the acoustic velocity of the mode, and b is given by

$$b = \omega_A L/ (2v). \tag{4.2.11}$$

When

$$b = b_m \equiv \omega_{Am} L / (2v) = m\pi / 2 \quad (m = 1,3,5,\cdots), \tag{4.2.12}$$

the mechanical resonance occurs as described by eqs. (4.2.9b) and (4.2.9c), and the electrical antiresonance occurs because of the piezoelectric longitudinal effect, as discussed in §3.5.

In the *radial-extensional* mode of the circular long rod, the vibration is caused by the piezoelectric transverse effect ($P \perp k$, k // r-direction), and the mechanical conditions are given by

$$S_z = 0, \quad \text{that is, clamped in the } z\text{-direction}, \tag{4.2.13}$$

and the electrical condition is the same as eq.(4.2.2). The fundamental piezoelectric relations

are given by the e-form as

$$T_{rr} = c^{E}_{11}S_{rr} + c^{E}_{12}S_{\theta\theta} - e_{31}E_z, \tag{4.2.14a}$$

$$T_{\theta\theta} = c^{E}_{12}S_{rr} + c^{E}_{11}S_{\theta\theta} - e_{31}E_z, \tag{4.2.14b}$$

$$T_{zz} = c^{E}_{13}S_{rr} + c^{E}_{13}S_{\theta\theta} - e_{33}E_z, \tag{4.2.14c}$$

where the mechanical condition eq.(4.2.13) has been already incorporated. The Newton's equation of motion is given by

$$\rho \frac{\partial^2 u_r}{\partial t^2} = \frac{\partial T_{rr}}{\partial r} + \frac{T_{rr} - T_{\theta\theta}}{r}, \tag{4.2.15}$$

Simultaneous equations (4.2.14a), (4.2.14b) and (4.2.15) involving both the electrical condition eq.(4.2.2) and the mechanical boundary condition,

$$T_{rr} = 0 \quad \text{at} \quad r = R, \tag{4.2.16}$$

are solved as

$$u_r = u(r) \exp(-j\omega_A t), \tag{4.2.17a}$$

where

$$u(r) = B' J_1(\omega_A r/v), \tag{4.2.17b}$$

$$B' = \frac{e_{31} E_z R}{c^{E}_{11}\alpha J_0(\alpha)+(c^{E}_{12}-c^{E}_{11})J_1(\alpha)}, \tag{4.2.17c}$$

where

$$v = (c^{E}_{11} / \rho)^{1/2}, \tag{4.2.18}$$

is the acoustic velocity of this mode, and α is given by

$$\alpha = \omega_A R/ v. \tag{4.2.19}$$

The mechanical resonance angular frequencies $\omega_{An} = \alpha_n v/R$ (n = 1,2,3,$\cdots$) can be obtained by

$$c^{E}_{11}\alpha_n J_0(\alpha_n) + (c^{E}_{12}-c^{E}_{11})J_1(\alpha_n) = 0. \tag{4.2.20}$$

Then, the electrical resonance occurs because of the piezoelectric transverse effect, as discussed in §3.4.

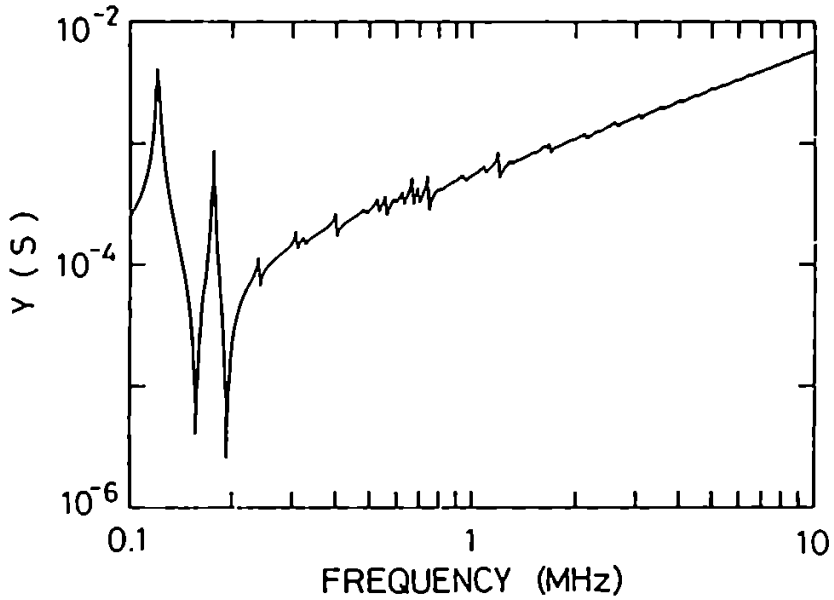

Fig. 4.2. Frequency characteristic of the admittance in the thick rod sample illustrated in Fig. 4.1(b).

§4.3. Measurement of d' and g'

4.3.1 Measurement for Disk Sample

The results of the electromechanical measurement of the disk sample (illustrated in Fig. 4.1(a)) were shown in Fig. 3.6. Optical measurement of the radial-extensional mode was carried out locally near the first and lowest resonance frequency (about 0.19 MHz) and of the thickness-extensional mode near the first antiresonance frequency. The frequency of the latter (about 1.3 MHz) is much higher than the former.

In the former case, the vibration was caused by the piezoelectric transverse effect, and the value of S / E was adopted as the fundamental quantity. Figure 3.10 showed spatial distribution of the maximum value of S_3/E_3, the Q-value, and the value of d'_{33} calculated by eq.(3.7.7) together with the value of d_{33} shown in Table 3.II.

In the latter case, the vibration was caused by the piezoelectric longitudinal effect, and the value of S / D was adopted as the fundamental quantity. Figure 3.17 showed spatial distribution of the maximum value of S_3/D_3, the Q-value, and the value of g'_{33} calculated by eq.(3.7.9) together with the value of g_{33} shown in Table 3.II. The influence of the boundary of the sample on the measurement of g' was seen to be stronger than that of d', because the resonance frequency of the disk sample's thickness-extensional mode was much higher than its radial-extensional mode.

4.3.2 Measurement for Thick Rod Sample

In the *thick rod* sample illustrated in Fig. 4.1(b), the result of the electromechanical measurement, the frequency characteristic of the admittance, is shown in Fig. 4.2. Similar optical measurements are performed for the length- and the radial-extensional modes of this sample. The resonance frequency of the former (about 0.12 MHz) is lower than that of the latter (about 0.175 MHz); and the former being due to the piezoelectric longitudinal effect, and the latter due to the piezoelectric transverse effect. Therefore, we adopt the S / D as the fundamental value for the former case, and the S / E for the latter case. The light for the measurement is incident on the sample surface at positions (a) $r \approx 0$ and (b) $r \approx 0.9R$ in the z-direction.

The S_3/D_3(max.), Q-value and g'_{33} for the former case, and the S_3/E_3(max.), Q-value and d'_{33} for the latter case are shown in Figs. 4.3(a) and 4.3(b), respectively. For the former antiresonance, at position (a) $r \approx 0$, S_3/D_3(max.) = 4.02 V·m/N and Q = 230 give $g'_{33} = 1.75\times10^{-2}$ V·m/N, which is 79.5% of the value of g_{33}, and at position (b) $r \approx 0.9R$, S_3/D_3(max.) = 3.08×10^{-1} V·m/N and Q = 239 give $g'_{33} = 1.29\times10^{-3}$ V·m/N, which is 5.86% of the value of g_{33}. For the latter resonance, at position (a) $r \approx 0$, S_3/E_3(max.) = 2.59×10^{-9} m/V and Q = 63.7 give $d'_{33} = 4.07\times10^{-11}$ m/V, which is 9.93% of the value of d_{33}, and at position (b) $r \approx 0.9R$,

(a)

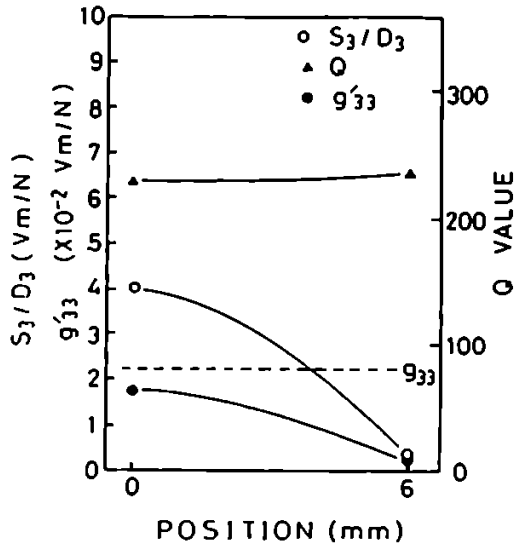

(b)

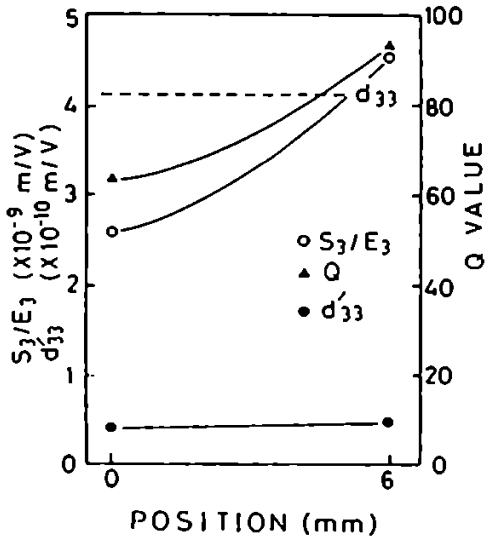

Fig. 4.3. (a) Spatial distribution of the S_3/D_3(max.), Q-value and g'_{33} measured at the first resonance caused by the length-extensional mode in the thick rod sample illustrated in Fig.4.1(b). (b) Spatial distribution of the S_3/E_3(max.), Q-value and d'_{33} measured at the second resonance caused by the length-extensional mode in the same sample. The abscissa is distance from the center of the sample. Broken lines show the values of g_{33} and d_{33} given in Table 3.II.

S_3/E_3(max.) = 4.59×10^{-9} m/V and Q = 93.4 give d'_{33} = 4.91× 10^{-11} m/V, which is 12.0% of the value of d_{33}. In each case, the values of g'_{33} and d'_{33} are much smaller than those of g_{33} and d_{33}, respectively. One of the reasons for these results may be the influence of the resonance coupling of the two modes. This will be discussed later using the theory of coupled resonance in the context of measuring d' and g'.

With regard to the former resonance, in which S / D is adopted as the fundamental value, the resonance curve of S_3 / E_3 cannot be plotted near the resonance at position (a) $r \approx 0$; therefore, the value of d'_{33} cannot be measured. However, the resonance curve of S_3 / E_3 can be plotted at position (b) $r \approx 0.9R$; therefore, the value of d'_{33} can be measured to be 1.12×10^{-10} m/V, which is 27% of the value of d_{33}. For the latter resonance, in which S / E is adopted as the fundamental value, the resonance curve of S_3 / D_3 cannot be plotted near the antiresonance at position (a) $r \approx 0$; therefore, the value of g'_{33} cannot be measured. However, the resonance curve of S_3 / D_3 can be plotted at position (b) $r \approx 0.9R$; therefore, the value of g'_{33} can be measured as 1.14×10^{-2} V·m/N, which is 52% of the value of g_{33}. For the thick rod sample, the electrical condition holding E or D constant is correct at the center of the z-plane, but seems to be unclear near the edge of the sample. This change of electrical condition will be discussed later.

4.3.3 Measurement for Long Rod Sample

For the *long rod* sample illustrated in Fig. 4.1(c), the result of the electromechanical measurement is shown in Fig. 4.4. A similar optical measurement is also made only for the length-extensional mode near the lowest resonance frequency of the sample. In spite of the presence of the piezoelectric longitudinal effect, the resonance curve of S_3/E_3 can be plotted; thus, the value of d'_{33} can be measured. The S_3/E_3(max.), Q-value and d' are shown in Fig. 4.5. At position (a) $r \approx 0$, S_3/E_3(max.) = 1.78 ×10^{-8} m/V and Q = 46.9 give d'_{33} = 3.80×10^{-10} m/V, which is 92.6% of the value of d_{33}, and at position (b) $r \approx 0.9R$, S_3/E_3(max.) = 2.11×10^{-8} m/V and Q = 54.2 give d'_{33} = 3.89×10^{-10} m/V, which is 95.0% of the value of d_{33}. From the resonance curve of S_3/D_3, at position (a) $r \approx 0$, S_3/D_3(max.) = 4.87 V·m/N and Q = 241 give g'_{33} = 2.02×10^{-2} V·m/N, which is 91.8% of the value of g_{33}. The d' and g' are nearly in agreement with d and g, respectively, in the case of the long rod sample. However, at position (b) $r \approx 0.9R$, the resonance curve of S_3/D_3 cannot be plotted; therefore, the value of g'_{33} cannot be measured.

The electrical condition holding D or E constant depends on whether the depolarizing electric field $E = -P/\varepsilon_0$ exists or not. The depolarizing field depends on the form of the column and is represented as

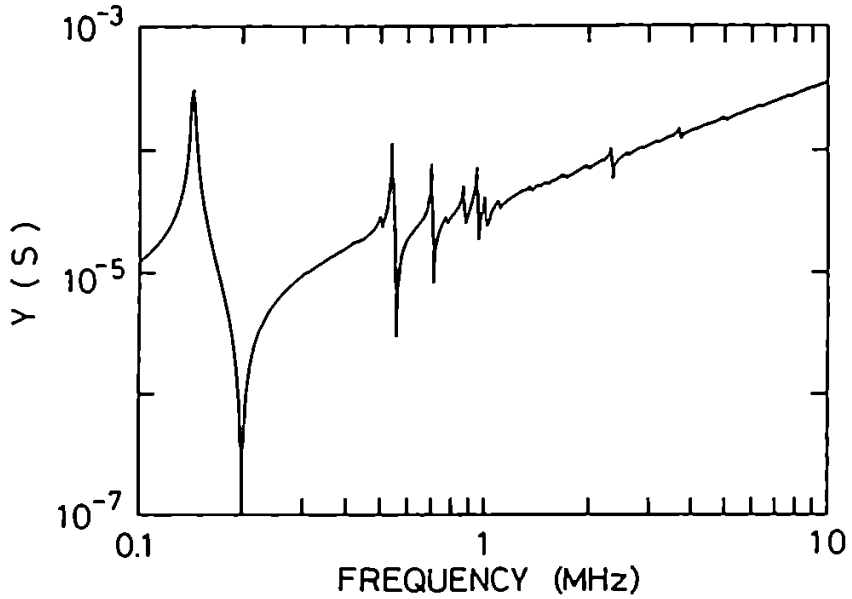

Fig. 4.4. Frequency characteristic of the admittance in the long rod sample illustrated in Fig. 4.1(c).

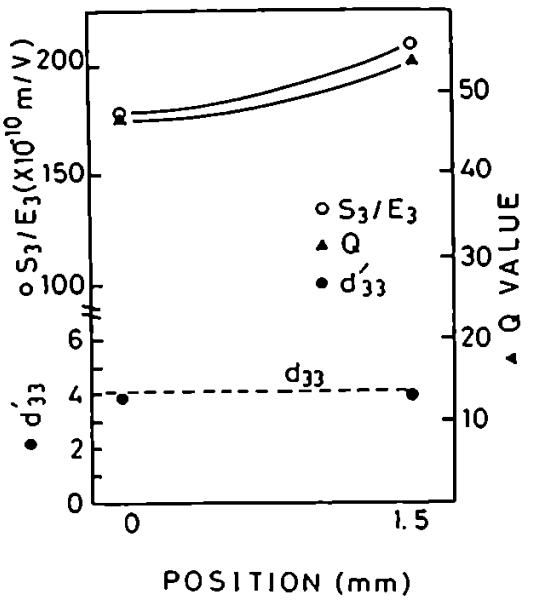

Fig. 4.5. Spatial distribution of the S_3/E_3(max.), Q-value and d'_{33} measured at the first resonance caused by the length-extensional mode in the long rod sample illustrated in Fig.4.1(c). The abscissa is distance from the center of the sample. A broken line shows the value of d_{33} given in Table 3.II.

$$E = -NP/\varepsilon_0 , \tag{4.3.1}$$

where

$N = 1$ for the infinitely thin disk,

$N = 0$ for the infinitely long rod,

and is expected to be different locally at position r when $0 < N < 1$. At the edge of the sample, the depolarizing field is expected to be smaller than that at the center of the sample. For the long rod sample illustrated in Fig. 4.1(c), the value of N in eq.(4.3.1) is much less than unity even at the center of the sample; therefore, the electrical condition holding D constant is not satisfied and the value of d' can be measured at this position. At the edge of the sample, the value of N is less than at the center of the sample and the electrical condition holding D constant is not correct so that the value of g' cannot be measured.

§4.4. Influence of Resonance Coupling

4.4.1 Concept of Resonance Coupling

The influence of resonance coupling on the measurement of d' and g' will now be discussed relative to the inductively coupled circuit illustrated in Fig. 4.6(a). The inductively coupled circuit is explained briefly below. The resonance angular frequencies ω_1 and ω_2 of the circuit with the coupling are given by

$$\omega_2^2, \omega_1^2 = \frac{\omega_{10}^2 + \omega_{20}^2 \pm \{ (\omega_{10}^2 + \omega_{20}^2)^2 - 4\omega_{10}^2\omega_{20}^2(1 - \eta^2) \}^{1/2}}{2(1 - \eta^2)}, \tag{4.4.1}$$

where

$$\omega_{10}^2 = (L_1C_1)^{-1} , \tag{4.4.2a}$$

$$\omega_{20}^2 = (L_2C_2)^{-1} , \tag{4.4.2b}$$

$$\eta^2 = M^2/(L_1L_2) , \tag{4.4.2c}$$

and the subscript 1 and 2 denote lower and higher frequencies, respectively; that is, $\omega_1^2 \le \omega_2^2$, and $\omega_{10}^2 \le \omega_{20}^2$. The quantity η is called a coupling coefficient in the resonance coupling.

An analogy between electrical and mechanical vibration is applied below. In the case of the columnar piezoelectric transducer, the resonance angular frequencies *without* the resonance coupling are given by

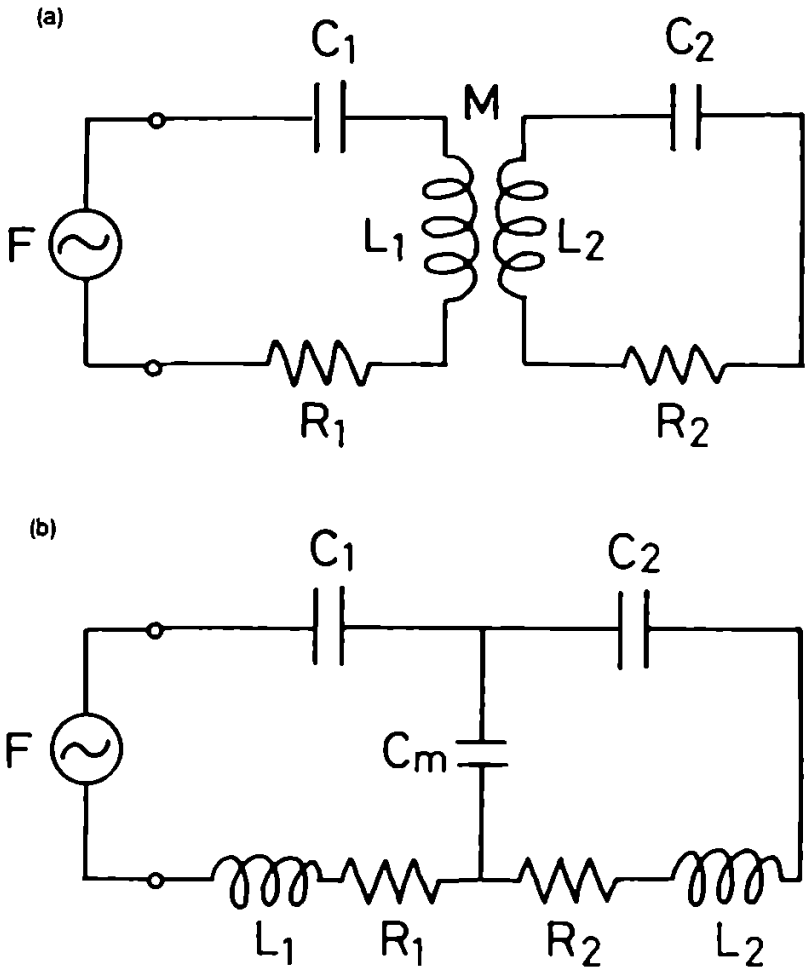

Fig. 4.6. (a) An inductively coupled circuit. Both two coupling circuits have ideal, independent and free vibration. (b) A capacitively coupled circuit.

$$\omega_{rL} = \frac{\pi}{(\rho s^{E}_{11})^{1/2} L}, \tag{4.4.3}$$

$$\omega_{rR} = \frac{\alpha_1}{\{ (1-\sigma^2)\, \rho s^{E}_{11} \}^{1/2} R}, \tag{4.4.4}$$

where ω_{rL} and ω_{rR} correspond to the resonance frequencies of the *length-extensional* mode in the *long rod* given by eqs. (4.2.10) to (4.2.12) and that of the *radial-extensional* mode in the *thin disk* given by eqs. (3.4.12) and (3.4.16b), respectively, and L and R are the length in the z-direction and the radius of the column, respectively. The material of the transducer is now assumed to be isotropic. For this reason, the elastic constant s_{11} is used instead of s_{33} in eq.(4.2.10). In addition, with regard to ω_{rL}, the elastic constant s^{E} is used instead of s^{D}. This means that the two resonances are studied based upon the same assumption that E is constant. The vibration of both the length-extensional mode in the long rod and the radial-extensional mode in the thin disk are *free* in both r- and z-directions. These two modes are coupled inductively as in Fig. 4.6(a), and the resonance angular frequencies ω_1 and ω_2 are given by

$$\omega_2^2, \omega_1^2 = \frac{\omega_{rL}^2 + \omega_{rR}^2 \pm \{ (\omega_{rL}^2 + \omega_{rR}^2)^2 - 4\omega_{rL}^2 \omega_{rR}^2 (1 - \eta^2) \}^{1/2}}{2(1 - \eta^2)}, \tag{4.4.5}$$

as in eq.(4.4.1).

The parameter p is defined by

$$p = \frac{\omega_{rR}}{\omega_{rL}} = \frac{L\alpha_1}{\pi R (1 - \sigma^2)^{1/2}}, \tag{4.4.6}$$

which is the ratio of the two angular frequencies *without* the coupling. The values of p of the samples illustrated in Figs. 4.1(a), 4.1(b) and 4.1(c) are 0.223, 1.09 and 4.37, respectively.

When $p << 1$, which is the case of the thin disk of $R >> L$, the two resonance angular frequencies are calculated according to eq.(4.4.5) as

$$\omega_1^2 = \omega_{rR}^2, \quad \text{and} \quad \omega_2^2 = \omega_{rL}^2 / (1 - \eta^2), \tag{4.4.7}$$

where the former corresponds to the resonance frequency of the radial-extensional mode in the thin disk, as expressed in eq.(4.4.4), and the latter corresponds to that of the thickness-extensional mode on the same sample, which is $(1 - \eta^2)^{-1}$ times as large as the value of ω_{rL}^2. The former vibration is free in both r- and z-directions. In contrast, the latter vibration is free in the z-direction but clamped in the r-direction. Multiplication by the factor $(1 - \eta^2)^{-1}$ represents the increase of the acoustic velocity due to the existence of the mechanical clamp.

When $p >> 1$, which is the case of the long rod of $R << L$, the two resonance angular frequen-

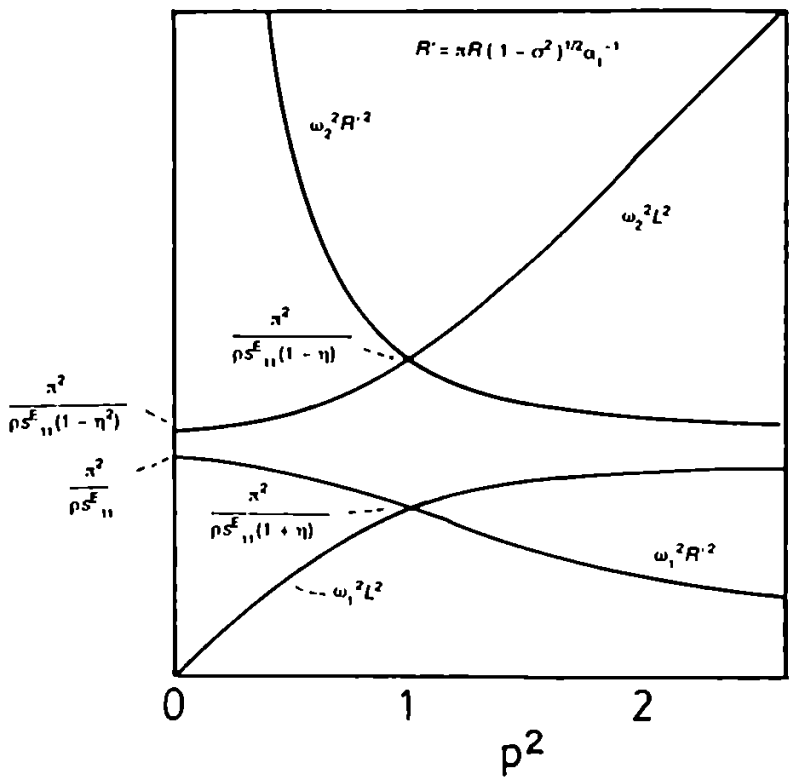

Fig. 4.7. Relationship between the resonance frequencies and the value of p.

cies are calculated as

$$\omega_1^2 = \omega_{rL}^2, \quad \text{and} \quad \omega_2^2 = \omega_{rR}^2 / (1 - \eta^2), \tag{4.4.8}$$

where the former corresponds to the resonance frequency of the length-extensional mode in the long rod, as expressed in eq.(4.4.3), and the latter corresponds to that of the radial-extensional mode on the same sample. The former vibration is free in two directions, while the latter vibration is free in the r-direction, but clamped in the z-direction.

The relationship between the resonance frequencies and the value of p is illustrated in Fig. 4.7. When $p = 1$, the two resonance angular frequencies are calculated as

$$\omega_1^2 = \omega_{rL}^2 / (1 + \eta), \quad \text{and} \quad \omega_2^2 = \omega_{rL}^2 / (1 - \eta), \quad \text{where} \quad \omega_{rL} = \omega_{rR}, \tag{4.4.9}$$

and the resonance coupling significantly influences the resonance frequencies.

The capacitively coupled circuit illustrated in Fig. 4.6(b) has resonance angular frequencies ω_1 and ω_2 which are given by

$$\omega_2^2, \omega_1^2 = \frac{\omega'^2_{10} + \omega'^2_{20} \pm \{ (\omega'^2_{10} + \omega'^2_{20})^2 - 4\omega'^2_{10}\omega'^2_{20}(1 - \eta^2) \}^{1/2}}{2}, \tag{4.4.10}$$

where

$$\omega'^2_{10} = (C_1 + C_m) / (L_1 C_1 C_m), \tag{4.4.11a}$$

$$\omega'^2_{20} = (C_2 + C_m) / (L_2 C_2 C_m), \tag{4.4.11b}$$

$$\eta^2 = C_1 C_2 / \{ (C_1 + C_m) (C_2 + C_m) \}, \tag{4.4.11c}$$

Comparing eqs.(4.4.1) and (4.4.10), the inductively and the capacitively coupled circuits are equivalent, conditioned upon

$$\omega'^2_{10} = \omega_{10}^2 / (1 - \eta^2), \tag{4.4.12a}$$

$$\omega'^2_{20} = \omega_{20}^2 / (1 - \eta^2). \tag{4.4.12b}$$

Multiplication by $(1 - \eta^2)^{-1}$ represents the effect of the mechanical clamp in one direction as discussed above; therefore, the two vibrational modes which are free in one direction, but clamped in the other direction are coupled in the capacitively coupled circuit. In the case of the columnar sample, the length mode for $L << R$ and the radius mode for $R << L$ are coupled. In the inductively coupled circuit, the length mode for $L >> R$ and the radius mode for $R >> L$ are also coupled.

With regard to the measurement of d' and g', the piezoelectric constants d and g must be measured in a stress-free state, considering the fundamental piezoelectric relations of d- and g-form. Hence, only the inductively coupled circuit is appropriate for the discussion regarding

the influence of the resonance coupling on the measurement of d' and g'.

The coupled coefficient η in the resonance coupling has the following relation to Poisson's ratio of material. The resonance angular frequency of the thickness-extensional mode in the thin disk, ω_{rT}, is given by

$$\omega_{rT}^2 = \frac{\pi^2 c^E_{11}}{\rho L^2} = \frac{\pi^2 (1-\sigma)}{\rho L^2 s^E_{11} (1+\sigma)(1-2\sigma)}, \tag{4.4.13}$$

based on holding E as constant and the material being isotropic. On the other hand, from eq.(4.4.3) and (4.4.7), ω_{rT} is given by

$$\omega_{rT}^2 = \frac{\pi^2}{\rho s^E_{11} (1-\eta^2) L^2}. \tag{4.4.14}$$

Comparing eq.(4.4.13) with eq.(4.4.14), we can obtain

$$\eta^2 = 2\sigma^2 / (1-\sigma). \tag{4.4.15}$$

Therefore, the coupling of the two vibrational modes is caused by the existence of Poisson's ratio.

4.4.2 Results of Calculation

The constants of the circuit illustrated in Fig. 4.6(a) can be determined by the methods described in this subsection. The angular frequencies ω_{rL} and ω_{rR} are determined for the present sample using eqs. (4.4.3) and (4.4.4), and smaller and larger ones are renamed ω_{10} and ω_{20}, respectively. The self-inductances L_1 and L_2 are given appropriately, for example, $L_1 = L_2 =$ 100 mH. The capacitances C_1 and C_2 are determined by eqs. (4.4.2a) and (4.4.2b), and the mutual inductance M is calculated using eqs. (4.4.2c) and (4.4.15). The resistance R_1 and R_2 are determined by

$$R_1 = (L_1 / C_1)^{1/2} / Q_1, \quad \text{and} \quad R_2 = (L_2 / C_2)^{1/2} / Q_2, \tag{4.4.16}$$

where Q_1 and Q_2, which are the Q-value of the respective modes, are given appropriately, for example, $Q_1 = 70$, and $Q_2 = 120$, which are based on the actual measurement.

The currents at a frequency ω_A in the left and right sides of Fig. 4.6(a), i_1 and i_2, are expressed as $i_1 = j\omega_A q_1$ and $i_2 = j\omega_A q_2$, respectively. The subscripts 1 and 2 denote lower and higher frequencies, respectively, as mentioned above, and the current i and the charge q correspond to the velocity and the displacement of vibration, respectively, because of the analogy between mechanical and electrical vibration. That is, q_1 and q_2 equal the average displacement of the reso-

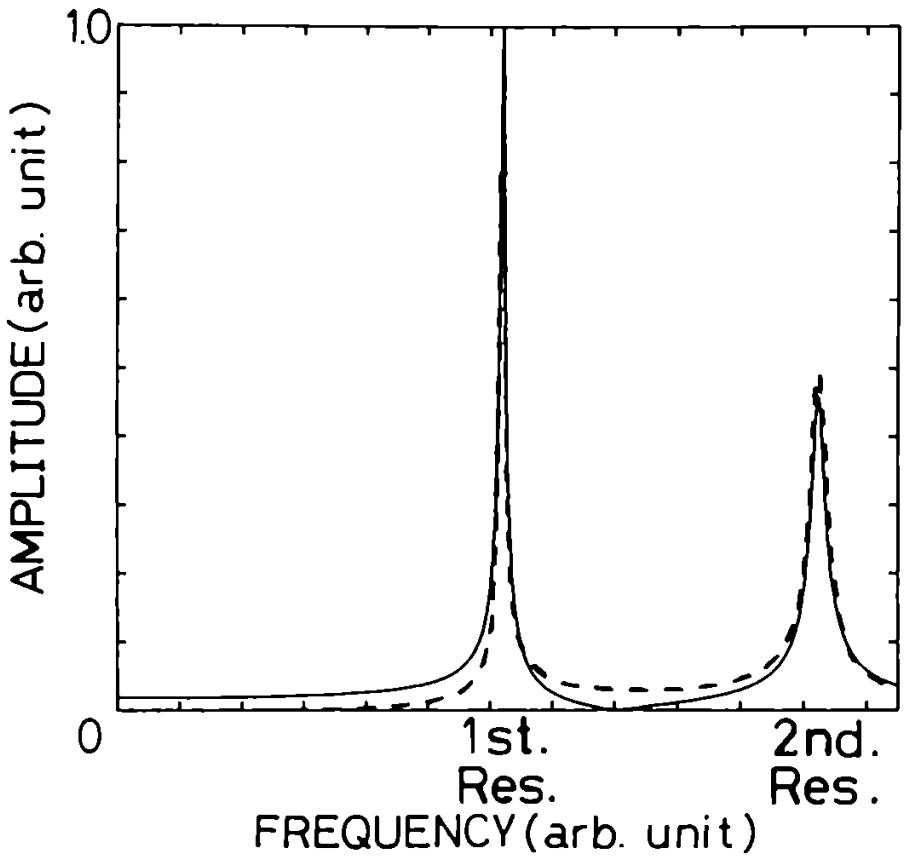

Fig. 4.8. Typical results of the calculation of the frequency characteristics of q_1 (solid line) and q_2 (dashed line).

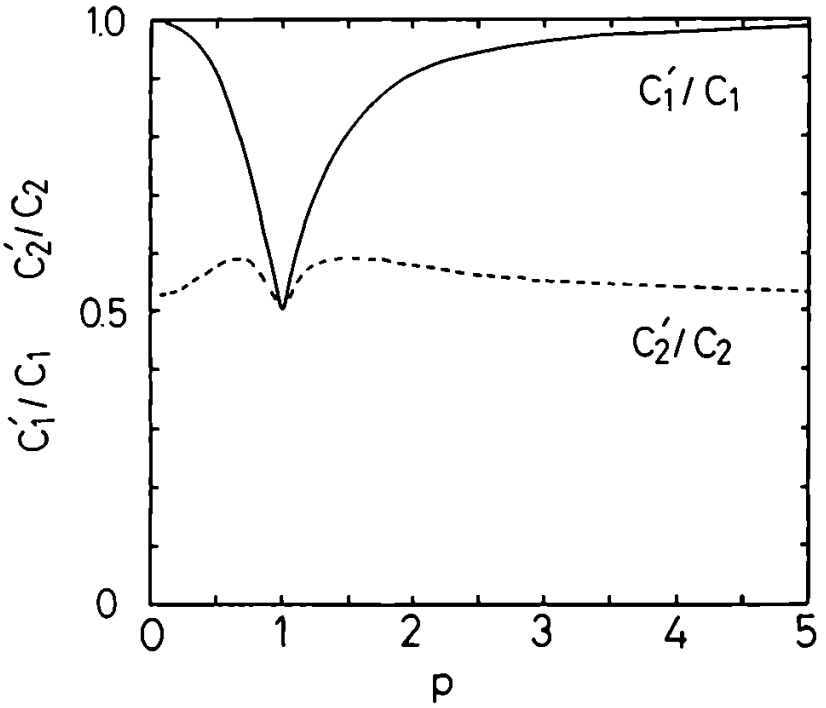

Fig. 4.9. The solid and the dashed lines show the dependence of C_1' / C_1 and C_2' / C_2 on the parameter p, respectively.

nator for the modes which have lower and higher resonance frequencies, respectively, as indicated in the discussion below. The charges q_1 and q_2 can be expressed as

$$q_1 = \frac{\omega^2{}_A L_2 - 1/C_2 - j\omega_A R_2}{(\det)} F , \tag{4.4.17}$$

$$q_2 = \frac{\omega_A{}^2 M}{(\det)} F , \tag{4.4.18}$$

where F is the driving force shown in Fig. 4.6(a), and

$$(\det) = \{ \omega_A{}^4 (M^2 - L_1 L_2) + \omega_A{}^2 (L_2/C_1 + L_1/C_2 + R_1 R_2) - 1/(C_1 C_2) \}$$
$$+ j \{ \omega_A{}^3 (R_1 L_2 + R_2 L_1) - \omega_A (R_1/C_2 + R_2/C_1) \} . \tag{4.4.19}$$

The frequency characteristics of q_1 and q_2 can be calculated for the samples. Typical results of the calculation of the frequency characteristics of q_1 and q_2 are shown in the solid and dashed lines in Fig. 4.8, respectively. Both resonance curves have two peaks. From the peak of q_1 at *lower* resonance frequency, the maximum value and the Q-value can be obtained, and the ratio of them is defined as $C'_1 F$; that is,

$$C'_1 F \equiv \frac{q_1 (\text{at } \omega_1)}{Q (\text{at } \omega_1)} , \tag{4.4.20}$$

similar to eqs. (3.7.7) and (3.7.9).

This $C'_1 F$ corresponds to the low frequency limit of q_1 *with* resonance coupling. The value of $C'_1 F$ is compared with that of $C_1 F$, which is the dc value of q_1 without coupling. From the peak of q_2 at the higher resonance frequency, the maximum value and the Q-value can be obtained, and their ratio is defined as $C'_2 F$; that is,

$$C'_2 F \equiv \frac{q_2 (\text{at } \omega_2)}{Q (\text{at } \omega_2)} . \tag{4.4.21}$$

A comparison is made between $C'_2 F$ and $C_2 F$. The solid and dashed lines in Fig. 4.9 show the dependence of C'_1 / C_1 and C'_2 / C_2 on parameter p, respectively. It is found that $C'_1 \approx C_1$ when $p^2 << 1$ or $p^2 >> 1$ and that $C'_1 < C_1$ when $p \approx 1$ in Fig. 4.9. This means that in the measurement of lower frequency resonance $d' \approx d$ and/or $g' \approx g$ for samples such as those in Fig. 4.1(a) or 4.1(c), with free vibration in both L- and R-directions, and that $d' < d$ and $g' < g$ for a sample such as that in Fig. 4.1(b). Moreover, it is found that $C'_2 < C_2$ regardless of the value of p. This means, in the measurement of higher frequency resonance, that $d' < d$ and $g' < g$ because of a mechanical clamp in one direction that results from the coupling.

4.4.3 *Comparison between Calculation and Experiment*

In this subsection, we shall compare the results of our calculations with our experiment's findings. The experimental results in §3.7 and §4.3 showed that the value of d' and g' derived by the optical method had local difference, that is, spatial distribution. On the other hand, the results of calculation in §4.4.2 were obtained using the electrical equivalent circuit which includes the characteristics of the sample as a whole. Therefore, for the comparison between the two results, the experimental results are averaged spatially by

$$\langle d' \rangle = \int d'(r)\, \mathrm{d}r / R, \tag{4.4.22}$$

$$\langle g' \rangle = \int g'(r)\, 2\pi r \mathrm{d}r / (\pi R^2), \tag{4.4.23}$$

where the notation "< >" indicates the spatial average, $d'(r)$ and $g'(r)$ are the function of position r, and assumed to be quadratic, because $d'(r)$ and $g'(r)$ are symmetric on $r = 0$, and $\mathrm{d}d'(r) / \mathrm{d}r$ and $\mathrm{d}g'(r) / \mathrm{d}r$ are zero at $r = 0$. Since the electric field E and the electric flux density D are the intensive and the extensive variables, and these correspond to "tension" and "flow", respectively, the integration of $d'(r)$ and $g'(r)$ which are calculated from S / E and S / D is represented as eqs. (4.4.22) and (4.4.23), respectively.

In the case of the *thin* disk, illustrated in Fig. 4.1(a), whose parameter p is 0.223, the results of the calculation are

$$C'_1 / C_1 = 0.985, \tag{4.4.24}$$

$$C'_2 / C_2 = 0.539. \tag{4.4.25}$$

On the other hand, the averaging of the experimental results, which were shown in Figs. 3.10 and 3.17, using eqs. (4.4.22) and (4.4.23) gives

$$\langle d'_{33} \rangle / d_{33} = 0.883, \tag{4.4.26}$$

$$\langle g'_{33} \rangle / g_{33} = 0.900. \tag{4.4.27}$$

In addition, the value of d'_{31} was

$$\langle d'_{31} \rangle / d_{31} = d'_{31} / d_{31} = 1.01, \tag{4.4.28}$$

as measured in §3.7.1. The measurement of d'_{33} and d'_{31} was performed at the radial-extensional mode, and that of g'_{33} at the thickness-extensional mode. The resonance frequency of the

former is lower than that of the latter. Therefore, $\langle d' \rangle / d$ and $\langle g' \rangle / g$ correspond to C'_1 / C_1 and C'_2 / C_2, respectively. We find that both C'_1 / C_1 and $\langle d' \rangle / d$ are almost in agreement with unity in eqs. (4.4.24), (4.4.26) and (4.4.28) and that the resonance coupling hardly influences the results of $\langle d' \rangle$; that is to say, the evaluation of the *material constants* can be performed with little influence from the *vibrational mode*. On the other hand, the value of $\langle g'_{33} \rangle$ is not in agreement with that of C'_2 / C_2. The reason can be explained as follows. Though the calculation of C'_2 / C_2 is based on all the characteristics of the sample, the measurement of g' is performed only in the z-direction. Since the amplitude of the vibration in this mode is very small in the r-direction, the average of g' not only on the z-plane but also in the r-direction must be smaller than the value given in eq.(4.4.27). Therefore, the average of g' from the entire sample must approximate the value of C'_2 / C_2.

In the case of the *thick rod* sample, illustrated in Fig. 4.1(b), whose parameter p is 1.086, the results of the calculation are

$$C'_1 / C_1 = 0.578, \tag{4.4.29}$$

$$C'_2 / C_2 = 0.537. \tag{4.4.30}$$

The averaging of the experimental results, which were shown in Figs. 4.3(a) and 4.3(b), gives

$$\langle g'_{33} \rangle / g_{33} = 0.427, \tag{4.4.31}$$

$$\langle d'_{33} \rangle / d_{33} = 0.106, \tag{4.4.32}$$

respectively. The resonance frequency of the mode which gives d'_{33} in eq.(4.4.32) is higher than that of the mode which gives g'_{33} in eq.(4.4.31); therefore, $\langle g' \rangle / g$ and $\langle d' \rangle / d$ correspond to C'_1 / C_1 and C'_2 / C_2, respectively. In both cases, the measurement of g' and d' is influenced strongly by resonance coupling, and the evaluation of the *material constants* cannot be performed. The considerable difference of the values in eq.(4.4.30) and eq.(4.4.32) stems from the same cause as the difference in values of g'_{33} / g_{33} and C'_2 / C_2 in the thin disk sample. The mode in the thick rod used for the calculation of d'_{33} is radial-extensional, and the amplitude in the r-direction is large at the resonance, but the mechanical clamp exists in the z-direction, because the resonance frequency of this mode is higher than that of the length-extensional mode in the z-direction. The average of d' not only in the z-direction but also in the r-direction must be larger than the value given in eq.(4.4.32).

In the case of the *long rod* sample, illustrated in Fig. 4.1(c), whose parameter p is 4.375, the results of the calculation are

$$C'_1 / C_1 = 0.987, \tag{4.4.33}$$

$$C'_2 / C_2 = 0.540. \tag{4.4.34}$$

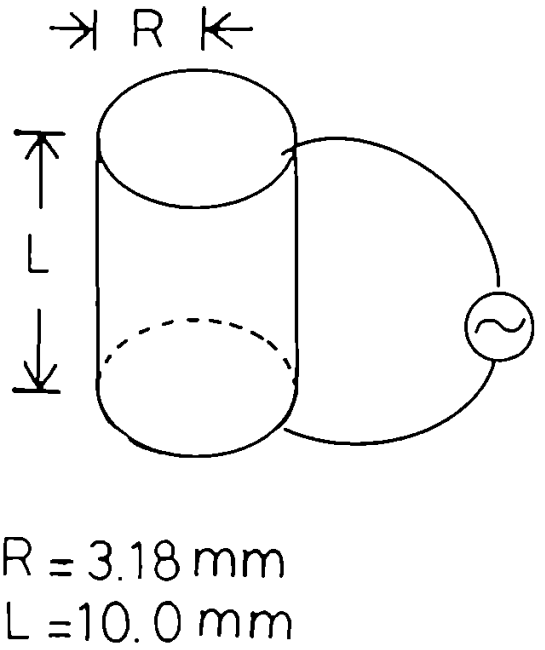

Fig. 4.10. Piezoelectric circular sample for the optical measurement of the acoustic velocity in the radial-extensional mode.

and the experimental results are

$$\langle d'_{33} \rangle / d_{33} = 0.938, \tag{4.4.35}$$

which is based on the results in Fig. 4.5, and

$$g'_{33} / g_{33} = 0.918, \tag{4.4.36}$$

at the center of the sample, $r = 0$. We can consider that the value of d' / d and g' / g is almost unity and in agreement with that of C'_1 / C_1. Therefore, the evaluation of the material constants can be performed in the length-extensional mode in the long rod sample without any effects from resonance coupling, except that this measurement is influenced by the decrease of the depolarizing field, and therefore, by the change of the electrical condition of piezoelectric vibration holding that $E = 0$ or $D = 0$.

§4.5. Measurement of Acoustic Velocity for Forms Other than Thin Disk

In §3.8, it was explained that the phase of acoustic vibration was measured optically, and the methods of measuring acoustic velocity and Poisson's ratio were applied to the disk sample illustrated in Fig. 3.1 (Fig. 4.1(a)). Application of these methods to circular samples whose forms are not thin disk is discussed in this section. Since eq.(3.4.11), which expresses the displacement of radial-extensional vibration, is also valid for forms other than thin disk, eq.(3.8.1) can be used for the calculation of v. However, the calculation of σ by using the value of v is impossible, because eqs.(3.4.12), (3.4.15) and (3.4.17) are not valid for forms other than thin disk. Moreover, phase shift frequency determined by eq.(3.8.1) moves to the higher range where many confusing resonances can exist. Accordingly, this measurement is more difficult than thin disk measurement. However, the phase shift determined by eq.(3.8.1) can be distinguished from the phase shifts due to resonances, because 1) when the light is incident in the z-direction, the phase shift of eq.(3.8.1) cannot occur at the same frequency as it can at position $r = R$ when the light is incident in the r-direction, and 2) when some capacitance is connected in series with the piezoelectric sample, the resonance frequency can change. As a result, the phase shift due to resonance can change, but the phase shift of eq.(3.8.1) is not so likely to change.

With samples illustrated in Figs. 4.10 and 4.1(c), the measurement of v is performed. The sample illustrated in Fig. 4.10 is the same as the samples illustrated in Figs.4.1 (a), 4.1(b) and 4.1(c), except for the shape. For this sample, the frequency of the phase shift determined by eq.(3.8.1) is observed to be 0.604 MHz, which gives

$$v = 3.15 \times 10^3 \text{ m/s}.$$

For the sample illustrated in Fig. 4.1(c), the frequency observed was 1.597 MHz, which gives

$v = 4.01 \times 10^3$ m/s.

The mechanical clamp increases the acoustic velocity.

§4.6 Summary

The optical measurement method described in the previous chapter was applied to circular samples whose forms were not of the thin disk type.

For the thick rod sample, d' and g', the optically measured values corresponding to the material constants d and g, respectively, were much smaller than the values of the material constants. On the other hand, for the long rod sample, they were nearly in agreement with the material constants. However, the electrical condition of the piezoelectric vibration was not satisfied, especially at the edge of the sample.

The theory of resonance coupling was applied to the problem of measuring d' and g'. It was found that the thin disk and long rod samples were appropriate for the measurement of the material constants; that is, $d' \approx d$ and $g' \approx g$, when the lowest resonance was used for the measurement.

The acoustic velocity of the radial-extensional mode was also measured optically; however, Poisson's ratio could not be measured for samples whose forms were not of the thin disk type.

References

1) M.Ohki, N.Shima and T.Shiosaki: Jpn.J.Appl.Phys., **31**(1992) 3272.

2) M.Ohki, N.Shima and T.Shiosaki: IEICE Tech.Rep., US91-79,EA91-92 (1992.1.28)

3) T.Tanaka: *Chitansanbariumu to Sono Ouyou* (Barium Titanate and Its Application) (Ohmusha,Tokyo,1955) §3.5 [in Japanese] .

Chapter 5
Influence of Photorefractive Effect on Piezoelectric Vibration

§5.1. Introduction

In previous chapters we have investigated the new measurement methods of the piezoelectric transducer based upon the interaction between the acoustic wave in and optical wave incident on the sample. From a crystallographic point of view, the crystal with the piezoelectric effect is possible to exhibit the Pockels effect—— an electrooptic effect of the first order, in which the refractive index of the crystal is changed by electric field. Transparent or semitransparent piezoelectric crystals in which optical waves can propagate are used for the electrooptic applications. Another objective of this thesis is to discover and examine a new phenomenon induced by coherent optical waves in a semitransparent piezoelectric transducer. We pay attention to the photorefractive (PR) effect for this purpose.

The PR effect is the phenomenon in which the refractive index of an electrooptic crystal varies according to the incidence of visible rays.[1] Interference of two coherent optical waves yields fringes, that is, the space-periodic variation of the intensity of the light, which cause excitation of carriers. The excited carriers are transferred in the crystal by diffusion and drift, forming a space-periodic charge distribution. The variation of the refractive index is caused by an internal electric field created from the charge distribution through the Pockels effect. In this way, grating of the refractive index is caused in the crystal. The diffraction and the apparent amplification of light can occur in the crystal due to this refractive grating.

Applications of the effect to holography and optical processing have been developed in recent years.[2),3)] An application to acoustics has also been developed by which an acoustic wave is filtered by the periodic variation of the acoustic velocity that is caused by the periodic internal electric field.[4)]

In this chapter, we describe the influence of the PR effect on acoustic vibration, especially piezoelectric vibration, from a new point of view. A piezoelectric resonator made of $LiNbO_3$:Fe with PR grating is examined as the sample. We view electromechanical characteristics near the resonance frequencies of the modes of vibration.[5)] The experimental results are explained by a new physical model.

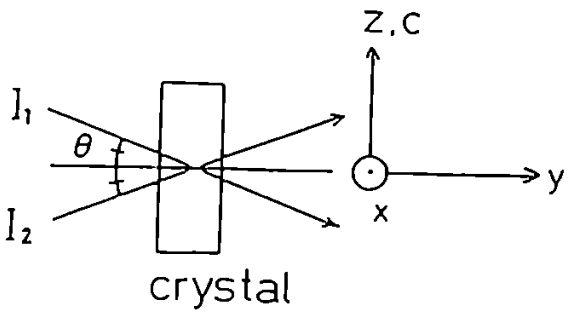

Fig. 5.1. Two optical waves mixed in the crystal.

Table 5.I. Elastic and piezoelectric (electrooptic) and dielectric tensors in crystallographic point group of *3m*.

Elastic

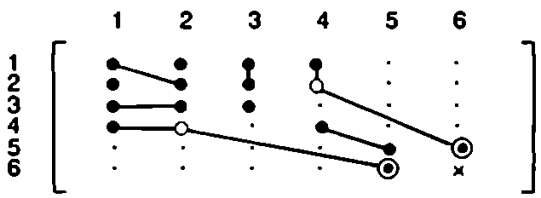

The notation "x" means $(c_{11} - c_{12}) / 2$ or $2(s_{11} - s_{12})$, and $c_{ij} = c_{ji}$, $s_{ij} = s_{ji}$. The " ○—● " means the converse algebraic sign and the same absolute value. The "◎" has the value of s_{ij} which is twice as large as that of "●" connected by the line, and has the same value of c_{ij} as that of "●" connected by the line.

Piezoelectric (Electrooptic)

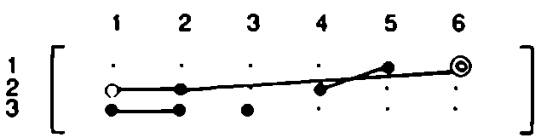

The "◎" has the value of d_{ij} which is (-2) times as large as that of "●" connected by the line, and has the value of e_{ij} which is (-1) times as large as that of "●" connected by the line.

Table 5.I. (cont'd)

Dielectric

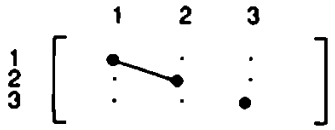

Table 5.II. Main material constants of $LiNbO_3$

$\varepsilon^S_{11}/\varepsilon_0$	44.3	c^E_{11} (10^{11} N/m^2)	2.030
$\varepsilon^S_{33}/\varepsilon_0$	27.9	c^E_{12} (10^{11} N/m^2)	0.573
$\varepsilon^T_{11}/\varepsilon_0$	85.2	c^E_{13} (10^{11} N/m^2)	0.752
$\varepsilon^S_{33}/\varepsilon_0$	28.7	c^E_{14} (10^{11} N/m^2)	0.085
n_O	2.3356	c^E_{33} (10^{11} N/m^2)	2.424
n_e	2.2448	c^E_{44} (10^{11} N/m^2)	0.595
e_{15} (C/m^2)	3.76	c^E_{66} (10^{11} N/m^2)	0.728
e_{22} (C/m^2)	2.43	s^E_{11} (10^{-12} m^2/N)	5.831
e_{31} (C/m^2)	0.23	s^E_{12} (10^{-12} m^2/N)	-1.150
e_{33} (C/m^2)	1.33	s^E_{13} (10^{-12} m^2/N)	-1.452
d_{15} (10^{-11} C/N)	6.92	s^E_{14} (10^{-12} m^2/N)	-1.000
d_{22} (10^{-11} C/N)	2.08	s^E_{33} (10^{-12} m^2/N)	5.026
d_{31} (10^{-11} C/N)	-0.085	s^E_{44} (10^{-12} m^2/N)	17.10
d_{33} (10^{-11} C/N)	0.60	s^E_{66} (10^{-12} m^2/N)	13.96
Pyroelectricity (10^{-5} C/(K·m^2))		4	
Spontaneous Polarization (C/m^2)		0.71	

§5.2. Formation of Photorefractive Grating

5.2.1 Photorefractive Effect

Two optical waves are incident and are mixed in the crystal, as illustrated in Fig. 5.1. The electric field of two optical waves mixed in the crystal at position $r = (x, y, z)$ is expressed as

$$E(r) = A_1(r)\cos(k_1 \cdot r) + A_2(r)\cos(k_2 \cdot r), \tag{5.2.1}$$

where A_i and k_i are the amplitude and the wavenumber vector of the light field before mixing, respectively. If the two optical waves are coherent, they can interfere and the space-periodic variation of the intensity, which is the time average of the square of the two fields, can be caused in the crystal as

$$I(r) = |A_1(r)|^2 + |A_2(r)|^2 + 2\gamma\, Re\{A_1(r)A_2^*(r)\}\cos(K \cdot r), \tag{5.2.2}$$

where the visibility $\gamma \approx 1$, the polarization states of the two waves are assumed to be the same, and the wavenumber vector K of the fringes in the crystal is given by

$$K = k_1 - k_2, \quad (|K| = 2\pi / \Lambda) \tag{5.2.3}$$

where Λ is the wavelength of the fringes in the crystal. The incident angle θ_{in} inside the crystal has relation to that outside the crystal, θ in Fig. 5.1, as

$$\sin\theta = n_C \sin\theta_{in}, \tag{5.2.4}$$

Snell's law. The relation between Λ and the incident angle θ_{in} inside the crystal is given by

$$\Lambda = \frac{\lambda / n_C}{2\sin\theta_{in}}, \tag{5.2.5}$$

where λ and n_C are the wavelength of the light in a vacuum and the refractive index of the light, respectively. The value of n_C depends on λ and the polarization state of the light. The intensity-modulation index m is defined as

$$m = \frac{2\,Re\{A_1(r)A_2^*(r)\}}{|A_1|^2 + |A_2|^2} = \frac{2(I_1 I_2)^{1/2}}{I_1 + I_2}, \tag{5.2.6}$$

where I_i is the intensity of the light before mixing.

The photorefractive (PR) effect occurs readily in an electrooptic crystal doped with impurity atoms. In this study, $LiNbO_3$:Fe, lithium niobate doped with 0.09 mol% Fe, is used as a sample. The crystallographic point group of the material is *3m*, whose forms of elastic, piezoelectric or electrooptic, and dielectric tensors are shown in Table 5.I. The main material constants are shown in Table 5.II. The $LiNbO_3$:Fe is appropriate for storing the PR grating recorded optical-

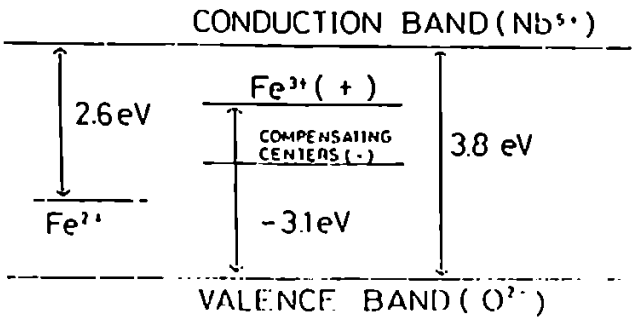

Fig. 5.2. Band structure of $LiNbO_3$:Fe.

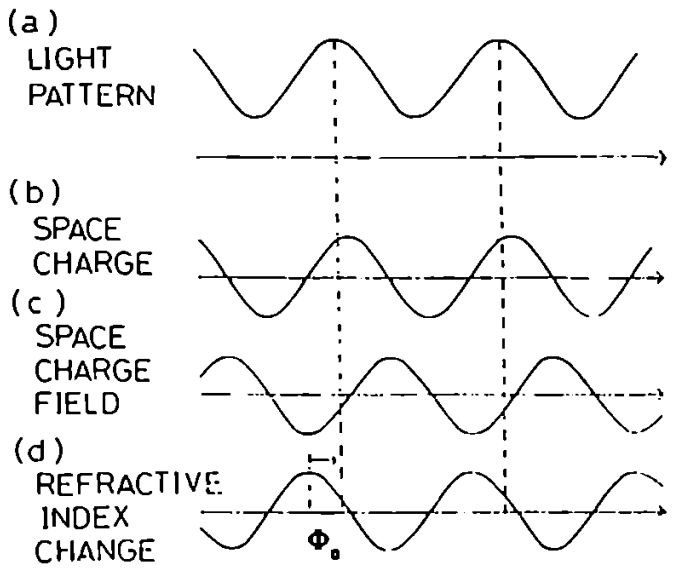

Fig. 5.3. Formation of the photorefractive grating. (a) Space-periodic light intensity. (b) Space-periodic charge distribution. (c) Space-periodic electric field E_{sc}. (d) The variation of the refractive index Δn_c which has the phase difference Φ_n from the intensity pattern.

ly, and has excellent piezoelectricity.

The formation of the PR grating is explained below.[6] The band structure of $LiNbO_3$:Fe is illustrated in Fig. 5.2.

1) Electrons are excited at points of higher light intensity, from the impurity level of Fe^{2+} ion to the conduction band. The light pattern is illustrated in Fig. 5.3(a). The density concentration of Fe^{2+} and the electrons in the conduction band are represented by $N_D - N_D^+$ and N_e^-, respectively. The Fe^{2+} ion is oxidized and becomes a Fe^{3+} ion after excitation.

2) The electrons in the conduction band are transferred to a region of lower intensity due to drift and diffusion. The current density J of the electrons is

$$J = \underset{\text{drift}}{\mu e N_e^- E_{in}} + \underset{\text{diffusion}}{eD\nabla N_e^-} = \mu e N_e^- E_{in} + k_B T \mu \nabla N_e^- , \tag{5.2.7}$$

where μ [$m^2/(V \cdot s)$], e [C], E_{in} [V/m] D [m^2/s], k_B [J/K] and T [K] are the mobility, the elementary electric charge, the dc or low frequency electric field in the crystal, the diffusion constant, the Boltzmann constant, and the absolute temperature, respectively. In eq.(5.2.7), the Einstein relation $eD = k_B T\mu$ is used. The electrons are captured by the impurity level of Fe^{3+}, the density concentration of which is represented by N_D^+. The Fe^{3+} ion is reduced and becomes a Fe^{2+} ion after the recombination. The rate equation for the density of the donor atom, Fe, is expressed as

$$\partial N_D^+ / \partial t = \underset{\text{excitation}}{(\alpha_D / h\nu)\, I(r)\, (N_D - N_D^+)} - \underset{\text{recombination}}{\gamma_D N_e^- N_D^+} , \tag{5.2.8}$$

where α_D, γ_D, h, ν are the absorption cross section of Fe^{2+}, the recombination coefficient of an electron with Fe^{3+}, Planck's constant, and the frequency of the light, respectively. The current continuity relation is

$$\nabla \cdot J = -e\, \partial (N_D^+ - N_e^-) / \partial t. \tag{5.2.9}$$

3) The charge distribution forms the electric field in the crystal, E_{in}, according to Poisson's equation as

$$\nabla \cdot E_{in} = e\,(N_D^+ - N_e^- - N_A^-) / \varepsilon , \tag{5.2.10}$$

where N_A^- is the density concentration of acceptor atoms which are occupied by electrons at all times to ensure the balance of charge in the crystal; that is,

$$e\,(\langle N_D^+ \rangle - \langle N_e^- \rangle - N_A^-) = 0 , \tag{5.2.11}$$

where the notation $\langle\ \rangle$ means the spatial average in the direction of K vector. E_{in}, N_D^+ and N_e^- in the crystal can be expressed as

$$E_{in} = E_0 + E_{SC} \exp(jK \cdot r) + \text{c.c.} , \tag{5.2.12a}$$

$$N_D^+ = N_{D0}^+ + N_{D1}^+ \exp(jK\cdot r) + \text{c.c.}, \tag{5.2.12b}$$

$$N_e^- = N_{e0}^- + N_{e1}^+ \exp(jK\cdot r) + \text{c.c.}, \tag{5.2.12c}$$

The distributions of the charge density $N_D^+ - N_e - N_A^-$ and the electric field E_{SC} are illustrated in Figs. 5.3(b) and 5.3(c), respectively.

4) The variation of the refractive index due to Pockels effect can be expressed as

$$\Delta(n_C^{-2})_{ij} = r_{ijk} E_{sc\,k}, \tag{5.2.13}$$

where r_{ijk} is the electrooptic constant. From eq.(5.2.13), we can derive

$$\Delta n_C \equiv -(1/2)\, n_{C0}^3\, r_{eff}\, E_{SC}, \tag{5.2.14}$$

where r_{eff} depends on the crystal orientation, the direction of E_{SC} and the polarization state of incident light. The space-periodic variation of the refractive index is illustrated in Fig. 5.3(d). The Δn_C has phase difference Φ_n from the light pattern as

$$n_C = n_{C0} + |\Delta n_C| \cos(K\cdot r + \Phi_n). \tag{5.2.15}$$

The Φ_n is an important factor for the diffraction and apparent amplification of the light.

The expression for E_{SC} can be obtained by using eqs. (5.2.7) to (5.2.11) with the Fourier expansion up to the first order, as described in eqs. (5.2.12a) to (5.2.12c). The steady-state response of E_{SC} can be expressed as[6]

$$E_{SC} = -j\, m \frac{E_N (E_0 + jE_D)}{E_0 + j(E_N + E_D)}, \tag{5.2.16}$$

where

$$E_N = eN_A^- / (\varepsilon K) \propto \Lambda, \tag{5.2.17}$$

$$E_D = k_B T K / e \propto \Lambda^{-1}, \tag{5.2.18}$$

and the factor " $-j$" in eq.(5.2.16) shows a spatial $+\pi/2$ or $-\pi/2$ shift of the Δn_C with respect to the light intensity pattern; that is, $\Phi_n = +\pi/2$ or $-\pi/2$ in eqs. (5.2.14) and (5.2.15), according to $r_{eff} > 0$ or $r_{eff} < 0$. E_{SC} is proportional not to the total intensity but to the modulation index m. When $E_0 = 0$, E_{SC} is given by

$$E_{SC} = -j\, E_N E_D / (E_N + E_D), \tag{5.2.19}$$

which shows that the smaller field of E_N and E_D is effective. E_N is the maximum space charge field obtained by the integration of the maximum available charge distribution $eN_A^-\cos(K\cdot r)$, which corresponds to the full separation of the charges. If $E_D < E_N$, the field is determined by E_D, which corresponds to the situation in eq.(5.2.7) in which $J = 0$; that is, the current density is

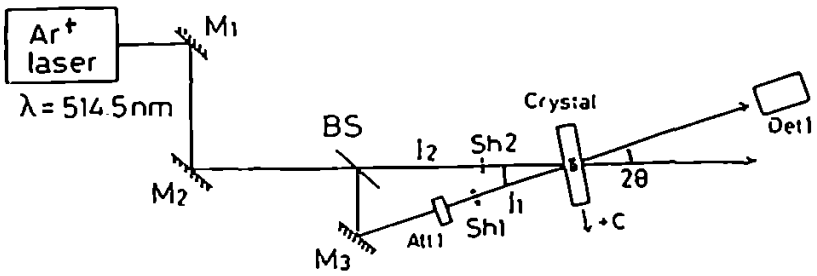

Fig. 5.4. Experimental arrangement to form the PR grating in the $LiNbO_3$:Fe crystal.

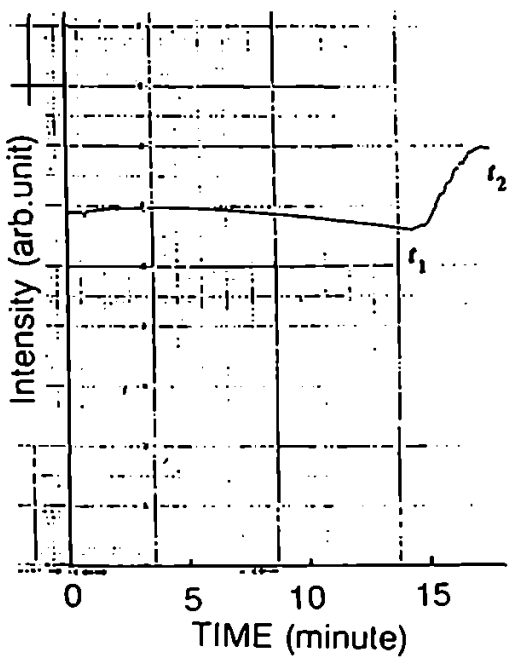

Fig. 5.5. Typical time variation of the intensity I_1 detected at the photo-diode.

not enough to reach the full separation of the charges. If E_0 becomes infinitely large, E_{SC} becomes $-jmE_N$. Therefore, the addition of the external field E_0 can promote the separation of the charges.

The diffraction and the apparent amplification of the two waves incident in the crystal can be derived as follows. Substitution of the electric field of the light, E, expressed in eq.(5.2.1) into the wave equation,

$$\nabla^2 E + \omega_C^2 \mu_0 \varepsilon(r) E = 0 , \tag{5.2.20}$$

where

$$\varepsilon(r) = \varepsilon_0 n_C^2(r) \approx \varepsilon_0 \{ n_{C0} + 2 n_{C0} \mid \Delta n_C \mid \cos(K \cdot r + \Phi_n) \} , \tag{5.2.21}$$

yields to the coupling equations between A_1 and A_2 as

$$\cos\theta_{in}\, dA_1 / dy = -(\alpha / 2) A_1 - j\pi \mid \Delta n_C \mid \lambda^{-1} \exp(j\Phi_n) A_2 , \tag{5.2.22}$$

$$\cos\theta_{in}\, dA_2 / dy = -(\alpha / 2) A_2 - j\pi \mid \Delta n_C \mid \lambda^{-1} \exp(-j\Phi_n) A_1 , \tag{5.2.23}$$

where the approximation

$$d^2 A_i / dr^2 << k\, dA_i / dr , \tag{5.2.24}$$

is used, and the transformation of coordinates

$$y = r \cos\theta_{in} , \tag{5.2.25}$$

is performed, considering the experimental configuration in Fig. 5.1. The first terms on the right sides of eqs. (5.2.22) and (5.2.23) represent the loss of amplitude in the crystal, and the second terms represent the diffraction of another wave. From eqs. (5.2.22) and (5.2.23), we obtain

$$\cos\theta_{in}\, dI_1 / dy = -\alpha I_1 + 2\pi \mid \Delta n_C \mid \lambda^{-1} (I_1 I_2)^{1/2} \sin(\Phi_n) , \tag{5.2.26}$$

$$\cos\theta_{in}\, dI_2 / dy = -\alpha I_2 - 2\pi \mid \Delta n_C \mid \lambda^{-1} (I_1 I_2)^{1/2} \sin(\Phi_n) , \tag{5.2.27}$$

where eq.(5.2.26) results from the sum of the respective sides of eq.(5.2.22) times A_1^* and those of the complex conjugate of eq.(5.2.22) times A_1, and eq.(5.2.27) is obtained by a similar procedure. When $\Phi_n = +\pi/2$, intensity I_1 is most amplified due to the energy transfer from I_2 to I_1. When $\Phi_n = -\pi/2$, the situation becomes converse.

5.2.2 Experimental System to Form PR Grating

The experimental system used for forming the PR grating in the $LiNbO_3$:Fe crystal is shown in Fig. 5.4. The Ar^+ laser with wavelength $\lambda = 514.5$ nm is used as a light source. Specifications of this laser are summarized in Table 5.III. The light is split into two parts I_1 and I_2, by a beam splitter (BS). I_1 can be attenuated by the attenuator Att1. I_1 and I_2 can be shut out by the

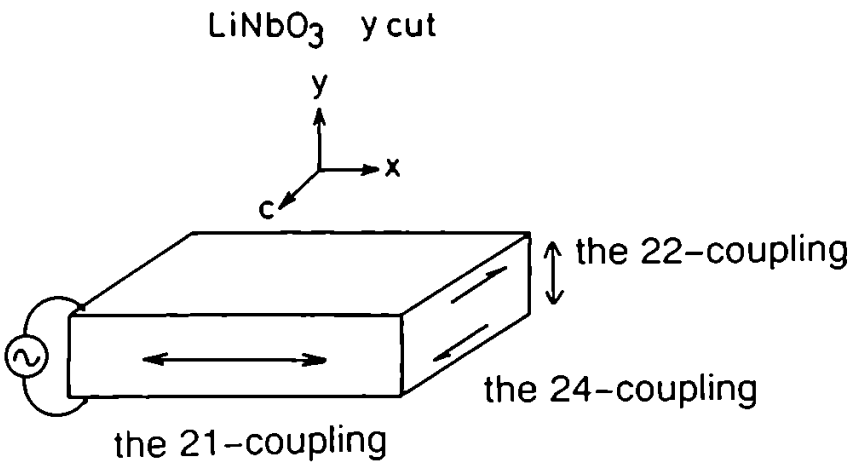

Fig. 5.6. Three vibrational modes in the *y*-cut plate of $LiNbO_3$.

Table 5.III. Specifications of the laser.

NEC GLG3200
wavelength : 514.5 nm, power : 800 mW
mode : TEM_{00}, linearly polarized
stability : 0.5%/h
beam diameter : 1.5 mm

Table 5.IV. Specifications of $LiNbO_3$ y-cut plates for the measurement.

Fe 0.09 mol% doped, thickness : 1.51 mm
polarization of light // *x*-axis, PR grating // *c*-axis
shapes of y-plane : #1 pentagonal ($Q \approx 4000$), #2 rectangular ($Q \approx 20000$), #3-5 irregular ($Q < 1000$)

shutters Sh1 and Sh2, respectively. The two lights are incident in the crystal, and the amplified or attenuated intensity of I_1 can be detected by the photodiode Det1.

The y-cut plates of $LiNbO_3$:Fe are used as the samples. The light is incident on the y-plane of the sample. The c-axis of the crystal is arranged as illustrated in Fig. 5.4. In this case, the algebraic sign of $\sin(\Phi_n)$ in eqs. (5.2.26) and (5.2.27) is positive; therefore, I_1 can be amplified, and I_2 is attenuated in the crystal. The polarization of the light is now set to be the s-polarization; that is, the electric field is in the x-direction in Fig. 5.4. Specifications of the y-cut plates for the experiments are shown in Table 5.IV.

Figure 5.5 shows the typical time variation of I_1 detected at the photodiode Det1 in Fig. 5.4. The ratio of I_1 to I_2 before entering into the crystal is 1 : 1, and the power is 550 mW/cm^2. At a time $t = 0$, the shutter Sh1 is opened and Sh2 is still closed. Only the incidence of I_1 can eliminate the residuary PR grating in the crystal. At $t = t_1$ (about 14.5 min.), the shutter Sh2 is also opened, the two waves are mixed in the crystal, and I_1 is amplified. At $t = t_2$ (about 17 min.), the increase of I_1, dI_1 / dt, reaches zero, the PR grating can be presumed formed in the crystal, and the shutters are closed.

The PR grating is formed in the c- (z-) direction in the crystal. The period of the PR grating Λ can be changed by changing the angle 2θ in Fig. 5.4, following eqs. (5.2.4) and (5.2.5). Since the polarization of the light is in the x-direction in the crystal, the refractive index n_c in eqs. (5.2.4) and (5.2.5) is n_O ($= (\varepsilon_{11} / \varepsilon_0)^{1/2}$); that is, the two waves are ordinary waves. The diameter of the light beam is about 1.5 mm, which partially forms the PR grating in the small volume in the crystal. The beam diameter can be expanded to about 20 mm by setting the beam expander within the experimental system, which forms a large volume of PR grating in the crystal.

§5.3. Decrease of Q and Generation of Nonlinear Acoustic Vibration due to PR grating

5.3.1 Experimental Method

After the PR grating is written, Au electrodes are deposited on the y-planes, and the frequency characteristics of admittance are measured near the resonance frequencies of the modes in the y-cut plate of $LiNbO_3$:Fe using the electromechanical methods described in §3.6. The piezoelectric vibration of the plate has the following mn modes where m denotes the direction of electric field to drive the vibration and n denotes the strain S_n; that is, $S_n = d_{mn} E_m$: 1) the 21-coupling, length-extensional mode in the x-direction, 2) the 24-coupling, thickness-shear mode in the x-plane, that is, the yz-plane, and 3) the 22-coupling, thickness-extensional mode in the y-direction. These three vibrational modes are illustrated in Fig. 5.6. We denote the lengths of the sample in the x-, the y- and the z-directions as x, y and z, respectively. In the y-cut plate, the lengths correlate as $y < x$ and $y < z$; therefore, at the resonance of the 22-mode, in which the

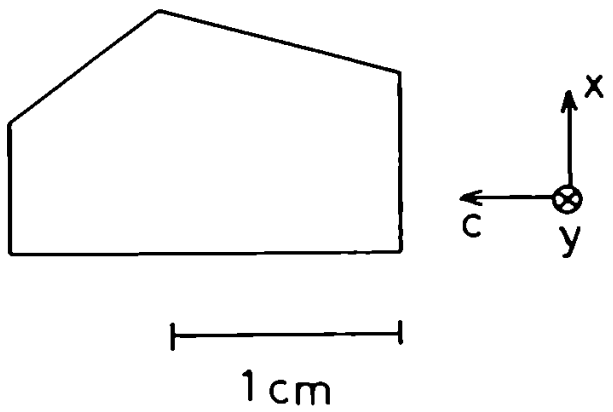

Fig. 5.7. Configuration of the sample, a pentagonal *y*-cut plate of $LiNbO_3$:Fe. The length in the *y*-direction is about 1.51 mm.

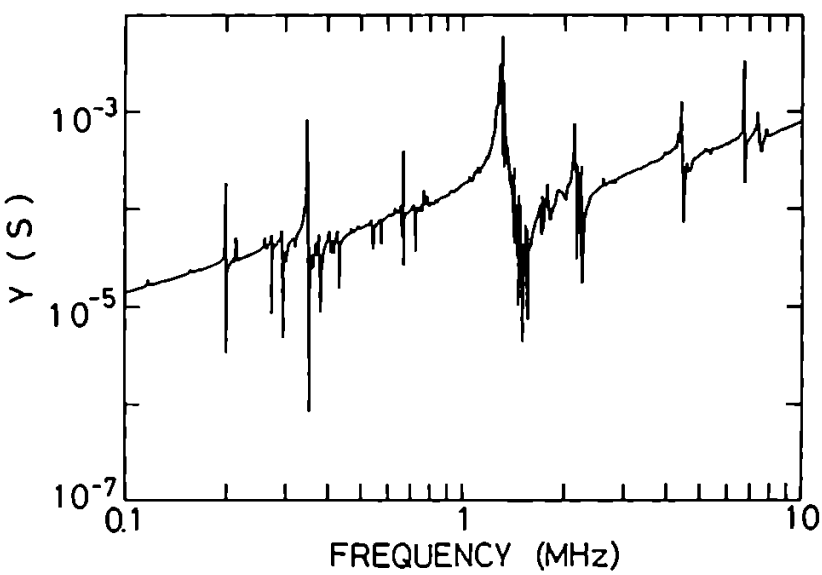

Fig. 5.8. Frequency characteristic of the admittance in the sample shown in Fig. 5.7.

(a)

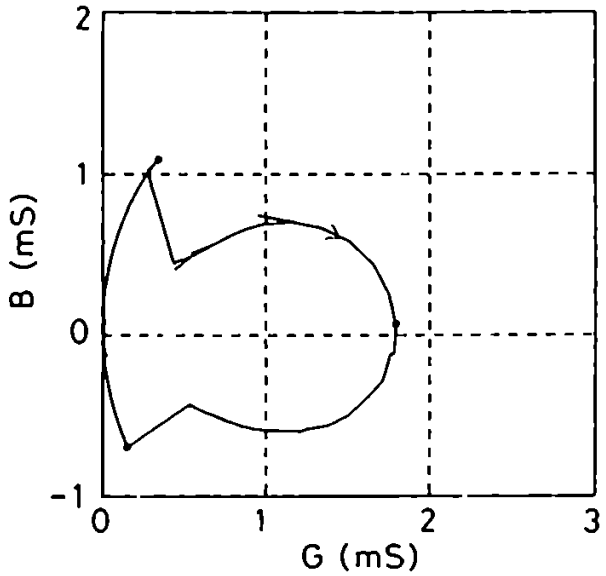

(b)

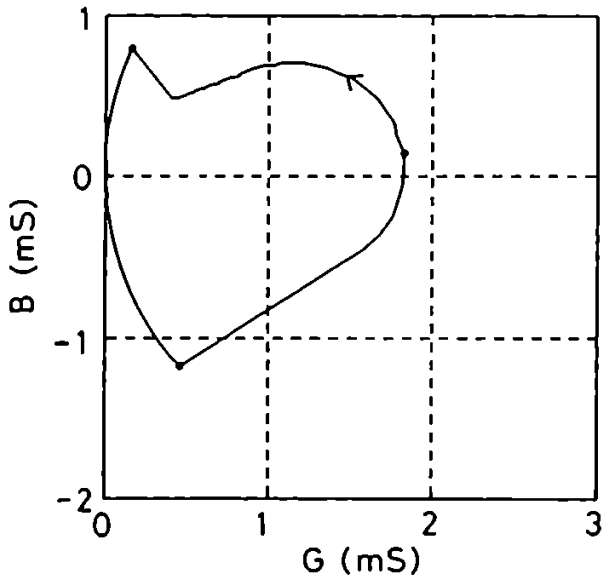

Fig. 5.9. Conductance-susceptance (G-B) characteristics of the sample with PR grating at the oscillation level of 1 V near the resonance of the 21-mode. (a) The case when frequency increases. (b) The case when it decreases.

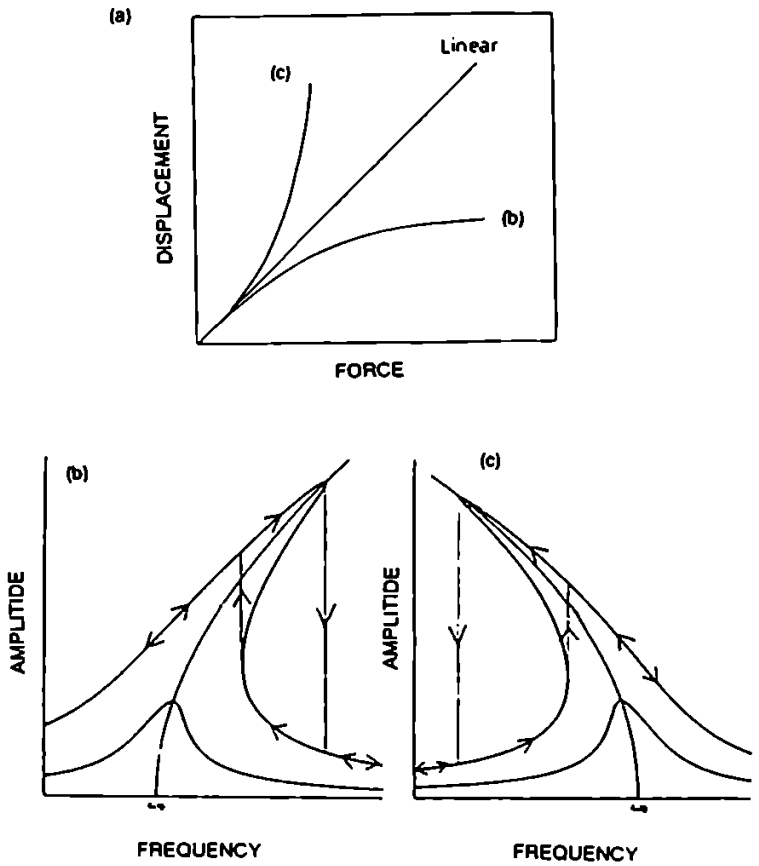

Fig. 5.10. The reason for the generation of the nonlinear jump and hysteresis. When the relationship between force and displacement is nonlinear as in curve (b) in figure (a); the case of hard spring, and curve (c); the case of soft spring, the resonance curves decline as in figures (b) and (c), respectively. Then, the jump and hysteresis of the amplitude can occur when the amplitude is large.

(a)

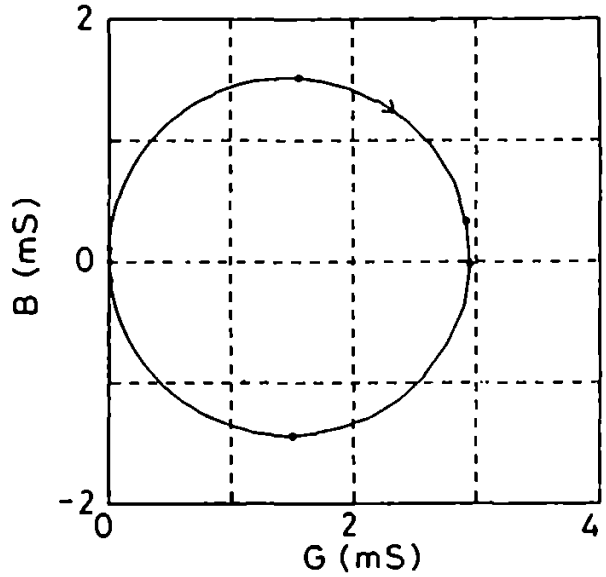

(b)

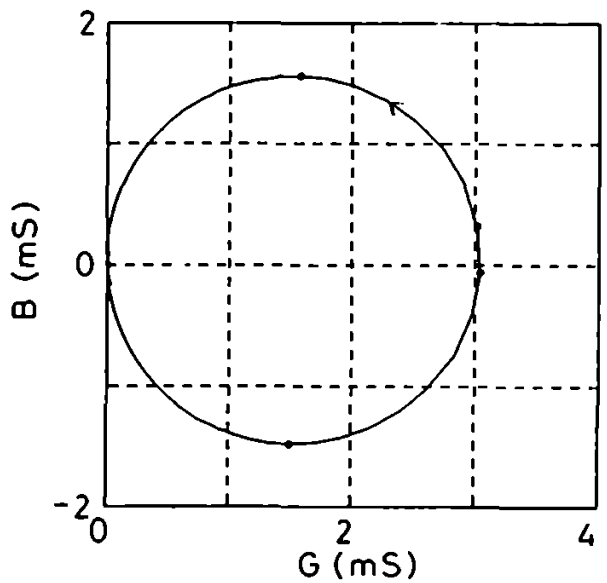

Fig. 5.11. The G-B characteristics of the sample with the PR grating in the 21-mode at the oscillation level of 0.05 V, when the frequencies are (a) up and (b) down.

Table 5.V. The Q-value, the electromechanical coupling coefficient k, and the resonance frequency of the sample with the PR grating in the 21-mode.

osc level		0.05 V	1 V
frequencies			
up	Q	2170	651
	k	20.8 %	20.7 %
	$\omega_m/(2\pi)$	0.34653 MHz	0.346540 MHz
down	Q	2170	750
	k	20.8 %	20.7 %
	$\omega_m/(2\pi)$	0.34653 MHz	0.346528 MHz

Table 5.VI. The Q-value, the electromechanical coupling coefficient k, and the resonance frequency of the sample with the PR grating in the 24- and 22-modes when the frequencies increase.

modes	osc level	0.05 V	1 V
24	Q	938	1290
	k	23.4 %	23.17 %
	$\omega_m/(2\pi)$	1.295 MHz	1.295 MHz
22	Q	3730	3730
	k	32.7 %	32.8 %
	$\omega_m/(2\pi)$	2.14912 MHz	2.14918 MHz

Table 5.VII. The Q-value, the electromechanical coupling coefficient k, and the resonance frequency of the sample after the annealing in the 21-mode.

osc level		0.05 V	1 V
frequencies			
up	Q	3850	4950
	k	20.7 %	20.9 %
	$\omega_m/(2\pi)$	0.34681 MHz	0.34664 MHz
down	Q	3470	4330
	k	20.7 %	20.9 %
	$\omega_m/(2\pi)$	0.34679 MHz	0.34665 MHz

resonance occurs in the y-direction, the vibration in the x- and z-directions is clamped. At the resonance of the 21-mode, in which the resonance occurs in the x-direction, the vibration in the z- as well as the y-direction is free because of the existence of Poisson's ratio. When the sample is elongated in the x-direction, it shrivels in the z-direction.

5.3.2 Experimental Results

Figure 5.7 shows the configuration of the sample, a pentagonal y-cut plate of $LiNbO_3$:Fe. The value of y is about 1.51 mm. The PR grating is written in large volume in the crystal by an expanded beam diameter of 20 mm. The ratio of I_1 and I_2 before entering into the crystal is 1 : 1. The value of Λ is about 1.5 μm. Whole Au electrodes are now deposited on the y-planes. The frequency characteristic of the admittance is shown in Fig. 5.8, in which the resonances of the 21- the 24- and the 22-modes exist at about 0.35 MHz, 1.30MHz and 2.15 MHz, respectively.

Near the resonance of the 21-mode, the conductance-susceptance (G-B) characteristics at the oscillation level of 1 V are shown in Figs. 5.9(a) and 5.9(b), where Fig. 5.9(a) is representative when the frequency increases and Fig. 5.9(b) when it decreases. We find the abrupt jumps and hysteresis of the admittance. Jump and hysteresis are typical phenomena of nonlinear vibration based on the bi-stability of the vibrational system. Figure 5.10 explains the reason for the generation of nonlinear jump and hysteresis.

Figures 5.11(a) and 5.11(b) show the G-B characteristics of the same mode at the oscillation level of 0.05 V, when the frequencies are up and down, respectively. The nonlinear jump cannot be observed, unlike the case at the oscillation level of 1 V. The admittance loci are almost true circles and the vibration is almost linear. Small driving voltage cannot cause the nonlinear phenomena. Next, we turn our attention to the Q-value, the electromechanical coupling coefficient k, and the resonance frequency, which are shown in Table 5.V. We find that the Q-value decreases when nonlinear phenomena such as nonlinear jump occur. The decrease of the Q-value refers to the energy transfer from linear vibration to nonlinear vibration. The electromechanical coupling coefficient and the resonance frequency are almost the same in these cases.

In the case of 24- and 22-modes the nonlinear jump is not observed. Table 5.VI shows the Q-value, the electromechanical coupling coefficient k, and the resonance frequency in these modes. The variation of the Q-value upon changes in the oscillation level, which is one of the nonlinear characteristics, can be observed in the 24-mode, but it is not observed in the 22-mode.

Next, the sample is annealed at 200 ^{0}C for 1 hour, so that the optical diffractive grating can be erased after annealing. The electromechanical measurement after annealing above is performed in order to compare with the characteristics observed before annealing. The experimental results of the 21-mode are shown in Table 5.VII. An increase of the Q-value is observed and the non-

Table 5.VIII. The variation of the Q-value and resonance frequency ω_m of the 21-mode after annealing. The symbols "N", "I" and "D" denote no significant change, increase and decrease, respectively. The value in parentheses shows the variation numerically.

Λ Electrodes		1μm	3.9μm
Whole	ω_m	N	I(0.05%)
	Q	N(10000~15000)	D(20000 → 5600)
Partial	ω_m	I(0.025%)	I(0.05%)
	Q	I(2600 → 17000)	I(2000 → 20000)

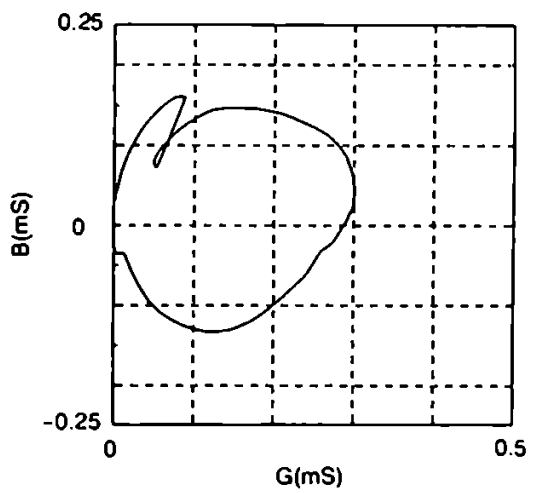

Fig. 5.12. Nonlinear jump phenomenon observed in the admittance circle near the resonance frequency of the 21-mode.

linear jump is eliminated. We can conclude that the PR grating written in the piezoelectric transducer can cause a decrease of the Q-value and the generation of nonlinear acoustic vibration, especially in the 21-mode.

§5.4. Influence of Variation of PR grating on Piezoelectric Vibration

In this section, we describe the influence of the variation of the PR grating on the piezoelectric vibration, for example, after thermal annealing,[5] by changing the intensity ratio of I_1 to I_2,[7] after the incidence of homogeneous light,[7] and by the aging.[7]

5.4.1 Influence of Thermal Annealing

A y-cut plate of $LiNbO_3$:Fe, which is rectangular, x = 7.19 mm, y = 1.51 mm, and z = 4.03 mm, is used. The Q-value of the present rectangular sample is, generally, larger than that of the pentagonal sample described in the previous section because of the regularity of its shape. The ratio of I_1 to I_2 is 1:1, and the diameter of the beam is about 20mm. The period of PR grating Λ is selected to be about 1μm and 3.9μm. After the PR grating is written, whole Au electrodes are deposited on the y-planes, and 1) the frequency characteristics of admittance, 2) the current-voltage (I-V) characteristics, and 3) the spectral analysis of harmonic generation, respectively, are measured near the resonance frequencies of the 1) 21-mode, 2) the 24-mode, and 3) the 22-mode. Concerning the 21-mode, the measurement is made in the case of not only whole electrodes but also partial ones, 2mm(x)×1mm(z), deposited on the center of the y-planes.

As described in the previous section, the optical diffractive grating can be erased after annealing at 200°C for 1 hour, so we perform the similar measurement as above after annealing to compare with the characteristics observed before annealing. A virgin y-cut plate, on which the PR grating has not been written, is prepared in order to examine the intrinsic characteristics of $LiNbO_3$:Fe.

In measuring the frequency characteristics of admittance, we also note the variation of 1) the Q-value of the resonance, 2) the resonance frequency ω_m, and 3) the existence of the nonlinear jump phenomena, due to annealing.

Table 5.VIII shows the variation of Q and ω_m after annealing in the 21-mode for two values of Λ and two kinds of electrodes. We find that the rate of the variation is larger when the electrodes are partial or when the value of Λ is larger.

When the Q-value is small (about 2000 in the sample before annealing with the *partial* electrodes and the grating of Λ = 3.9 μm), we observe the nonlinear jump phenomenon of an admittance circle, as shown in Fig.5.12. Although the $LiNbO_3$:Fe resonator without the PR grating shows an intrinsically weak nonlinear jump phenomenon, the sample with the PR grating shows

(a)

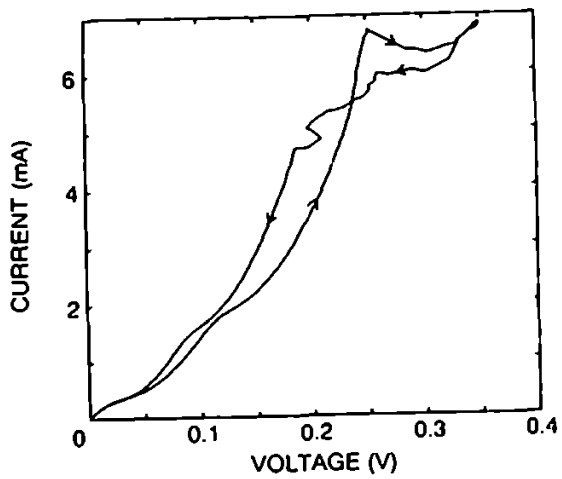

(b)

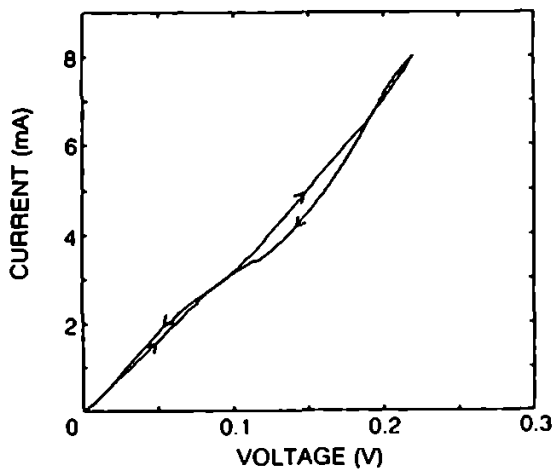

Fig. 5.13. (a) The *I-V* characteristic of the sample with the PR grating at the resonance frequency of the 21-mode. (b) Intrinsic *I-V* characteristic at the resonance frequency of the 21-mode.

Table 5.IX. The variation of the Q-value and the resonance frequency ω_m of the 24- and 22-modes after annealing.
The notations used are the same as in Table 5.VIII.

Modes	Λ	1μm	3.9μm
24	ω_m	N	I(0.08%)
	Q	N(4000 → 3000)	N(1300 → 2100)
22	ω_m	N	D(0.15%)
	Q	N(4800~5500)	I(300 → 3400)

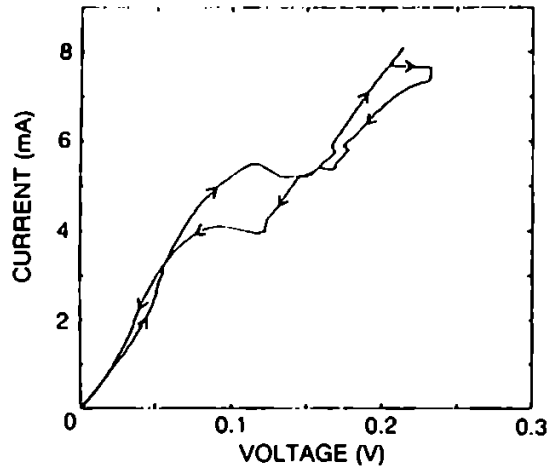

Fig. 5.14. The *I-V* characteristic of the sample with the PR grating at the resonance frequency of the 24-mode.

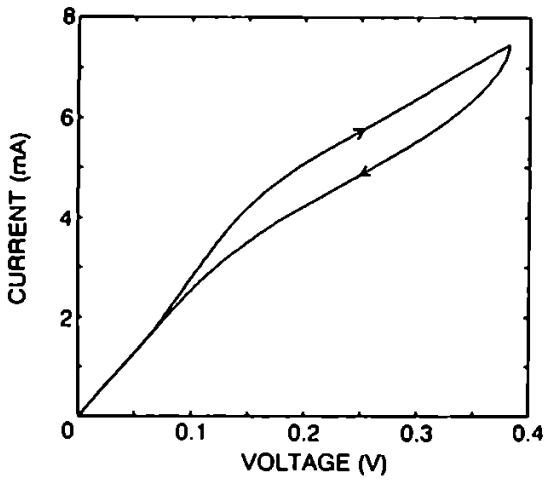

Fig. 5.15. The *I-V* characteristic of the sample with the PR grating at the resonance frequency of the 22-mode.

the phenomenon distinctly and at phase angles different from that of the former. After annealing of the sample, the Q-value increased tenfold to about 20000, and the nonlinear jump phenomenon disappeared. We find that the PR grating causes the decrease of Q and the generation of the nonlinear phenomena, as described in the previous section.

On the other hand, in the case of the sample with the *whole* electrodes and the grating of Λ = 3.9 μm, the nonlinear jump phenomenon did not appear before annealing, and the Q-value was about 20000. By fixing the sample with adhesive tape, Q-value decreased, then the nonlinear jump phenomena appeared. This suggests that too large Q-value does not cause the present nonlinear phenomena in the sample with the PR grating. The usual nonlinear effect, intrinsic to the $LiNbO_3$:Fe resonator, is likely to be enhanced when the Q-value increases because the higher orders of strain become more effective; thus, the nonlinear phenomena observed here in the sample with the PR grating are unusual and due to a completely different mechanism. *After annealing*, the phenomenon appeared and the Q-value decreased. This suggests the existence of the PR grating even after annealing. On the other hand, the optical Bragg diffraction did not occur after annealing, so the PR grating is thought to disappear. These two facts are seemingly not consistent with each other. Grating sufficient to cause the nonlinear phenomena seems to *partially remain* even after annealing. Moreover, the form of the electrodes (whole or partial), influences the nonlinear behavior, even though the other experimental conditions are the same.

The nonlinear phenomena are confirmed by I-V characteristics or harmonic generation, as well as by admittance characteristics. Figure 5.13(a) shows the I-V characteristic of the sample with whole electrodes and the grating of Λ = 1 μm after annealing. Figure 5.13(b) shows the intrinsic characteristic of $LiNbO_3$:Fe for comparison. In Fig. 5.13(a), we observe hysteresis and the marked variation of the gradient dI/dV. The gradient becomes negative in some range of the voltage. On the other hand, the weak nonlinearity in Fig. 5.13(b) is caused by the large Q-value of the resonator, which is the usual effect. Harmonic generation was also observed in both samples. Not only odd harmonics, but also even ones were observed.

Table 5.IX shows the variation of Q and ω_m after annealing in the 24- and 22-modes. Only whole electrodes are used. The value of ω_m in the 22-mode shows a tendency to decrease after annealing. This feature is different from the results in other modes. Another influence of the PR grating on the piezoelectric vibration is greater in the 22-mode than in other modes. The nonlinear jump phenomenon of the PR grating was observed in the 24-mode as well as in the 21-mode, but not in the 22-mode.

The I-V characteristic in the 24-mode for the sample with the grating of Λ =1 μm before annealing (in Fig. 5.14) shows marked hysteresis and negative gradients, as in the 21-mode. In contrast, the intrinsic characteristic in the 24-mode shows little hysteresis and no negative gradient.

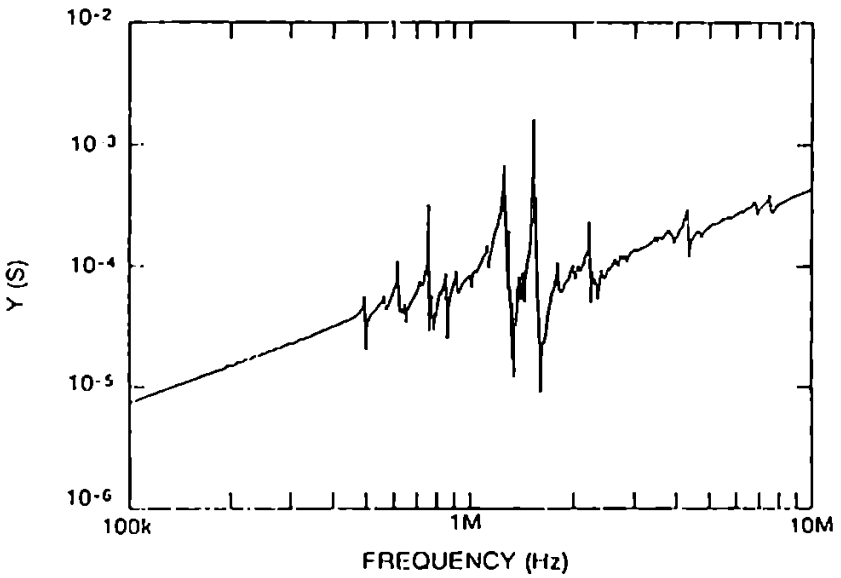

Fig. 5.16. Frequency characteristic of the admittance of the sample used in the experiment changing the value β. The shape of the sample is irregular; therefore, there are many peaks of Y due to the 21-mode, and the Q-value is small.

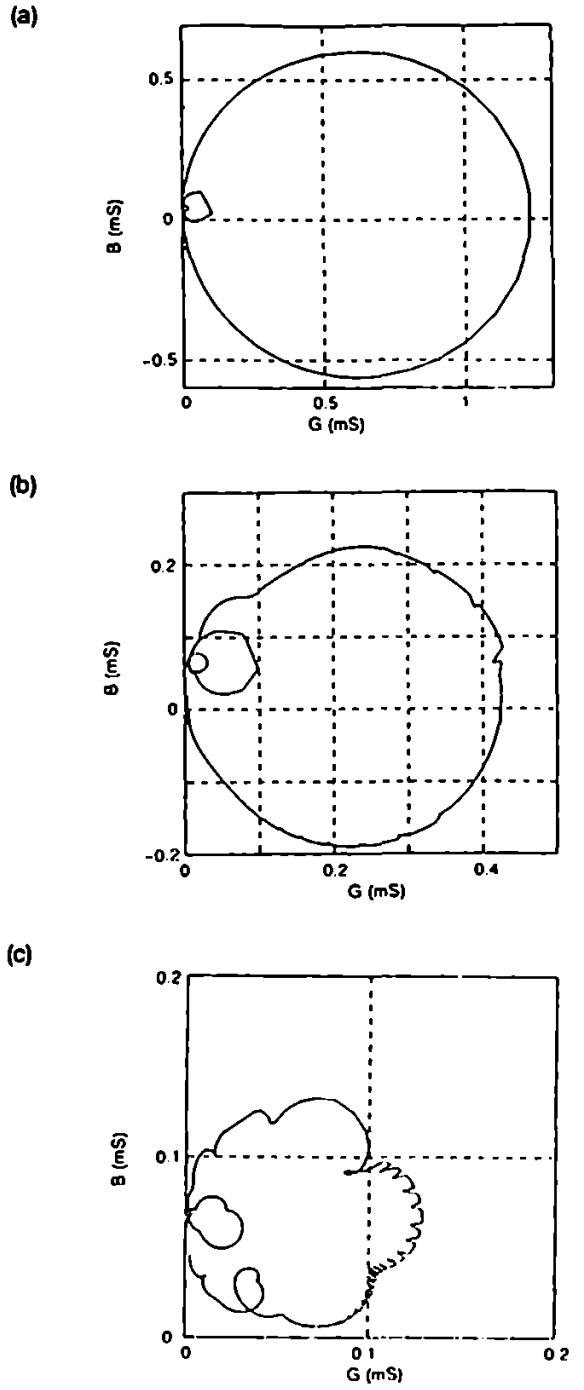

Fig. 5.17. Admittance circles of the 21-mode measured from 780 to 880 kHz with the PR grating formed by (a) $\beta = 0.1$, (b) $\beta = 0.5$, and (c) $\beta = 1$, respectively.

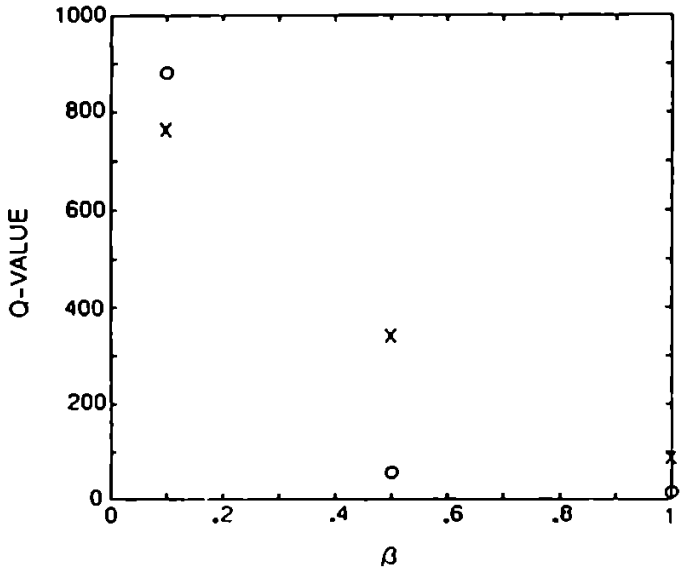

Fig. 5.18. The variation of the *Q*-value when changing the value of β. The notation "o" indicates the results measured from 600 to 700 kHz and the "x" from 780 to 880 kHz.

The $I-V$ characteristic in the 22-mode for the sample with the grating of Λ=1μm before annealing (in Fig. 5.15) shows hysteresis, but similar hysteresis is also observed in the intrinsic characteristic in the 22-mode. Hence, we cannot conclude at present the influence of the PR grating on the nonlinear phenomena in the 22-mode, even though the Q-value in the 22-mode was influenced by the PR grating. On the other hand, in the 21- and 24-modes, we can conclude the influence of the PR grating on the nonlinear phenomena, involving the low Q-value.

We also find that the variation of ω_m after annealing has no relation to that of Q. The variation of ω_m probably is related to that of the stiffness of the nonlinear spring, as suggested in Fig. 5.10.

5.4.2 Influence of Changing Intensity Ratio of I_1 to I_2

In the experiment described in §5.4.1, the value of Λ was changed and the influence of the grating on the piezoelectric vibration was investigated before and after the annealing. The change in Λ and thermal annealing can change the space-periodic internal electric field E_{SC} expressed in eqs. (5.2.12a) and (5.2.16). However, E_{SC} involves E_N which is directly proportional to Λ and E_D which is inversely proportional to Λ, as expressed in eqs. (5.2.17) and (5.2.18), respectively. Therefore, experimenting by changing the value of Λ cannot clarify the relationship between the value of E_{SC} and its influence on the piezoelectric vibration.

For that reason, in this subsection the intensity ratio of I_1 to I_2 before mixing is changed in order to investigate the relationship between E_{SC} and its influence, because E_{SC} is in proportion to the intensity modulation index m, as in eq.(5.2.16), and m is determined by the ratio of I_1 to I_2, as in eq.(5.2.6).

The power of I_2 before mixing is fixed at 550 mW/cm^2, and the ratio of I_1 to I_2, β, is changed to 0.1, 0.5, and 1, by attenuating I_1 using the attenuator Att1 in Fig. 5.4. The diameters of the beams are not expanded. The value of m is as follows:

$m = 0.54$ when $\beta = 0.1$,
$m = 0.94$ when $\beta = 0.5$,
$m = 0.1$ when $\beta = 1$.

Given the value of Λ at 1.6 μm, another $LiNbO_3$:Fe resonator (its frequency characteristic of the admittance is shown in Fig. 5.16) is used as a sample. Since the shape of this sample is not regular, there are many peaks of admittance below 1 MHz, which are due to the 21-mode, and the Q-value is smaller.

Figures 5.17(a), 5.17(b) and 5.17(c) show the admittance circles of the 21-mode measured from 780 to 880 kHz with the PR grating formed by (a) $\beta = 0.1$, (b) $\beta = 0.5$, and (c) $\beta = 1$, respectively. We find that the increase of β, and the concomitant increase of E_{SC}, surely makes the admittance circle smaller. Figure 5.18 shows the variation of the Q-value when changing

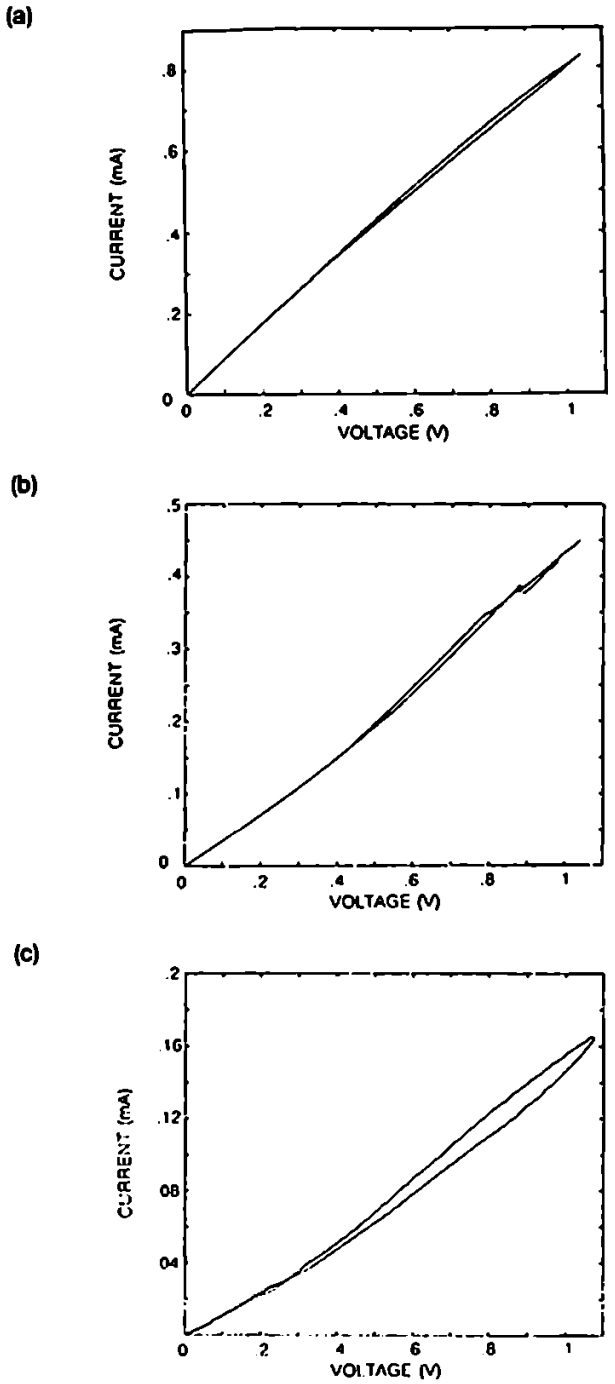

Fig. 5.19. The *I–V* characteristics when (a) $\beta = 0.1$, (b) $\beta = 0.5$, and (c) $\beta = 1$.

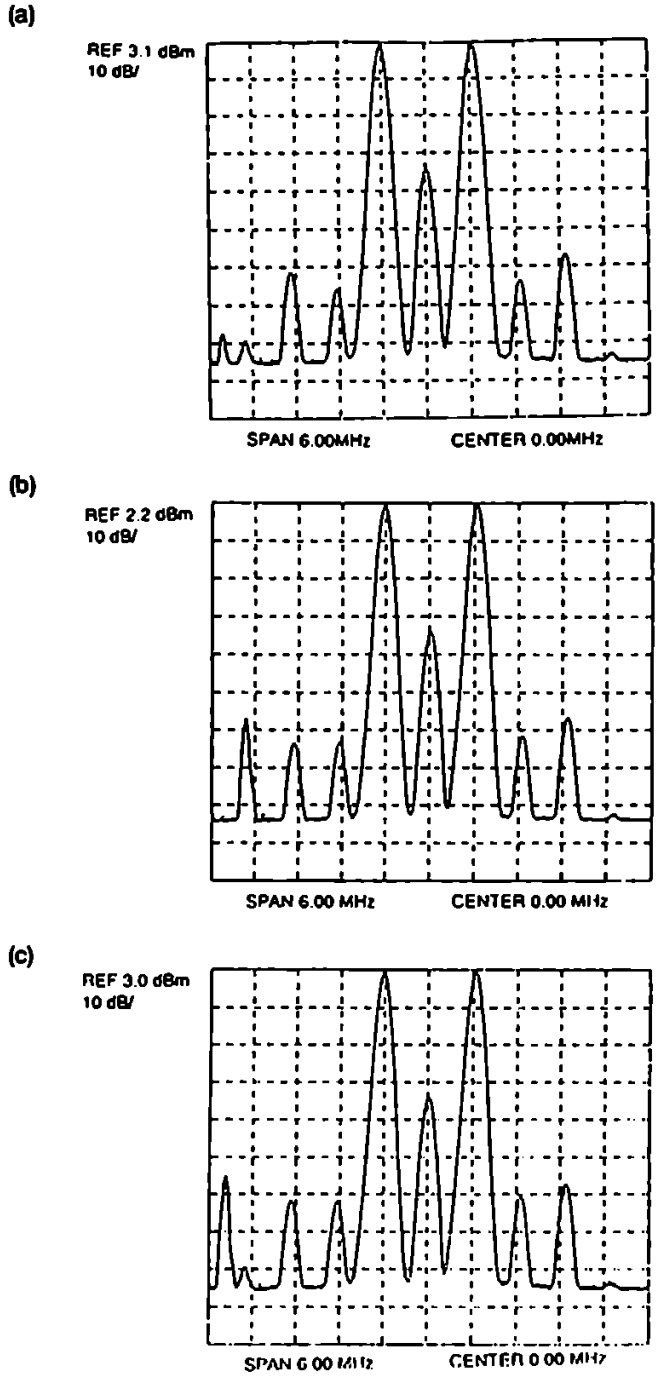

Fig. 5.20. Results of the spectrum analysis when (a) $\beta = 0.1$, (b) $\beta = 0.5$, and (c) $\beta = 1$.

(a)

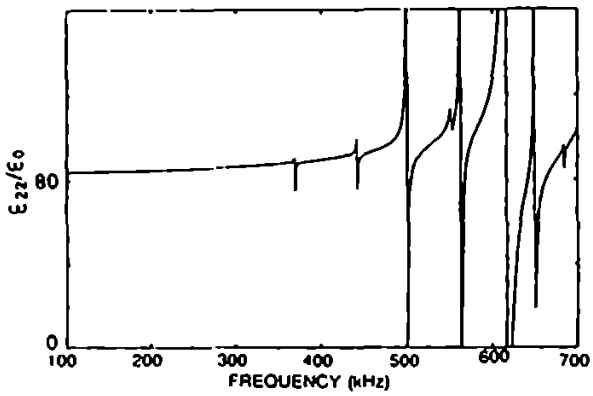

(b)

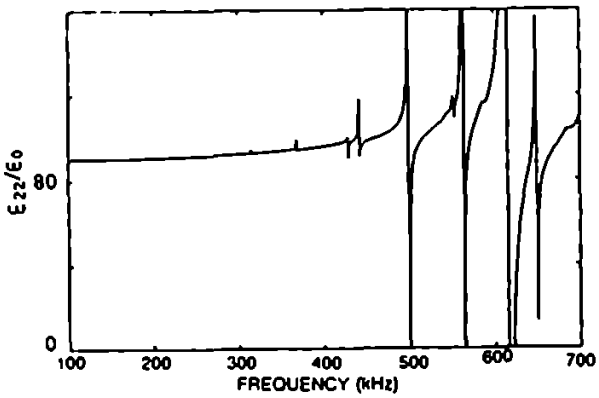

(c)

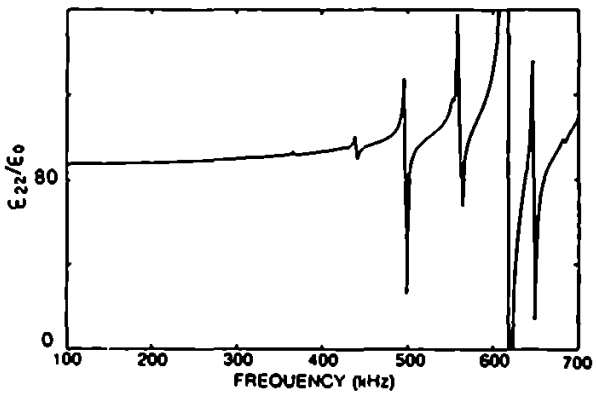

Fig. 5.21. Frequency characteristics of the dielectric constant $\varepsilon_{22} / \varepsilon_0$ when (a) $\beta = 0.1$, (b) $\beta = 0.5$, and (c) $\beta = 1$.

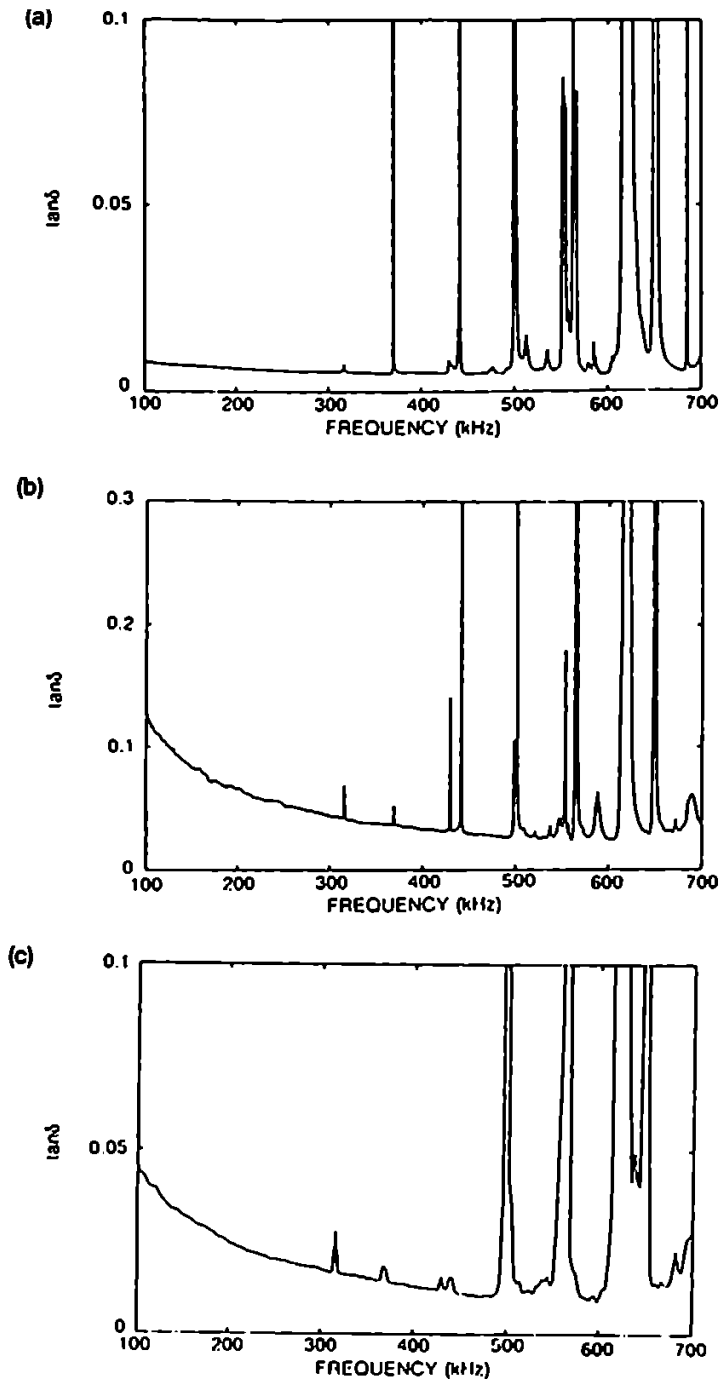

Fig. 5.22. Frequency characteristics of the dielectric loss (tan δ) when (a) β = 0.1, (b) β = 0.5, and (c) β = 1.

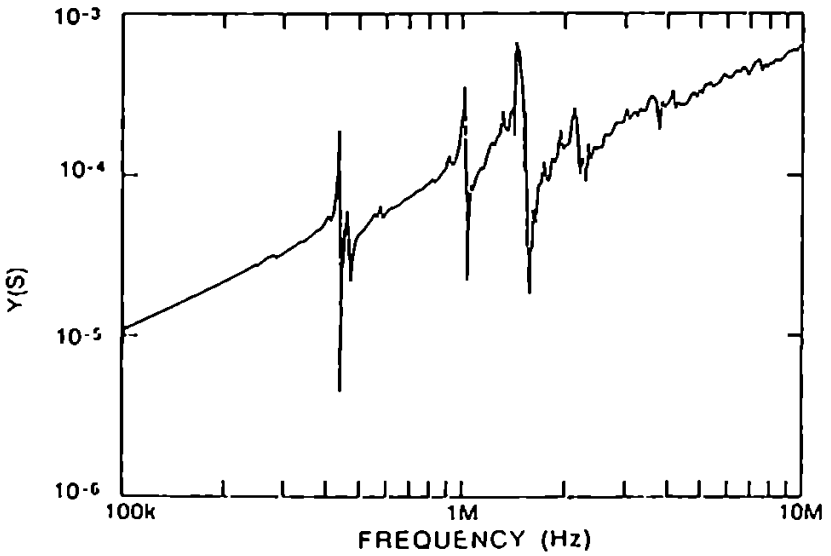

Fig. 5.23. Frequency characteristic of admittance of the sample used in the experiment investigating the influence of homogeneous light incidence.

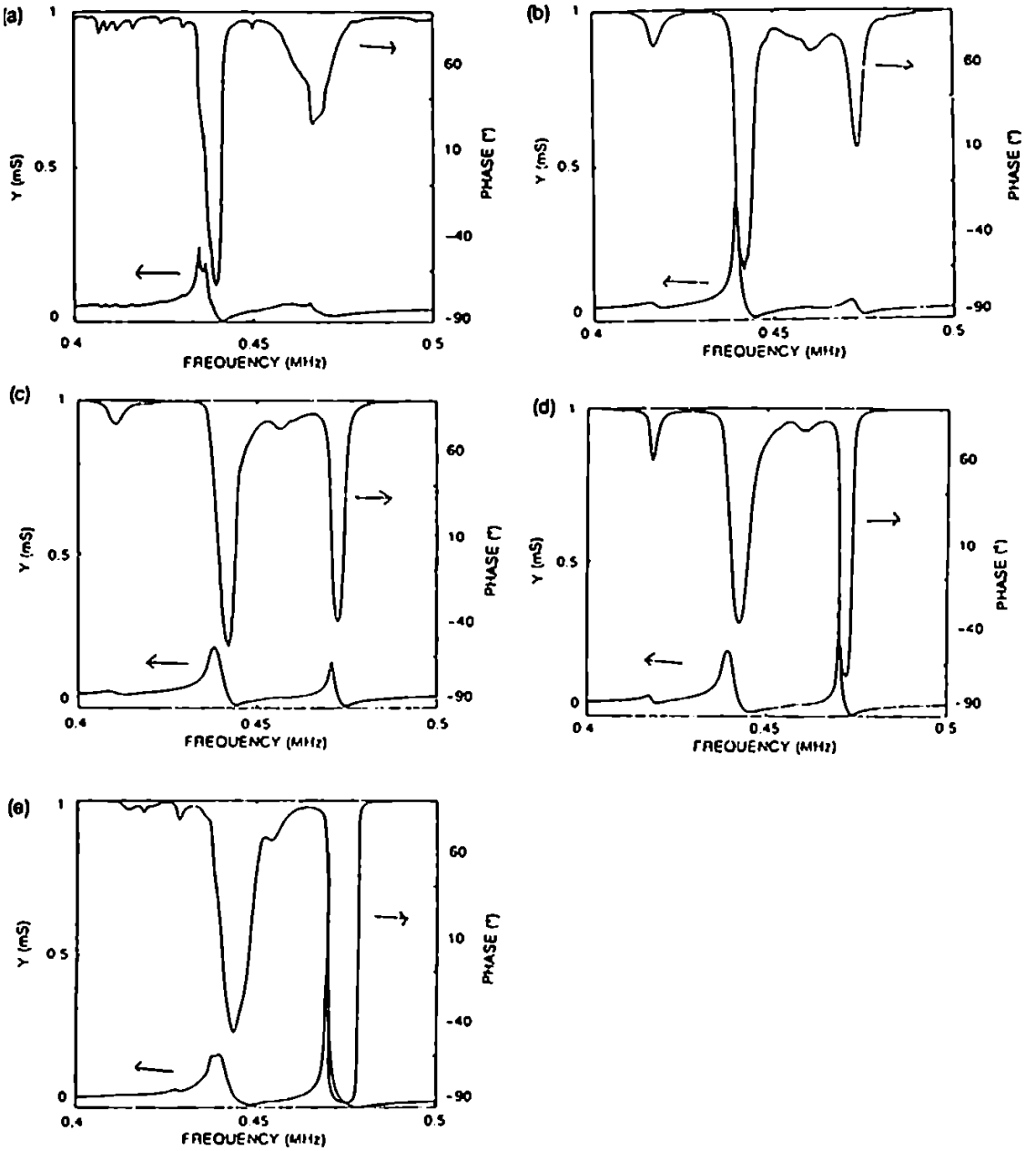

Fig. 5.24. Frequency characteristics of $|Y|$ and phase angle near the resonance frequency of the 21-mode, about 0.45 MHz, after the homogeneous light incidence for (a) 0 min., (b) 35 min., (c) 60 min., (d) 90 min., and (e) 150 min., respectively.

the value of β, measured from 600 to 700 kHz and from 780 to 880 kHz. The increase of E_{SC} causes the decrease of Q-value, which signifies the depression of the linear vibration. This result is consistent with the previous experimental results reported in this chapter; however, clear nonlinear phenomena such as the nonlinear jump are not observed here. The reason is as follows. Because of the irregularity of the sample shape, the Q-value, which is less than 100 when $\beta = 1$, is much smaller than that of other samples. Small Q-value means small amplitude of the linear vibration. Accordingly, the present Q-value is too small to cause the nonlinear jump phenomenon, because the phenomenon requires a larger amplitude of vibration, as suggested in Fig. 5.10.

The I-V characteristics and the results of the spectrum analysis are also shown in Figs. 5.19 and 5.20, respectively, when (a) $\beta = 0.1$, (b) $\beta = 0.5$, and (c) $\beta = 1$. We find that nonlinearity becomes slightly more pronounced as E_{SC} increases.

The variation of the dielectric constant was also investigated with change in β. Figures 5.21 and 5.22 show the frequency characteristics of the dielectric constant (permittivity) $\varepsilon_{22} / \varepsilon_0$ and the dielectric loss (tan δ), respectively, when β changes. Real and imaginary part of the complex dielectric constant are calculated using the components of the $\pi/2$ phase difference and in-phase between I and V, respectively. The tan δ is given by the ratio of the imaginary to the real part. If the dielectric loss did not exist in the material, only the component of $\pi/2$ phase difference would contribute to the permittivity. Piezoelectric resonance increase the in-phase component, as shown in Fig. 3.5, and therefore, the dielectric loss apparently. The sharp peaks in Figs. 5.21 and 5.22 are due to the piezoelectric resonances of the 21-mode, which do not have any relationship to the intrinsic dielectric property. The dielectric constant does hardly change when β increases, as in Figs. 5.21; however, the dielectric loss when $\beta = 0.5$ and $\beta = 1$ is larger than when $\beta = 0.1$ at frequencies below about 500 kHz, as in Figs. 5.22. This suggests movements of ions, which compose the PR grating, in the y-direction through Coulomb's force by the external electric field in the y-direction at low frequency. The decrease of the present tan δ at higher frequency suggests that the ions cannot follow the external force; that is, the vibration of the ions is inertia-controlled.

5.4.3 Influence of Homogeneous Light Incidence

In the experiment discussed in §5.4.1, the thermal annealing at 200 °C for 1 hour could not completely eliminate the PR grating. The residual PR grating often even caused nonlinear behavior. In this subsection, homogeneous light incidence onto the crystal is performed to eliminate the PR grating homogeneously and completely.

The sample is an irregular form of y-cut plate with a frequency characteristic of admittance as shown in Fig. 5.23. In forming the PR grating, the intensity of light is 550 mW/cm^2 with $\beta = 1$,

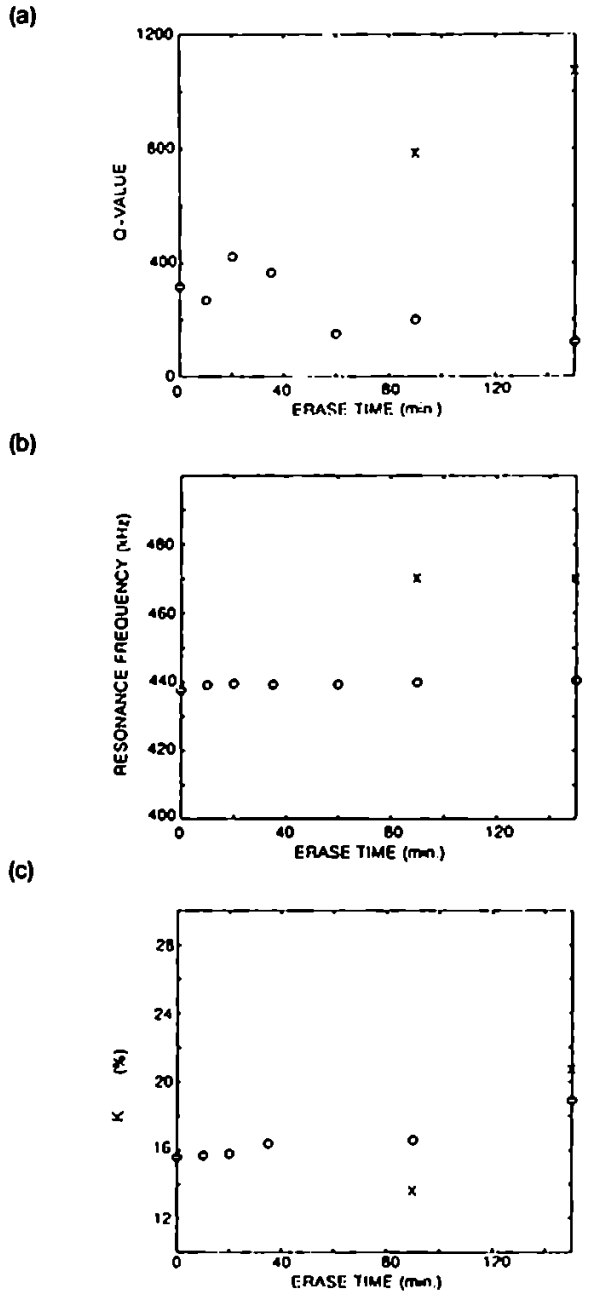

Fig. 5.25. The variation of (a) the Q-value, (b) the resonance frequency ω_m, and (c) the electromechanical coupling coefficient k after the homogeneous light incidence, where the notation "○" and "×" show the data at lower and higher resonance frequencies appearing in Figs. 5.24, respectively.

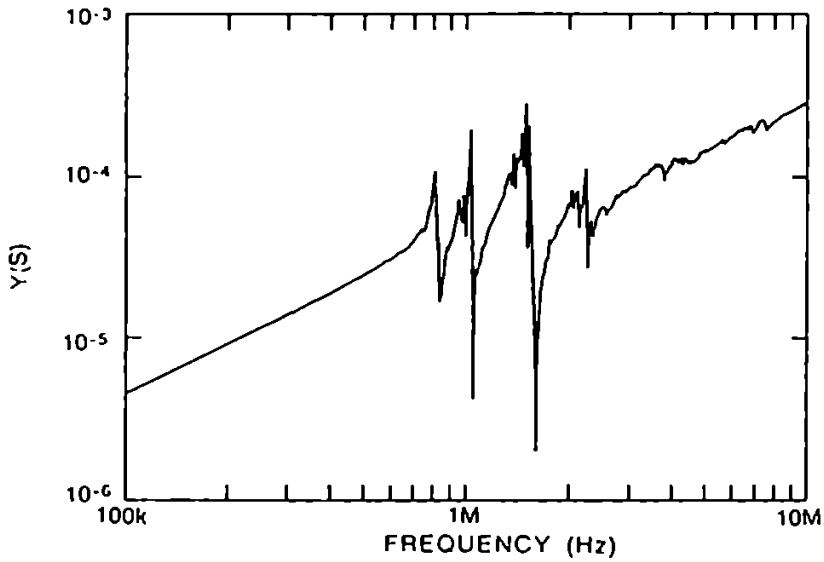

Fig. 5.26. Frequency characteristic of admittance of the sample used in the experiment investigating the time variation of the PR grating at room temperature.

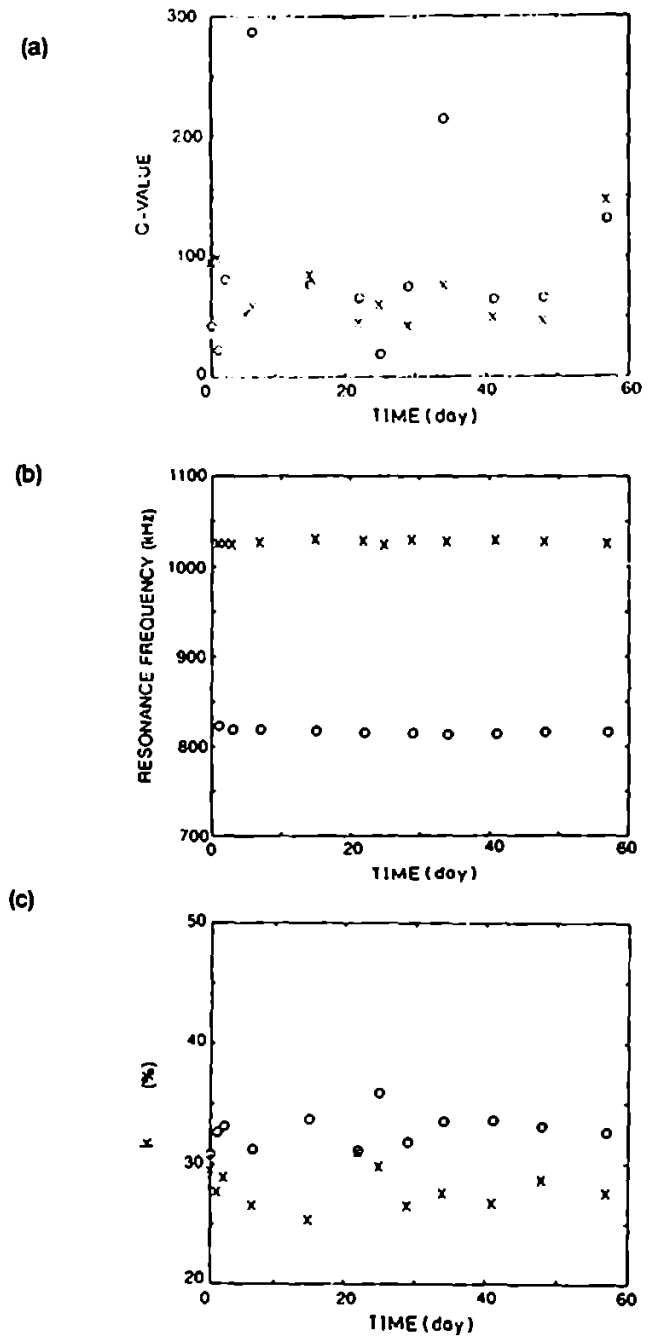

Fig. 5.27. The time variation of (a) the Q-value, (b) the resonance frequency ω_m, and (c) the electromechanical coupling coefficient k at room temperature in a dark place, where the notation "○" and "×" show the data at resonance frequencies of about 820 kHz and 1050 kHz, respectively, and the former is caused by the 21-mode.

and after depositing electrodes only I_2 with the power of 180 mW/cm^2 is incident from the side of the crystal.

Figure 5.24 shows the frequency characteristic of $|Y|$ and phase angle near the resonance frequency of the 21-mode (about 0.45 MHz), after the incidence of homogeneous light for (a) 0 min., (b) 35 min., (c) 60 min., (d) 90 min., and (e) 150 min., respectively. We find that two peaks of resonance exist and the peak of higher frequency grows by degrees relative to the incidence of light. The variation of the Q-value, the resonance frequency ω_m, and the electromechanical coupling coefficient k are shown in Figs. 5.25(a), 5.25(b), and 5.25(c), respectively, where the notation "○" and "×" show the data at lower and higher resonance frequencies appearing in Figs. 5.24, respectively. The energy transfer between the two peaks seems to have occurred. The linear vibration depressed by the PR grating becomes larger as the time of light incidence increases. In addition, the PR grating depresses the electromechanical coupling coefficient.

Clear influence of the PR grating on nonlinear behavior was not observed in the present sample, even though the PR grating depresses the Q-value, that is, depresses the linear vibration. The reason seems to be the same as in the sample investigated in §5.4.2.

5.4.4 Time Variation of PR Grating at Room Temperature

In this subsection, time variation of the PR grating at room temperature (about 15 °C) is investigated. The sample is an irregular form of y-cut plate with a frequency characteristic of admittance as shown in Fig. 5.26. In forming the PR grating, the intensity of light is 550 mW/cm^2 with $\beta = 1$, and after depositing electrodes the sample is preserved at room temperature in a dark place. The time variation of the Q-value, the resonance frequency ω_m, and the electromechanical coupling coefficient k are shown in Figs. 5.27(a), 5.27(b), and 5.27(c), respectively, where the notation "○" and "×" show the data at resonance frequencies of about 820 kHz and 1050 kHz, respectively, and the former is caused by the 21-mode. We find irregular variation of the Q-value and k and the stability of ω_m within 60 days. The nonlinear jump phenomenon was often observed during the 60 days, for example, after 22 days, with decrease of the Q-value. However, we cannot find a tendency of the PR grating to fade out within 60 days at room temperature in a dark place.

§5.5. Summary of Experimental Results

The PR grating formed in the piezoelectric $LiNbO_3$:Fe transducer decreased the Q-value, and therefore, depressed the linear vibration. It often caused nonlinear behavior such as nonlinear jump and hysteresis, accompanied by the decrease of the Q-value. Energy transfer from the linear to the nonlinear vibration occurred.

Even after the thermal annealing, the PR grating seemed to partially remain, and it often caused nonlinear behavior.

The generation of the present nonlinear behavior was related to the forms of the sample, the forms of the electrodes, and the vibrational mode. This nonlinear behavior could often occur in the 21- and the 24-modes, but was not evident in the 22-mode.

Too large Q-value depressed this nonlinear behavior. The usual nonlinear effect is probably enhanced when the Q-value increases because the higher orders of strain become more effective. Therefore, the nonlinear phenomena observed here in the sample with the PR grating are unusual and due to a completely different mechanism. They also did not appear clearly in the sample with very small Q-value due to the irregularity of the form.

The value of the space-periodic internal field E_{SC} clearly influenced the piezoelectric characteristics and the dielectric loss.

§5.6. Model for Nonlinear Phenomena

In the previous sections in this chapter, the decrease of Q-value and the generation of nonlinear vibration were detected in the $LiNbO_3$:Fe piezoelectric transducer in which photorefractive (PR) grating was formed. The decrease of Q means the depression of linear vibration, which is consistent with the generation of nonlinearity. The energy transfer from linear to nonlinear vibration can occur. The PR grating enhances or produces the nonlinearity in crystal. This nonlinearity was strongly influenced by the form of the sample. When the Q-value was too large or too small, depending upon the form of the sample, the present nonlinear behavior became obscure. We explain the experimental results by a new concept, space-periodic modulation of piezoelectric polarization due to the PR internal field,[8] which is a physical model within the range of possibility.

5.6.1 Two Modes of Vibration

First of all, we consider a compound pendulum connected by a nonlinear spring, as in Fig. 5.28(a). Vibration of the pendulum in Fig. 5.28(a) can be separated into two modes, as in Figs. 5.28(b) and 5.28(c), an in-phase and an antiphase vibration of the two pendulums, respectively.

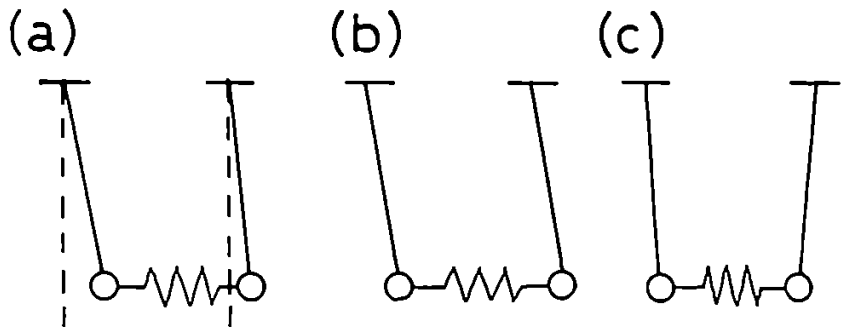

Fig. 5.28. (a) A compound pendulum connected by a nonlinear spring. (b) An in-phase mode of the vibration. (c) An antiphase mode of the vibration. In the antiphase mode, as the nonlinear spring does vibrate, the nonlinear vibration does occur.

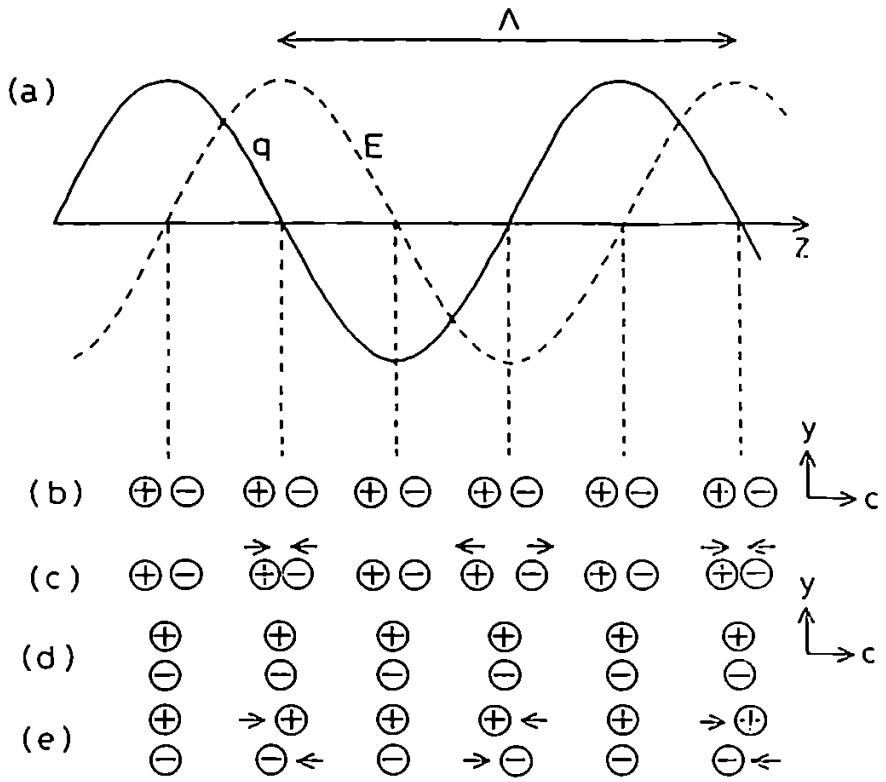

Fig. 5.29. (a) Space-sinusoidal charge distribution of the PR grating in a solid line and static internal electric field in a dashed line. (b) Alternating, that is, periodic in time domain, polarization in the *c*-direction. (c) The electric dipoles can be strained longitudinally by the internal field. (d) Alternating polarization in the *y*-direction. (e) The electric dipoles can be strained transversely by the internal field. Longitudinal anti-phase vibration could occur in the *c*-direction.

The displacements of two pendulums in Fig. 5.28(a) are expressed as u_1 and u_2, then the displacements of the in-phase and antiphase vibration, u_{in} and u_{anti}, respectively, are expressed as

$$u_{in} = u_1 + u_2, \tag{5.6.1a}$$

$$u_{anti} = \Delta u = -u_1 + u_2. \tag{5.6.1b}$$

In the former, since the two pendulums are in a parallel motion with each other and the nonlinear spring does not vibrate, nonlinear vibration does not occur. In the latter, since the two pendulums move on opposite directions and the nonlinear spring does vibrate, nonlinear vibration does occur. Only antiphase vibration can contribute to nonlinear vibration, because elasticity is caused by Δu and its higher orders. That is, the generation of nonlinear vibration requires the existence of both nonlinear springs and the antiphase vibration of the springs. The displacements in the in-phase vibration are restored by forces other than the elastic force between the two particles, for example, in the case of compound pendulum shown in Fig. 5.28(b), the gravity acting on the mass of particles, or in the case of solid resonator, for example, piezoelectric transducer, other elastic forces between the present particles and other particles.

Proper frequencies of the two modes are different, but if an external force exists, as in the case of piezoelectric transducer, vibrational frequencies of the two modes are the same, because both modes of vibration are caused by the same external force by means of piezoelectric effect.

We will investigate the cause of existence of nonlinear springs and antiphase vibration of them in the case of piezoelectric transducer in which PR grating is formed. In this case, we can consider that spatial period of antiphase vibration is equal to Λ, the period of PR grating.

5.6.2 Generation of Antiphase Vibration by Space-periodic Modulation of Piezoelectric Polarization due to Photorefractive Internal Field

We consider the generation of antiphase vibration in the PR grating. A space-sinusoidal charge distribution and an internal electric field are formed in the c-direction of the crystal, represented by solid and dashed lines in Fig. 5.29(a), respectively.

If alternating, that is, periodic in time domain, polarization P is generated with alternating displacement in the c-direction according to the piezoelectric relation,

$$P_3 = e_{31}S_1 + e_{32}S_2 + e_{33}S_3, \tag{5.6.2}$$

as in Fig. 5.29(b), then, the alternating electric dipoles could be strained space-periodically, as in Fig. 5.29(c), by the static PR internal electric field. Since both the electric dipoles and the PR grating are fixed in the crystal, the latter could also be strained space-sinusoidally in the c-direction, and could vibrate *longitudinally* in an *antiphase* state at intervals of every one-half of Λ.

The antiphase strain ΔS_3 caused by the mechanism described above can be expressed as

$$\Delta S_3 = \alpha_{332} E_{in3} E_{ex2}, \tag{5.6.3a}$$

or

$$\Delta S_3 = \alpha'_{333} E_{in3} P_3, \tag{5.6.3b}$$

where E_{in3} is the static PR internal electric field, and E_{ex2} is the alternating external electric field which drives the piezoelectric vibration. The former corresponds to E_{sc} described in §5.2. Coefficients α_{332} and α'_{333} are not constants, and depend on E_{in3}, E_{ex2}, and other experimental conditions.

The alternating polarization illustrated in Fig. 5.29(b) can be generated in the 21-mode in which S_1 and S_3 exist. In both 24- and 22-modes, alternating polarization can be generated in the y-direction according to

$$P_2 = e_{24} S_4 + \chi^S_{22} E_2, \tag{5.6.4a}$$

$$P_2 = e_{22} S_2 + \chi^S_{22} E_2, \tag{5.6.4b}$$

respectively, as in Fig. 5.29(d). In this case, the alternating electric dipoles could be strained *transversely*, as in Fig. 5.29(c). That is, shear vibration occurs in the yz-plane. The antiphase strain ΔS_4 can be expressed as

$$\Delta S_4 = \alpha_{432} E_{in3} E_{ex2}, \tag{5.6.5a}$$

or

$$\Delta S_4 = \alpha'_{432} E_{in3} P_2, \tag{5.6.5b}$$

where α_{432} and α'_{432} are not constants. In Fig. 5.29(c), the displacement *in the c-direction* due to the *transverse* strain ΔS_4 changes space-sinusoidally in the c-direction and space-linearly in the y-direction; therefore, *longitudinal antiphase* vibration could occur *in the c-direction* with a spatial period of Λ. The amplitude and phase of this longitudinal antiphase vibration change *in the y-direction*, unlike the case of ΔS_3. The change in the y-direction depends on the polarization state in the y-direction determined by the vibrational mode.

In the case of 21-mode, ΔS_4 can occur according to

$$P_2 = e_{21} S_1 + e_{22} S_2 + \chi^S_{22} E_2, \tag{5.6.6}$$

and eq.(5.6.5b). Both of ΔS_3 and ΔS_4 can be effective for the generation of the longitudinal antiphase vibration in this case.

Accordingly, piezoelectric polarization, that is, acoustic vibration can be modulated space-periodically by the PR internal field. The wavenumber k of the acoustic vibration can be modulated as

$$k' = k \pm K. \quad (\ |k| << |K| \ ) \tag{5.6.7}$$

Phase velocities of the three waves with the wavenumbers k, $k + K$ and $k - K$ are ω_A/k, $\omega_A/(k + K)$ and $\omega_A/(k - K)$, respectively. On the other hand, group velocities of them are the same as $\mathrm{grad}_k \omega_A$, because of the space-periodicity of the PR superlattice.

5.6.3 *Origin of Nonlinear Spring——— Enhancement of Intrinsic Nonlinearity and Generation of Nonlinearity by Coulomb's Force*

We shall now consider the origin of the nonlinear spring which causes nonlinear phenomena when PR grating exists. There are two possibilities.

First, nonlinearity intrinsic to $LiNbO_3$:Fe can be enhanced by the antiphase vibration of the PR grating mentioned above. In this case, the intrinsic nonlinear spring vibrates in the anti-phase state at intervals of every half of Λ. In general, piezoelectric vibration has some nonlinearity, because antiphase vibration which causes nonlinearity exists with a space-period of wavelength of acoustic wave. But, usual piezoelectric vibration of the resonator without PR grating is *almost* in the in-phase state if compared with the period of the PR grating Λ, because the wavelength of piezoelectric vibration is much larger than Λ. Therefore, nonlinear phenomena of a usual resonator are weaker than those of a resonator with PR grating.

Second, nonlinearity by Coulomb's force which obeys inverse-square law within the vibrating PR space-charge is a possible explanation. Only antiphase vibration contributes to nonlinearity in this case, too. For the sake of simplicity, we assume that electric charges which form PR grating are distributed at intervals of $\Lambda/12$, as illustrated in Fig. 5.30. The quantity of the electric charges q_n is distributed sinusoidally in the c-direction, as illustrated in Fig. 5.30. That is, we can write

$$q_n(Z) = q \sin(2\pi Z/\Lambda)\, \delta(Z - Z_n), \tag{5.6.8}$$

where n is an integer, $Z_n = n\Lambda/12$, $\delta(Z)$ is δ-function, Z is the position in the c-direction fixed in the crystal. In the case of 21-mode, the displacement of the charges which vibrate in the antiphase state Δz_n, as in Fig. 5.29(c), can be expressed as

$$\Delta z_n(Z) = \Delta z \sin(2\pi Z/\Lambda), \quad \text{at position } Z = Z_n, \tag{5.6.9}$$

[caused by ΔS_3]

where Δz is the maximum value of the antiphase displacement, and it depends on experimental conditions. The strain ΔS_3 has a phase difference of $\pi/2$, that is, $\Lambda/4$ from the antiphase displacement Δz_n expressed in eq.(5.6.9), because longitudinal strain in the z-direction and displacement in the z-direction have relationship between differential and integration with each

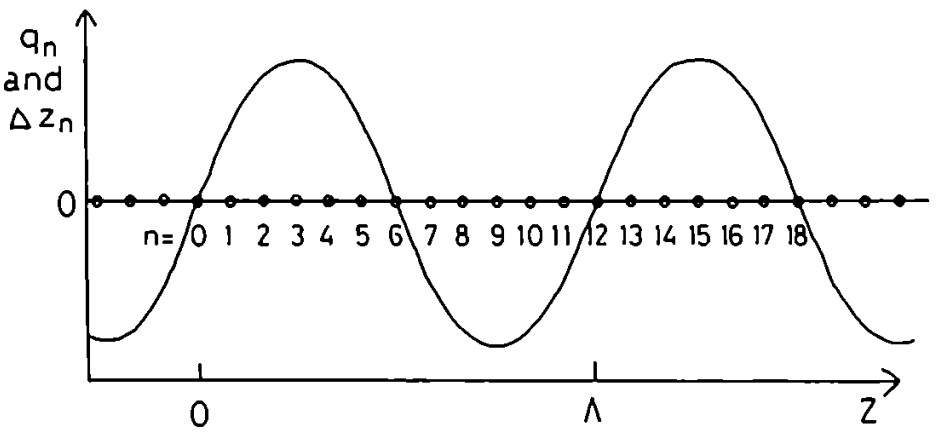

Fig. 5.30. Electric charges which form the PR grating are assumed to be distributed at intervals of Λ/12. The quantities of the electric charges q_n and Δz_n are distributed space-sinusoidally for position Z in the c-direction. In the case illustrated by Figs. 5.29(b) and 5.29(c), the anti-phase displacement Δz_n is in-phase with q_n.

other with regard to the z-coordinate, and both physical values are now sinusoidal functions of Z. When ΔS_4 exists, the antiphase displacement Δz_n due to ΔS_4 depends on not only Z, but also on position Y in the y-direction fixed in the crystal, as described in the previous subsection. In addition, the shear strain ΔS_4 is in-phase with the antiphase displacement Δz_n in the c-direction, because shear strain in the yz-plane and displacement in the z-direction do not have relationship between differential and integration with each other with regard to the z-coordinate. In this case, Δz_n is expressed as

$$\Delta z_n(Y, Z) = -\Delta z \cos(2\pi Z/\Lambda) f(Y), \quad \text{at position } Z = Z_n, \qquad (5.6.10)$$

[caused by ΔS_4]

where $f(Y)$ is a function of position Y. For the sake of simplicity, only ΔS_3 is now considered. The distribution of Δz_n is also illustrated in Fig. 5.30.

Coulomb's force F_k acting on the charge labeled $n=k$ in Fig. 5.30 can be expressed as

$$F_k \propto \sum_{m \neq k} \frac{q_k q_m}{(Z_m + \Delta z_m - Z_k - \Delta z_k)^2}$$

$$\propto C_0 + C_1(\Delta z/\Lambda) + C_2(\Delta z/\Lambda)^2 + C_3(\Delta z/\Lambda)^3 + \cdots . \qquad (5.6.11)$$

Coulomb's force acting between the electric charge labeled n=8 and the charges of n=0 to 16 in Fig. 5.30 is calculated as

$$C_0 = -110, \; C_1 = -141, \; C_2 = 1323, \; C_3 = 7003.$$

The value of C_2 is about ten times as large as the value of C_1. In this calculation, the nearest charges with the same algebraic sign most contribute to nonlinearity of F_k. Summation of eq.(5.6.11) was performed only in the range below a distance of Λ, because electric charges out of this summation range contribute to smaller linearity and nonlinearity. Antiphase vibration of electric charges over a distance of Λ forms weak and almost linear spring through Coulomb's force. On the other hand, in an usual piezoelectric transducer, relationship between stress T_3 and strain S_3 is expressed as

$$T_3 = c^E_{33} S_3 + c^E_{333} S_3^2 + \cdots . \qquad (5.6.12)$$

The value of the usual nonlinear elastic constant c^E_{333} in $LiNbO_3$ is -3.6×10^{11} N/m^2, and that of the linear elastic constant c^E_{33} is 2.4×10^{11} N/m^2. [9] These two constants have the value of comparable order. We find the possibility that nonlinearity by Coulomb's force can be stronger than intrinsic nonlinearity.

Coefficients with even numbers in eq.(5.6.11) exist in this case. On the other hand, Coulomb's force acting between the charges labeled n=9 and other charges in Fig. 5.30 does not

produce coefficients with even numbers; that is,

$$C_0 = 0, C_2 = 0, \cdots,$$

because the system has a centrosymmetry as seen by the charges of n=9. We can consider that the nonlinear spring formed by Coulomb's force in PR grating has spatial distribution with a period of Λ; that is,

$$C_i(Z) = C_i(Z + \Lambda) \quad (i = 0, 1, 2, \cdots). \tag{5.6.13}$$

Upon first glance at eq.(5.6.11), nonlinearity may seem to increase when the value of Λ decreases. However, if an interval between electric charges are unchanged, the coefficients of nonlinear term $C_i(i>1)$ in eq.(5.6.11) begin to decrease when the value of Λ decreases, because the number of charges involved in a period of PR grating decreases. If the value of Λ decreases finally to twice as large as the interval between electric charges, the antiphase vibration of electric charges is similar to optical mode of lattice vibration in solid-state physics, which is almost linear vibration. We can understand that nonlinearity by Coulomb's force depends on distribution of charges and their movement.

§5.7. Discussion

We consider the relationship between the experimental results described in §5.3 to §5.5 and the physical model analyzed in §5.6.

First, we shall explain the reason for disappearance of the present nonlinearity when the Q-value became too large. The increase of the Q-value means the increase of the almost in-phase displacement intrinsic to the piezoelectric resonator, because the Q-value is in proportion to the displacement of vibration at the resonance frequency, as discussed in §3.2.1. Here, the influence of the PR internal electric field on the piezoelectric vibration becomes weaker relative to the case with appropriately small Q-value. As a consequence, the value of the antiphase displacement Δz decreases. The decrease of Δz causes a more rapid decrease of the nonlinear terms than the linear term. This is also explained by the distribution of energy between the two modes, in-phase and antiphase modes. The total energy of the vibration W_t consists of the sum of the energy of the in-phase vibration W_{in} and that of the antiphase vibration W_{anti},

$$W_t = W_{in} + W_{anti}. \tag{5.7.1}$$

When the Q-value is large, the quantity of W_{in} is much larger than that of W_{anti} if W_t is constant, and the usual almost linear vibration inherent in the piezoelectric resonator predominates. When the Q-value is small, the quantity of W_{in} is also small, and that of W_{anti} can not be neglected if W_t

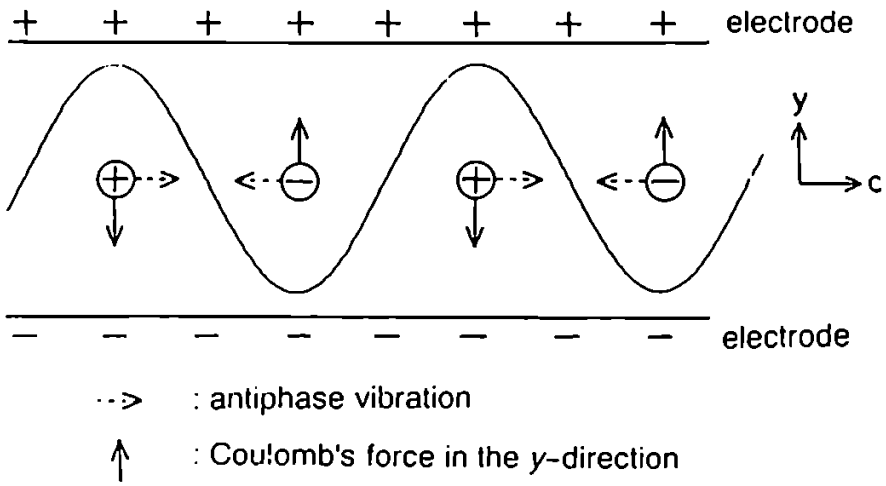

Fig. 5.31. The electric charges on the electrodes in the *y*-planes can influence the electric charges in the PR grating directly by Coulomb's force. These forces in the *y*-direction can act on the PR grating as couples of forces at intervals of Λ/2. The couples of forces can depress the generation of the antiphase vibration.

is constant. Therefore, the unusual nonlinear vibration appears.

In this model, transfer of the energy of the vibration in the c-direction between the two modes is important. In the 21- and 24-modes, the vibration is not clamped in the c-direction. In the 22-mode (the thickness-extensional mode), on the other hand, the vibration is clamped in the c-direction, as discussed in §3.5 and §3.7.3. The reason why the present nonlinearity is clear in the 21- and 24-modes and not clear in the 22-mode has to do with the clamp mentioned above. When the clamp exists in the c-direction, the quantity of W_{in} and W_{t} in the c-direction is small. Therefore, the quantity of W_{anti} transferred from W_{in} is also small, and nonlinearity does not appear clearly in the 22-mode.

The reason for negative dI/dV can also be explained. We assume that the transfer of the energy from W_{in} to W_{anti} occurs when voltage V increases. The transfer of the energy decreases the in-phase displacement the derivative of which corresponds to the current I. That is, the negative dI/dV indicates decrease of usual piezoelectric displacement and increase of nonlinearity by the mechanism described above when V increases. In usual piezoelectric transducer, negative dI/dV cannot occur. When nonlinearity increases in an usual transducer by increase of V, displacement of linear vibration also increases; therefore, dI/dV is always positive in usual piezoelectric vibration.

The obscurity of the present nonlinear behavior when the Q-value is too small results from the usual nonlinear characteristics.

The reason why the type of electrodes influences the experimental results is as follows. The electric charges on the electrodes in the y-planes can influence the electric charges in the PR grating directly by Coulomb's force. Existence of Coulomb's force in the y-direction was suggested by the experimental results shown in Figs. 5.22. These forces in the y-direction can act on the PR grating as couples of forces at intervals of $\Lambda/2$. The couples of forces can depress the generation of the antiphase vibration. Figure 5.31 shows this effect conceptually. After the annealing of the sample, both the quantity of the electric charges forming the PR grating and completeness of the grating decrease, as suggested in §5.4.1. Then, the couples of forces acting on the PR grating change by annealing. It follows that the nonlinear characteristics generated by the antiphase vibration can also change by annealing. However, the existence of the electrodes does not always depress the present nonlinearity, because the electrodes are necessary for the supply of energy to drive both the in-phase and antiphase modes of vibration. The generation of the present nonlinear vibration can be determined by the balance of the vibrational state in the c-direction and the present effect due to the electrodes.

§5.8. Summary

The decrease of Q-value and the generation of nonlinear vibration were detected in the

$LiNbO_3$:Fe piezoelectric transducer in which photorefractive (PR) grating was formed. The decrease of Q means the depression of linear vibration, which is consistent with the generation of nonlinearity. The energy transfer from linear to nonlinear vibration can occur. The PR grating enhances or produces the nonlinearity in crystal. This nonlinearity was strongly influenced by the form of the sample. When the Q-value was too large or too small, depending upon the form of the sample, the present nonlinear behavior became obscure.

In addition, we have discussed the possible reasons for the generation of nonlinear behavior described in the experimental results. The generation of nonlinear vibration requires the existence of both nonlinear springs and their antiphase vibration. The antiphase vibration can occur by the space-periodic modulation of piezoelectric polarization due to the PR internal field. The nonlinear springs originate from the enhancement of nonlinearity intrinsic to $LiNbO_3$:Fe through antiphase vibration and action of Coulomb's force in the vibrating PR space-charge in the antiphase state.

References

1) A.Ashkin, G.D.Boyd, J.M.Dziedzic, R.G.Smith, A.A.Ballman, H.J.Levinstein, and K.Nassau: Appl.Phys.Lett. **9** (1966) 72.

2) A.Yariv: *Optical Electronics 4th ed.* (Holy, Rinehart and Winston Inc., Orland, 1991)

3) P.Gunter *et al.* (editor): *Photorefractive Materials and Their Applications I* (Springer-Verlag, Berlin, 1988)

4) D.E.Oates and J.Y.Pan: Ferroelectrics, **92** (1989) 253.

5) M.Ohki, N.Taniguchi and T.Shiosaki: Jpn.J.Appl.Phys., **31**(1992) 3249.

6) N.V.Kukhtarev, V.B.Markov, S.G.Odulov, M.S.Soskin and V.L.Vinetskii: Ferroelectrics **22** (1979) 949.

7) T.Yagi: Thesis for Bachelor of Engineering, Kyoto Univ. (1993) [in Japanese]

8) M.Ohki and T.Shiosaki: Jpn.J.Appl.Phys., **32**(1993) 2243.

9) T.Mitsui *et al.*: *Landolt-Börnstein* (Springer-Verlag, Berlin, 1981) Group III, Vol.16, Sub-vol.a, p.153.

Chapter 6
Conclusions

In this thesis, new optical measurement methods of piezoelectric vibration and a new phenomenon induced optically in piezoelectric transducers were investigated. The former were described mainly in Chapters 2, 3, and 4, and the latter in Chapter 5. Both investigations were performed using interference of two coherent optical waves and on the basis of the electromechanical measurement method of piezoelectric vibration. The results obtained from this study are summarized here.

In Chapter 2, methods for measurement of piezoelectric vibration using optical fiber were described from an optical point of view. Two new methods for measurement of piezoelectric vibration using the fiber-optic ring interferometer were described.

In one method, the sample is in contact with a fiber in which the light is phase-modulated by the piezoelectric vibration. The fiber is wrapped many turns around a cylindrical piezoelectric transducer. The low frequency limit of S_1 / E_3 measured with this method was nearly in agreement with the material constant d_{31}.

In the other method, the light is incident on the sample surface and phase-modulated by reflection when the sample vibrates. The formulation of this method was described.

In Chapter 3, piezoelectric vibration and material were evaluated using the electromechanical method and the fiber-optic method. A disk piezoelectric transducer was used as the sample. Local measurement of the acoustic amplitude and phase was performed optically.

Optical measurement of the acoustic amplitude gave the values corresponding to the piezoelectric constants d and g locally, taking into account the theory of vibration, the electrical condition of the piezoelectric vibration, and the results of the electromechanical measurement.

It was found that the electric equivalent circuit was not effective for study of the transducer from a local point of view, because the vibration near the boundary was more difficult to follow the external force at higher frequency.

Optical measurement of the acoustic phase gave the acoustic velocity of the radial-extensional mode and the value of Poisson's ratio, utilizing local characteristics of the sample.

In Chapter 4, the measurement methods described in Chapter 3 were applied to circular piezoelectric transducers the forms of which were not thin disk.

For the thick rod sample, d' and g', the optically measured values corresponding to the material constants d and g, respectively, were much smaller than the actual values of the material constants. On the other hand, for the long rod sample, they were nearly in agreement with the material constants. However, the electrical condition of the piezoelectric vibration was not satisfied, especially at the edge of the sample.

The theory of resonance coupling was applied to the problem of measuring d' and g'. It was found that the thin disk and long rod samples were appropriate for the measurement of the material constants; that is, $d' \approx d$ and $g' \approx g$, when the lowest resonance was used for the measurement.

The acoustic velocity of the radial-extensional mode was also measured optically; however, Poisson's ratio could not be measured in this case.

In Chapter 5, the influence of the photorefractive (PR) effect on the piezoelectric vibration was investigated experimentally using the electromechanical method.

The PR grating written in the piezoelectric $LiNbO_3$:Fe transducer decreased the Q-value, and therefore, also depressed the linear vibration. It often caused nonlinear behavior such as nonlinear jump and hysteresis, accompanied by the decrease of the Q-value. The energy transfer from the linear to the nonlinear vibration occurred.

Even after thermal annealing the PR grating seemed to partially remain, and it often caused nonlinear behavior. The generation of the present nonlinear behavior had relation to the forms of the sample, the forms of the electrodes, and the vibrational mode.

The present nonlinear behavior often occurred in the 21- and the 24-modes, but was not evident in the 22-mode.

Too large Q-value depressed the present nonlinear behavior. It is postulated that the usual nonlinear effect is probably enhanced when the Q-value increases because the higher orders of strain become more effective. Accordingly, it was concluded that the nonlinear phenomena observed here for the sample with PR grating were unusual and due to a completely different mechanism. They also did not appear clearly in the sample with too small Q-value due to the irregularity of the form.

The value of space-periodic internal field E_{SC} clearly influenced the piezoelectric characteristics and the dielectric loss.

In addition, the experimental results described above were explained by a new concept, space-periodic modulation of the piezoelectric polarization due to the PR internal electric field: The generation of nonlinear vibration requires both the existence of nonlinear springs and their antiphase vibration. This antiphase vibration can occur through the space-periodic modulation of piezoelectric polarization due to the PR internal field. The nonlinear springs originate from the enhancement of the nonlinearity intrinsic to $LiNbO_3$:Fe through antiphase vibration and Coulomb's force in the vibrating PR space-charge in the antiphase state.

Acknowledgements

This study was performed from 1990 to 1993 at Department of Electronics, Kyoto University. The author expresses his sincere appreciation to Professors Kazumi Matsushige, Hisanao Ogura and Shigeo Fujita for their guidance and suggestions for this thesis. The author acknowledges invaluable advice of Professor Emeritus Akira Kawabata and Assoc. Prof. Tadashi Shiosaki who guided the author's theses for Bachelor's and Master's degrees and the investigation performed thenceforth as well, and helpful advice of Assoc. Prof. Masatoshi Adachi (in Toyama Prefectural Univ.) and Dr. Masaru Shimizu.

The author appreciates important contribution of Messrs. Naomi Shima, Toshihiro Kita, Nobuyuki Taniguchi, and Tadao Yagi to this work, helpful suggestions and work of time by Messrs. Zhiming Chen and Tadashi Kasamatsu from photorefractive and crystallographic points of view, and aid of other members of "Kawabata lab." (Quantum electronics lab.) and its succession research group of Prof. T. Shiosaki.

The author is very grateful to Messrs. Kazuya Ohmae and Hideyo Hiramatsu with Furukawa Electric Co., Ltd. for preparation of experimental facilities, especially, fiber-optic interferometer, to Murata Manufacturing Co., Ltd. for preparation of PZT piezoelectric ceramics in various shapes, and to associates in Department of Applied Physics, National Defense Academy for their kind help to the author at the last stage of this work.

List of Publication

Papers

1) M.Ohki, N.Shima and T.Shiosaki: *Proc. 12th Symp. Ultrasonic Electronics, Tokyo, 1991*, Jpn.J.Appl.Phys., **31**(1992) Suppl.31-1, pp.105-107, "Measurement of Piezoelectric Vibration Using Optical Fiber"

2) M.Ohki, N.Taniguchi and T.Shiosaki: Jpn.J.Appl.Phys., **31**(1992) No.9B, pp.3249-3251, "Influence of Photorefractive Effect on Piezoelectric Vibration"

3) M.Ohki, N.Shima and T.Shiosaki: Jpn.J.Appl.Phys., **31**(1992) No.9B, pp.3272-3275, "Optical Measurement of Piezoelectric Vibration in Circular Rod and Disk Ceramics"

4) M.Ohki and T.Shiosaki: Jpn.J.Appl.Phys., **32**(1993) No.5B, pp.2243-2246, "Space-periodic Model of Piezoelectric Polarization due to Photorefractive Internal Field for Generation of Nonlinear Vibration"

5) M.Ohki, N.Shima and T.Shiosaki: Jpn.J.Appl.Phys., **32**(1993) No.5B, pp.2463-2465, "Optical Measurement of Acoustic Velocity and Poisson's Ratio in Disk Piezoelectric Transducer"

Proceedings

6) M.Ohki and T.Shiosaki: *Proc. IEEE Ultrasonics Symp.,Florida, 1991*, pp.615-620, "Measurement and Evaluation of Piezoelectric Vibration Using Fiber Optic Interferometer"

7) M.Ohki, N.Taniguchi and T.Shiosaki: *Proc. IEEE ISAF, Greenville, South Carolina, 1992*, pp.156-159, "The Effect of Photo-refractively Induced Periodic Strain Grating on Piezoelectric Vibration in $LiNbO_3$:Fe"

8) M.Ohki and T.Shiosaki: *Proc. IEEE Ultrasonics Symp., Tucson, Arizona, 1992* , to be published, "Nonlinear Phenomena Caused by Periodic Charge Distribution in Piezoelectric Resonator"

Technical Reports

9) M.Ohki, N.Shima and T.Shiosaki: IEICE (The Institute of Electronics, Information and Communication Engineers) Tech.Rep., US90-71,EA90-84 (1991.1.25) [in Japanese]

10) M.Ohki, T.Kita and T.Shiosaki: IEICE Tech.Rep., US91-23 (1991.7.16) [in Japanese]

11) M.Ohki, N.Shima and T.Shiosaki: IEICE Tech.Rep., US91-79,EA91-92 (1992.1.28), [in Japanese]

Other Presentation

12) M.Ohki, M.Adachi, T.Shiosaki and A.Kawabata: Extended Abstracts (The 37th Spring Meeting, 1990); JSAP (The Japan Society of Applied Physics) and Related Societies, 28aC8, p.735 [in Japanese]

13) M.Ohki, N.Shima and T.Shiosaki: Extended Abstracts (The 51th Autumn Meeting, 1990); JSAP, 27pL15, p.805 [in Japanese]

14) M.Ohki, N.Shima and T.Shiosaki: Abstract of The 26th Meeting of The 150th Committee in Japan Society for the Promotion of Science [in Japanese]

15) M.Ohki, T.Kita and T.Shiosaki: Extended Abstracts (The 38th Spring Meeting, 1991); JSAP and Related Societies, 31aY2, p.369 [in Japanese]

16) T.Kasamatsu, M.Ohki and T.Shiosaki: Extended Abstracts (The 52th Autumn Meeting, 1991) JSAP, 11pRG8 p.363 [in Japanese]

17) M.Ohki and T.Shiosaki: Extended Abstracts (The 52th Autumn Meeting, 1991); JSAP, 11pRG16 p.365 [in Japanese]

18) M.Ohki, T.Kita, N.Shima and T.Shiosaki: Committee of Research for Dielectric Materials, I-4-010 (1991.11) [in Japanese]

19) M.Ohki, N.Shima and T.Shiosaki: Abstract of The 12th Symposium on Ultrasonic Electronics (1991.12), pp.103-104 [in Japanese]

20) M.Ohki, N.Shima and T.Shiosaki: Extended Abstracts (The 39th Spring Meeting, 1992); JSAP and Related Societies, 30aK2 p.362 [in Japanese]

21) M.Ohki, N.Taniguchi and T.Shiosaki: Extended Abstracts (The 39th Spring Meeting, 1992); JSAP and Related Societies, 30aK29 p.368 [in Japanese]

22) M.Ohki, N.Taniguchi and T.Shiosaki: Abstract of The 9th Symposium on Ferroelectric Materials and their Applications (1992.5), pp.117-118 [in Japanese]

23) M.Ohki, N.Shima and T.Shiosaki: Abstract of The 9th Symposium on Ferroelectric Materials and their Applications (1992.5), pp.131-132 [in Japanese]

24) M.Ohki, N.Shima and T.Shiosaki: Abstract of The 13th Symposium on Ultrasonic Electronics (1992.12), pp.221-222 [in Japanese]

25) M.Ohki and T.Shiosaki: Abstract of The 13th Symposium on Ultrasonic Electronics (1992.12), pp.233-234 [in Japanese]